



HAL
open science

Apprentissage statistique et automatique pour la détection des défauts de soudures : application à la fabrication de ballons d'eau chaude sanitaire

Abdallah Amine Melakhsou

► **To cite this version:**

Abdallah Amine Melakhsou. Apprentissage statistique et automatique pour la détection des défauts de soudures : application à la fabrication de ballons d'eau chaude sanitaire. Mathématiques [math]. Université de Lyon, 2023. Français. NNT : . tel-04892807

HAL Id: tel-04892807

<https://hal-emse.ccsd.cnrs.fr/tel-04892807v1>

Submitted on 29 Jan 2025

HAL is a multi-disciplinary open access archive for the deposit and dissemination of scientific research documents, whether they are published or not. The documents may come from teaching and research institutions in France or abroad, or from public or private research centers.

L'archive ouverte pluridisciplinaire **HAL**, est destinée au dépôt et à la diffusion de documents scientifiques de niveau recherche, publiés ou non, émanant des établissements d'enseignement et de recherche français ou étrangers, des laboratoires publics ou privés.

THÈSE DE DOCTORAT

de Mines Saint-Etienne - Une école de l'IMT

Ecole Doctorale N°488
(Sciences, Ingénierie, Santé)

Spécialité de doctorat : Mathématiques appliquées

Soutenu publiquement le 07 septembre 2023 par :

Abdallah Amine Melakhsou

**Automated welding defect detection using
statistical and machine learning: case study of
hot water tanks manufacturing**

Devant un jury composé de :

Jairo Cugliari	HDR Maitre de conférence, Université Lyon 2	Rapporteur
Emmanuel Ramasso	HDR Maitre de conférence, SUPMICROTECH-ENSMM	Rapporteur
Gilles Roussel	Professeur, Université du Littoral-Côte d'Opale	Examinateur
Marianne Clausel	Professeure, Université de Lorraine	Examinatrice
Anis Hoayek	Maitre de conférence, Mines Saint-Etienne	Examinateur
Mireille Batton-Hubert	Professeure, Mines Saint-Etienne	Directrice de thèse

Affidavit

Je soussigné, Abdallah Amine Melakhsou, déclare par la présente que le travail présenté dans ce manuscrit est mon propre travail, réalisé sous la direction scientifique de Mireille Batton-Hubert dans le respect des principes d'intégrité et de responsabilité inhérents à la mission de recherche. Les travaux de recherche et la rédaction de ce manuscrit ont été réalisés dans le respect de la charte nationale de déontologie des métiers de la recherche.

Ce travail n'a pas été précédemment soumis dans sa globalité en France ou à l'étranger dans une version identique ou similaire à un organisme examinateur.

Fait à Saint-Etienne, le 03/07/2023.

Ce travail de thèse est une œuvre de l'esprit, protégée par le droit d'auteur, tel que prévu aux articles L111-1 du CPI et suivants disposant que « *L'auteur d'une œuvre de l'esprit jouit sur cette oeuvre, du seul fait de sa création, d'un droit de propriété incorporelle exclusif et opposable à tous. [...]* »

Il est rappelé que par exception au droit d'auteur, la loi française autorise l'utilisation d'une œuvre divulguée, sans autorisateur de son auteur, suivant les conditions définies dans l'article L122-5 du CPI disposant que « *Lorsque l'œuvre a été divulguée, l'auteur ne peut interdire [...] la représentation ou la reproduction d'extraits d'œuvres, [...] sous réserve que soient indiqués clairement le nom de l'auteur et la source [...] les analyses et courtes citations justifiées par le caractère critique, polémique, pédagogique, scientifique ou d'information de l'œuvre à laquelle elles sont incorporées [...]* »

Remerciements

Je désire témoigner ma reconnaissance à de nombreuses personnes avec qui j'ai travaillé tout au long de mon doctorat et à tous ceux qui ont contribué de loin ou de près à l'accomplissement de ce travail. Tout d'abord, je tiens à remercier Mireille Batton-Hubert, professeure de l'école des mines, qui m'a encadré tout au long de cette thèse, pour ses qualités humaines, sa disponibilité permanente et pour tout ce que nous avons pu accomplir ensemble dans ce travail.

Je tiens à exprimer tous mes remerciements à Julio Cugliari et Emmanuel Ramasso qui m'ont fait l'honneur d'être rapporteur de ce manuscrit. Je remercie également Marianne Clausel, Gilles Roussel et Anis Hoyaek d'en être les examinateurs.

Ma gratitude va également à Nicolas Casoetto, Thierry Mellouet et Erwan Stephens, avec lesquels j'ai beaucoup appris et qui m'ont accompagné dans la partie industrielle du doctorat.

Je remercie également toute ma famille, en particulier ma mère, pour son soutien sans cesse malgré la distance qui nous sépare.

Enfin, un immense merci à tous mes collègues du laboratoire génie mathématique et industriel ainsi que mes collègues d'elm leblanc pour tous les échanges et les collaborations ainsi que les bons moments passés ensemble.

Présentation de la thèse

La fabrication de ballons d'eau chaude implique la production d'un produit complexe composé de divers éléments qui subissent de multiples soudages manuels et automatiques. La qualité des soudures est cruciale pour assurer la qualité globale et la durabilité du produit final. Par conséquent, l'inspection de la qualité des soudures joue un rôle essentiel dans cette industrie. Cependant, ceci est souvent encore effectué à l'aide de méthodes traditionnelles d'inspection de la qualité qui reposent principalement sur l'inspection humaine. Néanmoins, ces méthodes d'inspection sont chronophages et sujettes à un taux élevé d'erreurs.

Une solution potentielle pour surmonter les problèmes des techniques d'inspection classiques est l'utilisation de l'apprentissage automatique. Ces dernières années, les algorithmes d'apprentissage statistique et automatique ont attiré une attention considérable dans l'industrie manufacturière et sont utilisés pour diverses tâches, telles que l'optimisation de la chaîne d'approvisionnement, la prévision de la demande, l'optimisation des processus et la détection des défauts. L'objectif principal de ce travail de recherche est le développement de systèmes de détection et de diagnostic des défauts de soudage utilisant l'apprentissage statistique et automatique en exploitant les signaux des variables de soudage capturés lors des processus de soudage automatique ainsi que des images du cordon de soudure final.

L'utilisation de l'apprentissage automatique pour la détection des défauts de soudage peut être particulièrement difficile dans le contexte du soudage des ballons d'eau chaude pour de nombreuses raisons, telles que la dynamique complexe du soudage, la diversité des procédés de soudage utilisés et le large éventail de défauts qui peuvent avoir lieu. Nous proposons dans cette thèse des approches qui répondent à ces défis, dans le but de développer des systèmes destinés à être utilisés pour la détection en temps réel des défauts de soudage dans la fabrication des ballons d'eau chaude.

Après avoir étudié la faisabilité de la détection des défauts à partir des signaux de soudage, nous avons proposé une approche basée sur le One-Class SVM et les noyaux de substitution de la distance. Cette approche ne nécessite que des données de soudures sans défaut dans la phase d'apprentissage, ce qui surmonte le problème du manque d'étiquettes, car elle peut détecter toute anomalie des signaux des variables de soudage. De plus, l'approche proposée fonctionne avec les

signaux bruts et détecte les anomalies en fonction de leurs distances aux données normales, ce qui facilite la généralisation sur des signaux de différents types provenant de différents procédés de soudage. En plus de la détection d'anomalies, nous avons également proposé une approche de diagnostic basée sur la classification des sous-séquences anormales des signaux.

Une autre approche est proposée où nous avons étendu la transformée de noyaux convolutifs aléatoires au problème de détection d'anomalies. L'approche utilise cette transformée pour détecter et expliquer les anomalies dans des séries temporelles, ce qui peut assister dans le diagnostic des défauts. En plus des signaux de soudage, nous proposons également un système qui détecte les défauts à partir des images de la soudure. Nous avons conçu un système d'acquisition d'images et entraîné un réseau neuronal capable de localiser et de classer les défauts de soudure.

Cette thèse a été effectuée en partenariat avec elm.leblanc, une entreprise du groupe Bosch, dans le cadre d'une convention Cifre.

Contents

General introduction	7
1 Study of the burn-through detection in the circular welding	9
1.1 Introduction	10
1.2 Literature review on welding defect detection	16
1.2.1 Statistical process control	16
1.2.2 Machine Learning techniques	16
1.3 Methods	19
1.3.1 Kernel Density Estimation	19
1.3.2 Functional non-parametric kernel classifier	20
1.3.3 Pipeline of burn-through detection	24
1.4 Results and discussion	26
1.4.1 Preliminary study of the methodology	26
1.4.2 Results	28

CONTENTS

1.4.3	Comparative study	33
1.5	Burn-through root cause in the circular welding of hat water tanks	35
1.6	Conclusion	40
2	One-class classification for welding fault detection	43
2.1	Introduction	44
2.2	Literature review on abnormal time series subsequence detection	47
2.2.1	Methods for anomaly detection in the raw and discrete representations	48
2.2.2	Methods based on features for anomaly detection	52
2.3	Methods and materials	53
2.3.1	Definition and notations	53
2.3.2	Problem Formulation	55
2.3.3	One-Class SVM with distance substitution kernels	56
2.3.4	Time series dissimilarity measures	62
2.3.5	Experimental protocol	65
2.3.6	Evaluation metric	68
2.4	Description of welding processes and preprocessing	69
2.4.1	The circular welding	69
2.4.2	The orbital welding	70
2.4.3	Cold Metal Transfer welding	77
2.5	Results and discussion	82

CONTENTS

2.6	Welding defect diagnosis using Random Convolutional Kernel Transform	89
2.7	Conclusion	96
3	Welding defect detection using random convolutional kernel transform	99
3.1	Introduction	100
3.2	Methods	101
3.2.1	Random convolutional kernel transform with OC-SVM	101
3.2.2	Approach 1: Explainable abnormal subsequence detection using ROCKET .	104
3.2.3	Approach 2: Dimensionality reduction techniques with ROCKET and OC-SVM	108
3.3	Results and discussion	109
3.3.1	Results of the first approach	111
3.3.2	Results of the second approach	116
3.4	Conclusion	123
4	Computer vision-based welding defect detection	125
4.1	Introduction	126
4.2	Literature review on computer vision-based defect detection	128
4.2.1	Supervised defect detection	128
4.2.2	Unsupervised defect detection	131
4.3	Methods and materials	132
4.3.1	You Only Look Once v3 network	133

CONTENTS

4.3.2	Evaluation metric	137
4.3.3	Image acquisition system	138
4.4	Results and discussion	139
4.5	Conclusion	144
General conclusion		147
Bibliography		153
Appendix		165
A	Causality between welding signals	165
B	Whole time series anomaly detection	167
C	The software for real-time anomaly detection and diagnosis in the circular welding process	169
D	Detecting abnormal subsequences of variable lengths	170
E	Pseudocode of ROCKET for explainable abnormal subsequence detection	173
F	Testing ROCKET and OC-SVM on time series from different domains	175
G	Welding defect diagnosis using ROCKET and K-means	179
H	Unsupervised welding defect detection from weld images	182

List of Figures

1	The manufacturing process of hot water tanks.	3
2	An illustration of the arc welding process.	4
3	Some examples of welding defects illustrated from the front view of welded pieces.	5
1.1	Illustration of the TIG welding (Antonini (2014)).	10
1.2	Illustration of the setup of the circular welding process.	12
1.3	Examples of signals of a defect-free weld (a) and a weld with a burn-through (b).	13
1.4	Periodogram of the voltage and current signals in the case of welding duplex water tanks.	14
1.5	The proposed procedure for burn-through detection and localization.	15
1.6	The two sinusoidal signals and their PDDs.	22
1.7	An example of classification using the non-parametric kernel classifier.	24
1.8	Diagram of the adopted methodology for defect detection and localization.	25
1.9	Example of processed signals according to the proposed methodology. The PDDs are log-transformed.	27

LIST OF FIGURES

1.10 (a) The first FPCA function. (b) The second FPCA function and the variation projection (c).	28
1.11 The ROC curves of the classifiers A and B.	30
1.12 The effect of the PDD's bandwidth on the classifiers' accuracy.	31
1.13 The effect of the training sample size on the accuracy of the classifier A.	32
1.14 Signals of defective welds where burn-through are localized (shown in red).	33
1.15 Histogram of the defects' localization.	36
1.16 The two types of burn-through in the signals.	36
1.17 An interpretation of the first type of burn-through signature.	37
1.18 The two types of burn-through shown in real pieces.	37
1.19 Tear of the longitudinal weld.	38
1.20 Voltage signals where the burn-through is detected at the end of the welding cycle.	39
1.21 The distortion caused by the welding of the muff.	40
2.1 Types of univariate time series anomalies.	45
2.2 The procedure followed for the detection of abnormal subsequences.	46
2.3 Illustration of lockstep and elastic dissimilarity measures.	54
2.4 Illustration of OC-SVM with the linear (a) and nonlinear (b) kernels.	59
2.5 An illustration of a Sakoe-Chiba constraint. The white cells indicate the allowed shifts from the diagonal.	63
2.6 Illustration of the <i>lb_keogh</i> . The hatched region is the lower bound.	64

LIST OF FIGURES

2.7	The experimental protocol.	65
2.8	The representation of the subsequences obtained by the MDS. (a) overlapping sub-sequences, (b) non-overlapping subsequences.	66
2.9	Illustration of the 5-folds evaluation technique.	68
2.10	Example of a normal signal (a) and a signal with an abnormal subsequence (b).	70
2.11	The setup of the orbital welding of nipples.	71
2.12	An example of a normal voltage signal of the orbital welding.	71
2.13	An example of a signal with spikes.	72
2.14	The despiked signal obtained by the despiking methods.	73
2.15	The proposed despiking method.	74
2.16	The despiked signal obtained with the proposed method.	75
2.17	The strategy followed for signal despiking.	76
2.18	The setup of the CMT process.	78
2.19	Illustration of the CMT process (Srinivasan et al. (2022)).	78
2.20	Voltage and current signals and the corresponding welds of the sub-signals.	79
2.21	The segmentation method.	80
2.22	The despiking technique used for the CMT signals.	81
2.23	Histogram of the sub-signals lengths.	81
2.24	Histogram of the correlation between current and voltage.	81
2.25	Examples of signals and the associated anomaly scores for each subsequence. (a) The circular welding, (b) the orbital welding, and (c) the CMT welding.	87

LIST OF FIGURES

2.26	Examples of multivariate welding signals along with the produced anomaly scores.	88
2.27	The 6 most observed welding defects.	90
2.28	Illustration of the anomaly detection output (the anomaly scores) and how it is used to extract welding defects' signatures.	91
2.29	An illustration of ROCKET.	94
2.30	Accuracy of ROCKET as a function of the number of random kernels.	95
3.1	An illustration of the two proposed approaches.	103
3.2	An illustration of the convolution between a subsequence and a convolutional kernel.	105
3.3	An illustration of the feature importance estimation.	106
3.4	Examples of abnormal subsequences of the circular welding signals along with the three most important kernels.	113
3.5	Examples of abnormal subsequences of the orbital welding signals along with the three most important kernels.	113
3.6	The three most important random kernels obtained from 4 different runs.	114
3.7	The three most important random kernels obtained using our approach (in blue) and those obtained with TreeSHAP (in red).	115
3.8	An example of an abnormal subsequence from the CMT welding signals that cannot be effectively explained.	115
3.9	The three most important random kernels obtained with a model using 5000 random kernels.	116
4.1	Types of the orbital welding defects.	127

LIST OF FIGURES

4.2	illustration of the YOLOv3 architecture.	134
4.3	The output of YOLO at each prediction level.	135
4.4	The architecture of YOLOv3 Tiny (Ding et al. (2019)).	136
4.5	Illustration of the IOU.	138
4.6	The proposed image acquisition system.	139
4.7	The USB camera module used for image acquisition.	139
4.8	The four objects to be detected: three defects and one pseudo defect (impurity). . .	140
4.9	The proposed system for the welding inspection.	142
4.10	A screenshot of the developed GUI.	143
4.11	The quality control station based on the proposed system.	143
4.12	A defect detected by the model on an image of a different welding process.	144
13	An example of voltage and wire speed signals, where the burn-through is noticed in both.	165
14	The pipeline of the circular welding monitoring.	169
15	A screenshot of the developed software.	169
16	The two proposed approaches for detecting abnormal variable length subsequences. . .	170
17	Anomaly scores produced by each approach for the test signal.	172
18	ECG signal along with the ground truth labels and anomaly scores.	175
19	Mars Curiosity rover signal along with the ground truth labels and anomaly scores. .	176
20	A zoom on the abnormal subsequence.	176

LIST OF FIGURES

21	Anomaly score obtained with the larger moving window.	177
22	The most important kernels obtained using the proposed explainability approach. . .	178
23	Silhouette scores for different numbers of clusters for (a) orbital signals' subsequences and for those of the CMT signals (b).	179
24	The centroids of the abnormal subsequences of the "orbital 1" signals.	180
25	The centroids of the abnormal subsequences of the CMT connection welding signals.	181
26	The segmentation of the welded tube image.	182
27	An illustration of the autoencoder for image reconstruction.	182
28	Some results of anomaly detection from the anomaly map.	183

List of Tables

1.1	Information on welding parameters.	11
1.2	The confusion matrix of the classifier A.	29
1.3	The confusion matrix of the classifier D.	29
1.4	Optimal parameters of the two classifiers.	30
1.5	The confusion matrix of the defect localizer A.	32
1.6	The confusion matrix of the defect localizer D.	32
1.7	Comparison with other techniques.	34
1.8	Comparison with other techniques when training on 10% of the whole dataset.	34
2.1	The confusion matrix.	68
2.2	Number and length of the subsequences used for each signal.	82
2.3	Results for abnormal subsequence detection in the circular welding process.	83
2.4	Results for defect detection in the first part of the tube welding signal.	83
2.5	Results for defect detection in the second part of the tube welding signal.	83

LIST OF TABLES

2.6	Results for abnormal subsequence detection in the connection tube welds.	85
2.7	Results for abnormal subsequence detection in the intersection welds.	85
3.1	F1-score for all the signals obtained by the first approach.	111
3.2	The results of the models using only <i>mv</i> in the feature vector.	117
3.3	The results of the models using only <i>ppv</i> in the feature vector.	118
3.4	The results of the models using both <i>mv</i> and <i>ppv</i> in the feature vector.	120
3.5	The results of the models as a function of the number of random kernels used to transform the subsequences.	121
3.6	Results of the models using 50 random kernels with only high dilation values.	122
4.1	The number of images used in the study.	141
4.2	The AP of each class with the mAP of each model. (BT 1= Burn-through 1, BT 2= Burn-through 2, NW= No Weld, Imp=Impurity).	142
3	Results of Transfer Entropy estimated for the defective weld signals	166
4	Results for abnormal full-series detection in the circular welding process.	167
5	Results for abnormal full-series detection in the orbital welding process.	167

General Introduction

Context

Hot water tank manufacturing involves the production of a complex product composed of various components that undergo multiple manual and automatic welding processes. The quality of the welds is crucial for ensuring the overall quality and durability of the final product. Consequently, weld quality inspection plays an essential role in this industry. However, it is still often performed by traditional quality inspection methods that primarily rely on human inspection. Typically, the welds are inspected visually by the operator after each welding cycle and by a final liquid penetrate testing at the end of the manufacturing process. Because of the small size that welding defects can have, the large number of welds to inspect, and the required expertise to detect welding defects, human visual inspection becomes time-consuming and error-prone, resulting in reduced efficiency. Moreover, welding defects that are not detected by the operator at a given stage of the manufacturing process will lead to a nonconforming final product that will eventually be detected at the final test. In such cases, the entire product must be discarded, leading to high scrap costs and possible negative impacts on the environment. Additionally, there are cases in which the defect is not detected by the final test. The consequences in this scenario may prove to be considerably more severe, as the product would be shipped back by the client, resulting in high logistics costs.

A potential solution to overcome the shortcomings of classical inspection techniques is the use of machine learning. In recent years, statistical and machine learning algorithms have gained significant attention in the manufacturing industry and are used for various tasks, such as supply chain

optimization, demand forecasting, process optimization, and defect detection. The primary objective of this research work is the development of automatic welding defect detection and diagnosis systems using statistical and machine learning in the case of hot water tank manufacturing.

A background on the manufacturing of hot water tanks

The manufacturing process of hot water tanks consists of multiple stages. The essential steps are shown in Fig. 1. Initially, two sub-processes are involved in transforming two initial pieces, which are stainless steel metal sheets and tubes. Part of the metal sheets is dedicated to producing the caps by a deep-drawing process, while another part is rolled to create the ferrule. Subsequently, the ferrule (cylinder) is welded with a longitudinal welding machine before joining a muff at one of its ends by another welding machine.

On the other side, the tubes are bent and rolled to create sticks and coils. Each two coils are assembled by an orbital welding process to make the heat exchanger. Finally, a small piece called the nipple is welded at the ends of the sticks and the coils.

The last two welding processes constitute the stages where all previously manufactured parts are assembled. First, the coils and rods are placed inside the ferrule, and the assembly, consisting of two caps and the equipped ferrule, is put into a machine that assembles them by welding. The final welding process fixes the tubes to the ferrule with a robotic welding arm, which forms the hot water tank connections.

There are numerous welding types, each possessing its own advantages and application range. Concerning the manufacturing of hot water tanks, arc welding is used for all the welding processes presented above. Arc welding is a family of welding techniques that use the heat produced by an electrical arc to melt and fuse the pieces. The preference for arc welding in the context of the manufacturing of hot water tanks arises from its suitability for joining thin sheets of stainless steel. Fig. 2 illustrates arc welding in its basic form. The electric arc is created between an electrode and the workpiece, which produces sufficient heat for the fusion of the pieces. Shielding gas is often used to protect the weld area from contamination. The shielding gas can be an inert gas, such as

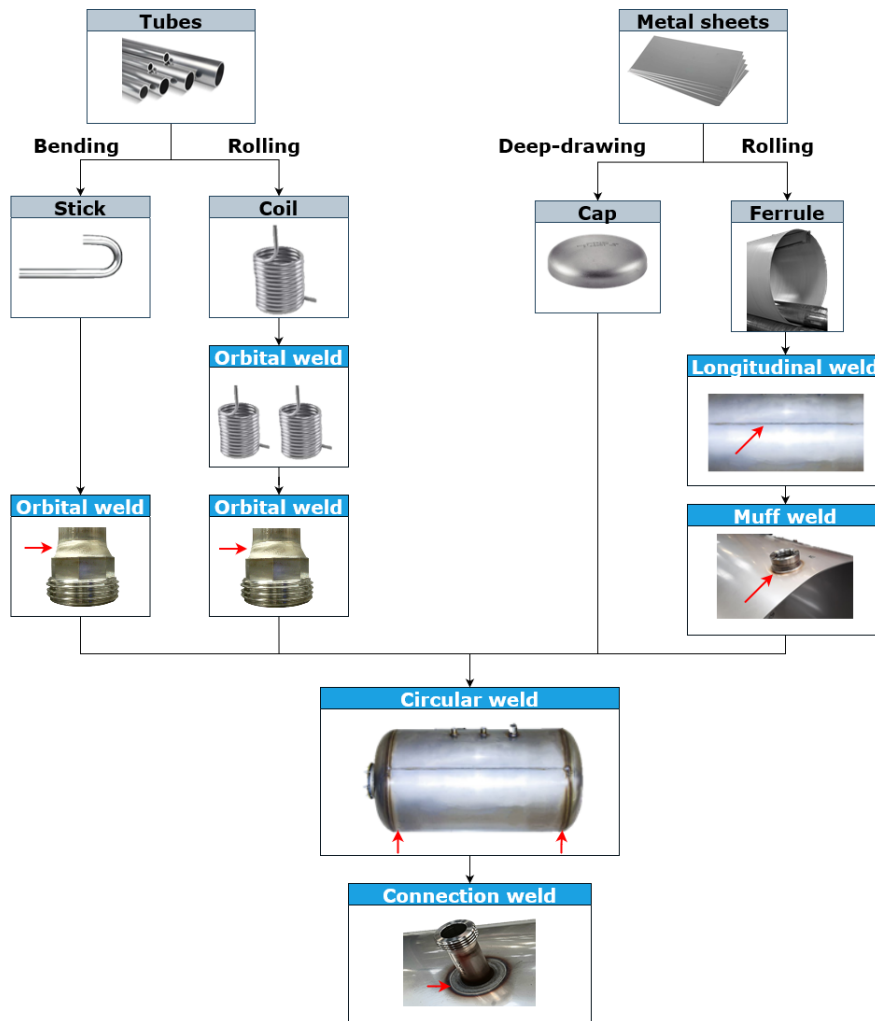


Figure 1: The manufacturing process of hot water tanks.

argon, helium, or a mixture of both. In some cases, an active gas, such as carbon dioxide, can be used as the shielding gas.

As noted, there are different types of arc welding techniques, such as Shielded Metal Arc Welding (SMAW), Gas Metal Arc Welding (GMAW), Flux-Cored Arc Welding (FCAW), etc. The choice of arc welding method depends on the type of metal being welded, the thickness of the pieces, and the specific application requirements. The types of arc welding used in the manufacturing of hot water tanks will be described later in the manuscript.

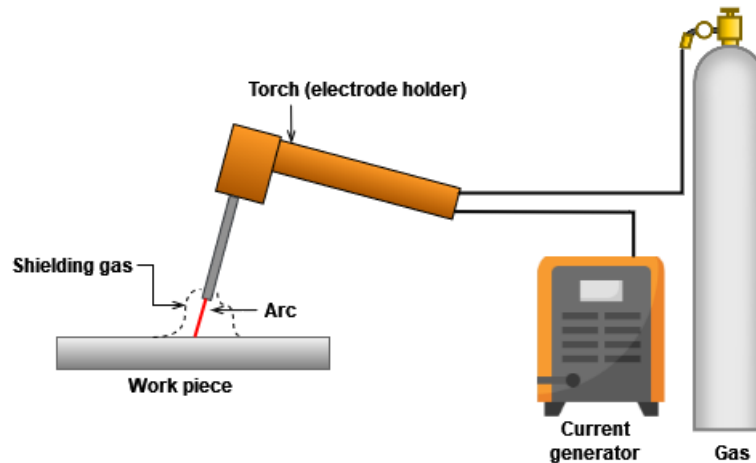


Figure 2: An illustration of the arc welding process.

A background on welding defects

Due to the range of welding techniques and the multitude of factors that impact the welding process, a broad spectrum of welding defects can occur. Fig. 3 gives an illustration of some welding defects. The lack of penetration indicates that the gap between the two pieces is not completely filled. This can occur when the heat level is low or when the size of the electrode is not adequate. Cracks, on the other hand, are fractures that can be caused by high stress levels or improper cooling. Porosities are small holes that are formed in the weld pool resulting from gas bubbles that do not escape the weld pool. This defect can be caused by unclean pieces or high welding speed. Burn-through is a penetration through the pieces being welded, which can be caused by a high level of heat, low welding speed, or misalignment between the pieces. Misalignment is also an undesirable event even without the presence of burn-through, as it reduces the durability of the weld.

There are many other welding defects that can occur, which, among other reasons, makes automatic welding defect detection a challenging subject.

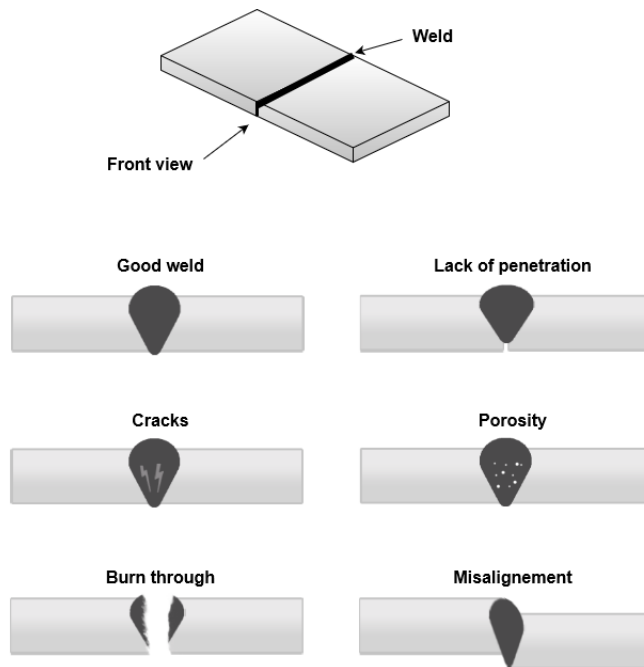


Figure 3: Some examples of welding defects illustrated from the front view of welded pieces.

Objectives of the research work

The primary objective of this research work is the development of automatic welding defect detection and diagnosis systems using statistical and machine learning by leveraging the signals of the welding variables that are captured during the automatic welding processes. Additionally, the research work explores defect detection from weld images acquired after welding has been completed.

The use of machine learning for automatic welding defect detection is particularly challenging in the context of hot water tank welding for numerous reasons, namely:

- **The complex dynamics of the welding operation:** this could make differentiating between a good and a defective weld difficult.
- **The diversity of the welding processes used in the manufacturing of this product:** this suggests that a machine learning model used to detect defects in a given process might

not be adequate to detect defects in another welding process.

- **The diversity of the welding defects:** as evoked earlier, a wide range of welding defects can occur. Hence, labeling data can be a time-consuming and expensive task, especially if deliberately made defects are needed for this purpose.
- **The quality of the data:** in an industrial environment, it can be difficult to acquire data without external interference, which can make defect detection challenging.

This thesis proposes approaches that specifically address these challenges, with the aim of developing systems intended to be utilized for real-time welding defect detection in the manufacturing of hot water tanks. Hence, in addition to the discussed challenges, the approaches must also satisfy the criteria of accuracy and inference time. Moreover, a research question that is addressed in this work is the possibility of predicting the defect's root cause from the welding data.

Organization of the manuscript

This thesis is organized as follows:

In Chapter 1, we study the feasibility of an automatic burn-through detection in the circular welding process, which is one of the most observed welding faults in the manufacturing of hot water tanks. We begin by reviewing the techniques used in the literature for automatic welding defect detection. We then propose a method for burn-through detection and localization. Additionally, we study the root causes of this defect and explore the possibility of an automatic diagnosis and root cause extraction from welding signals.

In Chapter 2, we treat the problem of detecting any welding abnormality based on the concept of semi-supervised time series anomaly detection. This addresses the challenges of the lack of labels and the problem of generalization to different welding signals. Moreover, we propose in this chapter an automatic diagnosis of welding anomalies using a classification approach.

In Chapter 3, we propose an approach to the problem of welding defect detection that can produce an explanation about why an anomaly is detected as such, which may be used as a tool

for root cause extraction. Furthermore, an approach is proposed that also addresses the problem of generalization to different welding signals.

In Chapter 4, we address the problem of welding defect detection through weld images. We begin with a literature review of computer vision-based defect detection. We then present the developed image acquisition system and the adopted approach used for the defined objectives.

Chapter 1

Study of the burn-through detection in the circular welding

Contents

1.1	Introduction	10
1.2	Literature review on welding defect detection	16
1.2.1	Statistical process control	16
1.2.2	Machine Learning techniques	16
1.3	Methods	19
1.3.1	Kernel Density Estimation	19
1.3.2	Functional non-parametric kernel classifier	20
1.3.3	Pipeline of burn-through detection	24
1.4	Results and discussion	26
1.4.1	Preliminary study of the methodology	26
1.4.2	Results	28
1.4.3	Comparative study	33
1.5	Burn-through root cause in the circular welding of hot water tanks	35
1.6	Conclusion	40

1.1 Introduction

In this first chapter, we are interested in studying and exploring welding signals in the circular welding process. Our aim in this study is to explore the possibility of developing automatic burn-through detection through welding signals. Moreover, we are interested in studying the root cause of the burn-through in this process and the feasibility of an automatic root cause extraction from the welding signals.

The circular welding machine employs Tungsten Inert Gas (TIG), also called Gas Tungsten Arc Welding (GTAW), which is a type of arc welding used to produce high-quality welds on most materials such as steel, stainless steel, aluminum, and nickel alloys and is in use in different sectors such as aeronautics and automobile industry. During this welding process depicted in Fig. 1.1, an electrical arc is created between a non-consumable tungsten electrode and the workpiece to produce the required heat for the fusion. The protection of the weld pool from contamination and oxidation is assured by an inert gas such as argon or nitrogen. GTAW can be used with or without the filler wire depending on the application and is highly known for its suitability for the assembling of thin parts.

Like any welding process, GTAW is subject to defects such as lack of penetration, porosity,

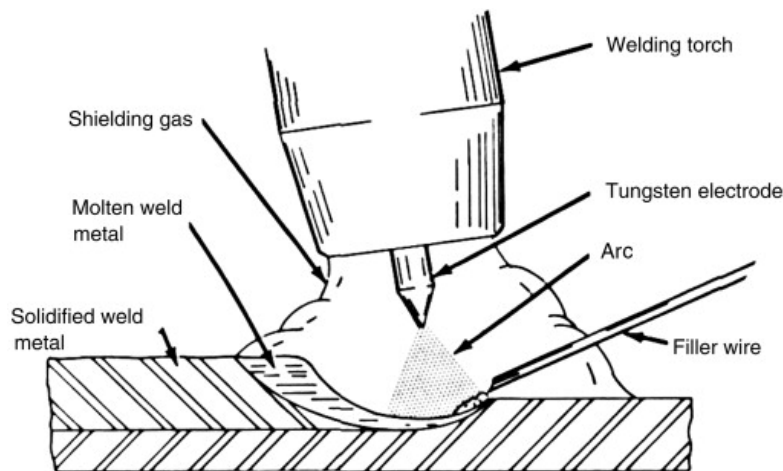


Figure 1.1: Illustration of the TIG welding (Antonini (2014)).

and burn-through. In the circular welding of hot water tanks, the latter is the most commonly encountered fault. The inspection of the circular weld is performed visually by the operator at the end of the process. However, due to the large number of tanks produced and the difficulties in inspecting the whole welding seam around the perimeter of the water tank, this procedure is time demanding and can be prone to errors. Our objective in this chapter is to study the electrical signals acquired during this welding and explore the possibility of automatic burn-through detection.

The process of circular welding is depicted in Fig. 1.2. It is carried out by a semi-automatic machine, which simultaneously performs the welding of the two caps of the hot water tank with the cylinder. During the circular welding process, the tank rotates at a constant speed, whereas the two torches are immovable. The wire is automatically fed to the pool at a constant speed and the welding is conducted using a constant current or pulsed current depending on the type of the tank to be welded. We study in this chapter two types of hot water tanks that are made respectively of austenitic and duplex stainless steel. Information on the nominal values of the process variables of each type is given in Table 1.1.

Two sets of signals per tank are acquired in real-time, which consist of current, voltage, and wire feed speed for each of the two welds. The sampling rate is fixed at 25 Hz and the acquisition is done by WeldQAS data acquisition device to which are connected the sensors as Fig. 1.2 shows. We obtain signals consisting of 2800 and 1700 points respectively for the austenitic and the duplex hot water tanks.

We noticed that the voltage is the variable that contains most of the information regarding the arc behavior during welding. For both types of tanks, the current signal is nearly constant. This is due to the fact that the current is produced by the generator and has only a minor interaction with the welding operation in this specific welding process. We also found that the wire feed speed is very often not informative for the detection of burn-through. Fig. 1.3.(a) shows the three signals of a good weld of an austenitic tank, and Fig. 1.3.(b) shows the signals of a weld with burn-through.

Table 1.1: Information on welding parameters.

	Current type	Current (A)	Voltage (V)	Wire speed (m/min)
Duplex	Pulsed at $f=7\text{Hz}$	190	10.5	8
Austenitic	Constant	180	10	8.5

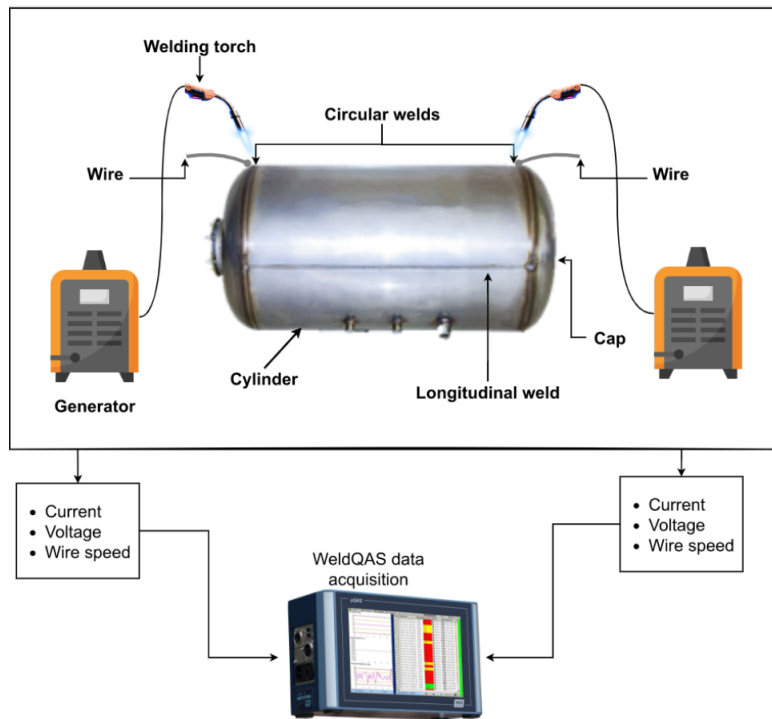


Figure 1.2: Illustration of the setup of the circular welding process.

As discussed above, the current and the wire feed speed are approximately the same for the two welds, while the voltage signals are different. We noticed that the burn-through in this process is indicated by peaks in the voltage signal. This is because the voltage is correlated with the arc length. As a consequence, when the arc lengthens because of a hole in the weld seam, the voltage increases rapidly. In the considered example, the burn-through is highlighted in red in Fig.1.3.(b) around the 20th second. According to the morphology of the burn-through, the peaks can have variable duration and amplitude. Moreover, despite the fact that the welding of the two caps is simultaneous, the presence of a burn-through on one side does not indicate its presence on the other. In fact, a burn-through is frequently observed on only one side at a time.

An important observation that must be taken into account for the development of an adequate method for burn-through detection, is that welding voltage signals can be nonlinear and non-stationary because of the complex dynamics of the welding operation (Bingul et al. (2000)). Often, the voltage signals of the circular welding process are non-stationary. To show this, we apply

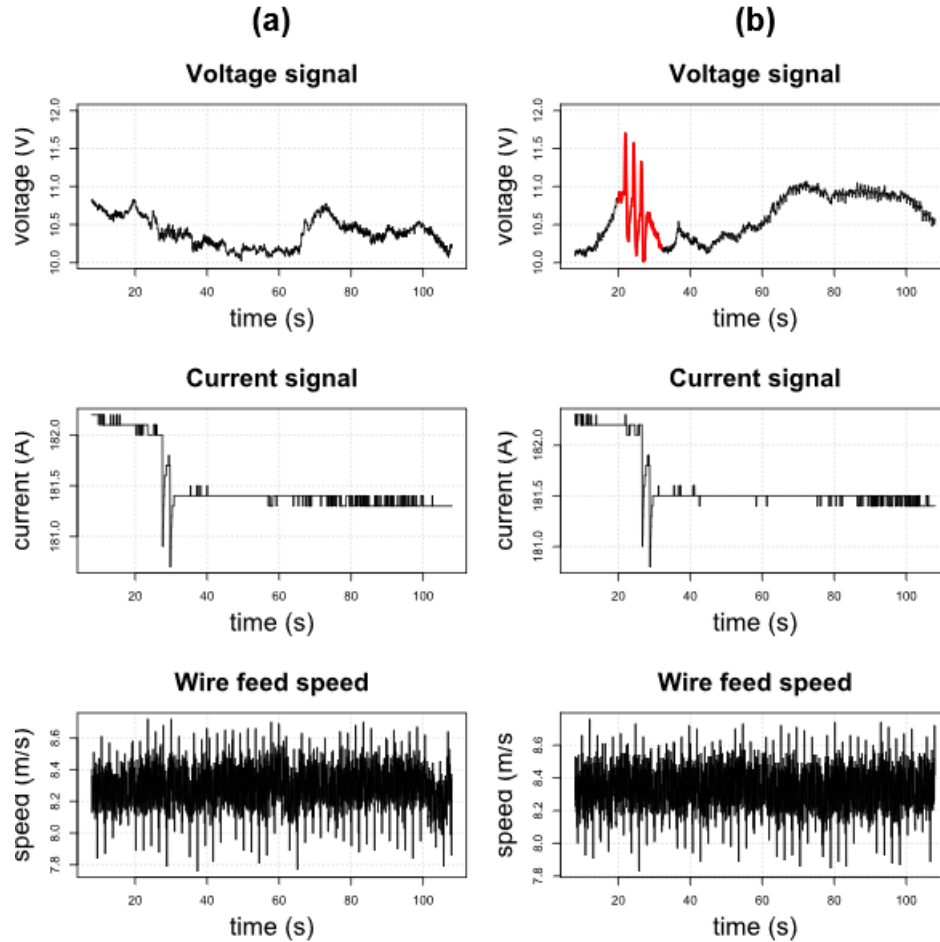


Figure 1.3: Examples of signals of a defect-free weld (a) and a weld with a burn-through (b).

the Augmented Dickey-Fuller to test stationarity against the null hypothesis that the time series has a unit root, which implies the non-stationary. The p-value of this test for the signal of good weld shown in Fig.1.3.(a) is equal to 0.5626. Therefore, the null hypothesis of the Augmented Dickey-Fuller test is accepted, which verifies that the voltage signal of the circular welding can be non-stationary. This has the implication that the burn-through peaks can have a value that is within the usual values of the signal.

In our exploratory analysis, we also found that in the case of welding with pulsed current, we also noticed that the pulse frequency is found in the voltage signals. This is shown by the periodograms

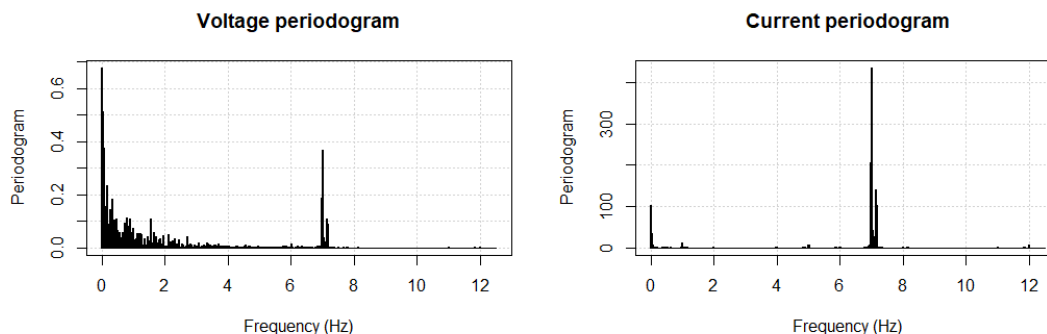


Figure 1.4: Periodogram of the voltage and current signals in the case of welding duplex water tanks.

in Fig. 1.4 where we see that the component at 7Hz is shared by both the current and the voltage signals.

In this work, we would like to detect burn-through in a two-level procedure, as depicted in Fig. 1.5. In the first level, we want to detect if there is a burn-through in the signal. If yes, in the second stage, we want to localize the burn-through by analyzing segments of the signal by a moving window. This procedure is adopted because we do not only want to detect burn-through in real-time, but we also want to make use of the historical signals to learn more about this defect in the considered process, namely by studying the signatures of the burn-through and its localization. We then need the detection method to be both fast and accurate. A part of the efficiency is then achieved by abandoning the uninteresting signals at the first stage, which would help accelerate the study.

Our work in this chapter is summarized as follows:

- We propose a fast and accurate method for burn-through detection based on signal filtering, probability density distribution, and the use of a functional data classifier.
- We conduct a study on the defect root cause and the information carried out by the signal with the aim of exploring the possibility of automating the root cause extraction from the welding signals.

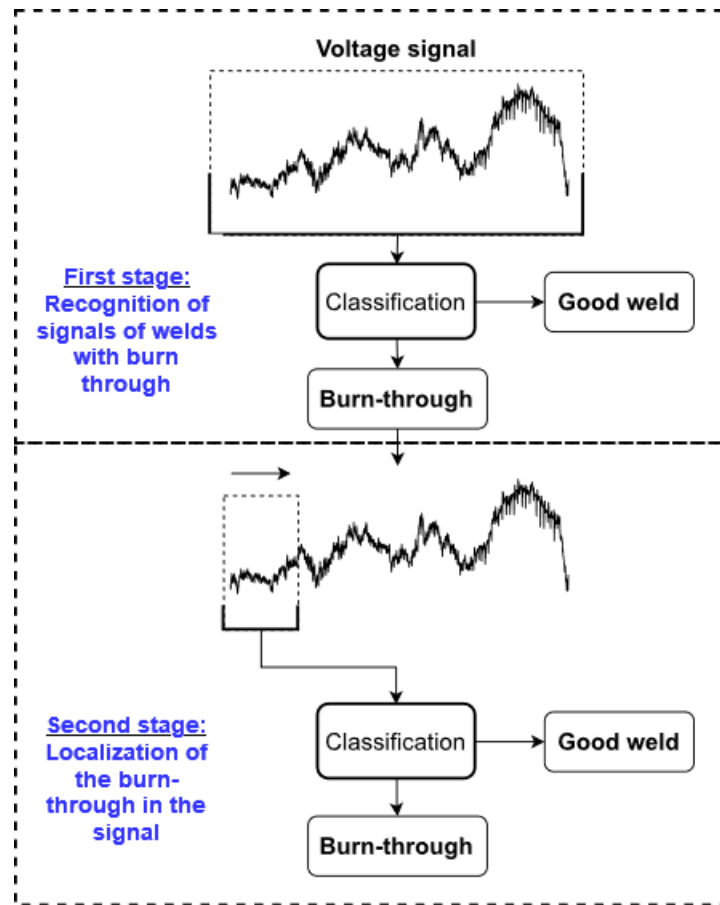


Figure 1.5: The proposed procedure for burn-through detection and localization.

- Based on root cause analysis, we propose solutions to prevent the burn-through occurrence.
- We show that in some cases, it is possible to anticipate the occurrence of the burn-through from the welding signals.

The chapter is organized as follows: in Section 1.2 we review relevant works about welding defect detection through the welding signals. We present the methods and materials in Section 1.3. The results of the proposed methodology along with a comparative study are given in Section 1.4. In Section 1.5 we conduct a study about root cause analysis, and we finish by conclusions.

1.2 Literature review on welding defect detection

Many efforts have been made to propose methods for welding quality evaluation and defect detection, mainly through the signals of welding key parameters such as voltage and current, which were found to correlate to the seam quality in arc welding processes (Sumesh, Nair, et al. (2018)). The techniques from the literature can be grouped into two main categories: Statistical Process Control and Machine Learning.

1.2.1 Statistical process control

The classical statistical process control (SPC) approaches were used in several recent works for the problem of welding defect detection. For instance, Z. Zhang, X. Chen, et al. (2014) use the control chart technique in the time and the frequency domain for the online detection of three forms of welding faults under pulsed GTAW. In the time domain, the pulse interference is eliminated with the help of the wavelet transform, then the variance of each segment of the filtered signal is monitored with the mean control chart. In the frequency domain, the root-mean-square is defined as the key feature and is monitored for each preset frequency band of the spectral density. It was found in their study that the voltage in the time domain has more sensitivity to the welding quality. Thekkuden et al. (2018) employed control charts to investigate their ability to detect porosity in GMAW under short circuit transfer mode. The mean and the standard deviation of voltage transient segments are computed and monitored by the control chart. The technique showed good results in detecting this type of welding defect. Guo et al. (2016) combine the Shewhart control chart with the Mahalanobis distance in order to monitor the quality of ultrasonic welding of lithium-ion batteries. However, the main disadvantage of control charts is the fact that they make assumptions about the data that are not always met such as normality and independence.

1.2.2 Machine Learning techniques

Machine Learning (ML) algorithms have gained considerable interest in the subject of welding defect detection. For instance, Pal et al. (2008) proposed a method named Neuro-wavelet, which

combines features obtained with wavelet transform on the current signal and the use of an Artificial Neural Network (ANN) to predict the tensile strength of weld joints. Sumesh, Nair, et al. (2018) studied the correlation of the current and voltage signals to the welding quality and constructed a decision tree model from 12 statistical features extracted from the raw signals. Under GMAW, Y. Huang, D. Yang, et al. (2020) developed a Support Vector Machine (SVM) classifier based on the multiscale entropy of the current and voltage signals to classify welds into four groups: porous, good, uneven, and spatter welding seams. The accuracy of the classifier was improved using the genetic algorithm for the optimization of the SVM parameters, which led to a final accuracy of 92.36%.

After observing that the waveforms in the voltage signal are irregular when there is porosity in the weld, Shin et al. (2020) extracted 12 statistical features to assess the regularity of the voltage signals in a GMAW process and studied the correlation between these features and the porosity rate. Based on the correlation, 6 features were then retained to develop a neural network to automatically detect porosity. Y. Huang, X. Wang, et al. (2021) used local mean decomposition to decompose the current signal into a series of product functions and employed multiscale entropy of a set of the latter to train a deep belief network to classify the signals into four categories: surface porosity, poorly formed, well-formed, and wider weld. Jin, Shin, et al. (2020) transform the current signal acquired during GMAW into scalograms using Morlet wavelet transform and use a convolutional neural network to detect under penetration. Jin and Rhee (2021) extracted 24 features from both voltage and current signals from time and frequency domains, which were used afterward to develop an ANN to predict the gap between the pieces during welding. K. Chen et al. (2019) used 6 features from current, voltage, and energy to train an XGBoost model to predict the coefficient of penetration that they defined as the ratio of penetration depth to the plate thickness.

Y. Li et al. (2022) proposed an incremental learning approach based on linear SVM and 13 features extracted from voltage and current signals to detect defects in Cold Metal Transfer (CMT) welding. Moinuddin et al. (2021) used statistical features from current and voltage signals and trained an SVM and decision tree models to detect porosity, burn-through, and lack of penetration. Arabaci et al. (2019) pointed out that the use of statistical characteristics extracted from current signals of the GMAW may fail to capture the difference between categories of welding data. Based on this statement, they attempt to categorize welding defects based on the use of Principal Component

Analysis (PCA) on raw current signals. Thirty experiments composed of six categories of welding were conducted and the acquired current signals are reduced by PCA. The scores obtained from the projection of signals on several first eigenvectors were classified using SVM, decision trees, and k -Nearest Neighbors (k -NN) whose accuracy was the highest.

In addition to welding electrical signals, arc sound was found informative of the welding quality (Sumesh, Rameshkumar, et al. (2015)). Pernambuco et al. (2019) suggested the use of ANN for the classification of sound signals into three welding conditions; good weld, with oil, and without shielding gas under GMAW. The classification was studied for different modes of metal transfer, and the results showed higher accuracy of the trained ANN when the welding is carried out with the short circuit transfer mode. He et al. (2019) proposed a strategy where real-time acquired sound signal segments are transformed by synchrosqueezed wavelet transform to get the time-frequency distributions, which are reduced by the PCA afterward. The approximate entropy computed from the obtained principal components was used as a feature vector for the training of an SVM model. Cocota Jr et al. (2017) used wavelet transform and Fourier transform to extract features from sound signals to train ANN and SVM models for the detection of discontinuities during the Shield Metal Arc Welding Process. W. Ren et al. (2020) proposed to transform the sound into a Time-Frequency spectrogram and the use of a convolutional neural network to classify the penetration level of the welding.

Instead of using only welding parameters' signals or only the sound signals for defect detection, Z. Zhang and S. Chen (2017) defined a strategy to identify penetration quality based on the fusion of multi-sensor data. Arc sound, voltage, and light signals were used in their study. The extracted features from each signal are combined to train an SVM model with 10-fold cross-validation. The data fusion model was compared to models trained from each sensor data separately and was found more accurate, with an accuracy of 96.5% against 92% when using only the sound signal. Cui et al. (2020) carried out another recent work based on multi-sensor data fusion. They use the combination of current, voltage, and sound signals in order to identify the lack of penetration, full penetration, and excessive penetration in Keyhole TIG welding. The features extracted from the signals were reduced using principal component analysis. The accuracy of the SVM model used for the classification was found dependent on the retained number of principal components. Surovi et al. (2022) extracted multiple features from the sound signal such as energy, mean, and kurtosis,

and combined them with process parameters to detect welding defects.

Despite the conducted works, real-time welding quality control remains a difficult task due to the complexity of the physics of welding and the interdependence between its different parameters (Mirapeix et al. (2007)). The ML models for welding defect detection are often based on the classification of some statistics extracted from the welding signals. This methodology might fail because the statistical features may not accurately capture the difference between defect-free and defective welding signals in real industrial processes (Arabaci et al. (2019)) mainly when the length of the signal is high. Moreover, most of the studies are done on deliberately made defects, which may not reflect the real behavior of the welding process. Furthermore, as the defects are often deliberately made, there is a lack of root cause studies in most of the works.

1.3 Methods

In order to overcome the shortcomings of the existing methods that are relying on the classification of the welding signals from some features extracted from them, which might fail to distinguish between defect-free and defective weld signals. We propose in our work to classify the signals based on their probability density distribution (PDD). This is motivated by our first observations that the burn-through appears as peaks in the signals. Hence, when working with the PDDs of the signals, we expect them to exhibit heavy tails when there is a burn-through, which makes the PDD an interesting discriminatory characteristic of the signals. To that end, we use Kernel Density Estimation to estimate the PDDs of the signals and the functional non-parametric kernel classifier to classify the PDDs.

1.3.1 Kernel Density Estimation

Kernel Density Estimation (KDE), also called Parzen estimator, proposed by Parzen (1962), is the most used non-parametric method for estimating the probability density distribution (PDD) of a given independent and identically distributed (i.i.d) univariate sequence. It is given by the following

equation:

$$\widehat{PDD}(x) = \frac{\sum_{i=1}^n K(h^{-1}(x - x_i))}{nh} \quad (1.1)$$

where:

- K : The kernel function,
- x : The point where density is estimated,
- h : The bandwidth (also called the smoothing parameter),
- n : The length of the sample,
- x_1, \dots, x_n The i.i.d sample, which is a preprocessed signal in our case.

The bandwidth value determines the resolution of the density distribution function. The larger the value of the bandwidth, the more the PDD is smooth. This parameter is more important than the kernel type in the KDE method (Węglarczyk (2018); Kamalov (2020)). Several techniques exist for the estimation of the optimal value of the bandwidth h . In our study, we consider the optimal bandwidth value to be the value that leads to the highest classification accuracy. The Gaussian kernel is the most used for the estimation of the probability density distribution because it is distributed over the whole x-axis, which makes it the most suitable for KDE (Węglarczyk (2018)) and will be then used in our study. After estimating the PDD of the signals, we use the functional non-parametric kernel classifier in order to classify them.

1.3.2 Functional non-parametric kernel classifier

Ferraty et al. (2003) introduced the non-parametric functional data classifier that we use in this study, which is based on distances between functional observations and the use of a kernel function to determine the posterior probabilities that a new curve belongs to one of the predefined classes. Let Y_i be a categorical response taking values in $\hat{G} = (1, \dots, G)$ and X_i the associated functional observations, which is in our case PDDs. The probability that a new functional observation X

belongs to the class g in \hat{G} is given by the following estimator:

$$\hat{P}(g|X) = \frac{\sum_{i=1}^n \mathbb{1}_{Y_i=g} \times K(h^{-1}d(X, X_i))}{\sum_{i=1}^n K(h^{-1}d(X, X_i))} \quad (1.2)$$

where:

- $\hat{P}(g|X)$: The posterior probability that a curve X belongs to class g ,
- K : The kernel function,
- h : The smoothing parameter,
- $\mathbb{1}_{Y_i=g}$: The Heaviside function that equals 1 when the curve X_i belongs to class g ,
- $d(X, X_i)$: Distance between the PDD X and the PDD X_i with $i=1, \dots, n$, where n is the number of the training curves). We use the Euclidean distance (L_2) in our classification problem, which is given by:

$$\|X - X_i\|_2 = \sqrt{\frac{1}{\sum_{j=1}^m w^j} \sum_{j=1}^m (|X^j - X_i^j|)^2 \times w^j} \quad (1.3)$$

where:

- w : A vector of weights having the same length as the functional observations,
- m : The length of the functional observations.

We choose the L_2 distance since we classify the PDDs and not the original signals. The PDD aligns the signals since it does not take into account the time. Thus, we do not need a distance measure intended for the alignment. To show that, consider two simulated signals $f_1 = \sin(2\pi t)$ and $f_2 = \sin(\pi(2t - 0.5))$, which is exactly f_1 with a phase shift of 0.5π . Fig. 1.6 shows the two signals and their PDDs. We notice that the PDDs of the two signals are aligned, which confirms the suitability of the L_2 distance.

Usually, the Kullback-Leibler divergence is used to measure dissimilarity between PDDs. However, for our particular problem, the L_2 distance is well-suited because we are only interested in detecting if a PDD has a heavier tail compared to PDDs of defect-free signals.

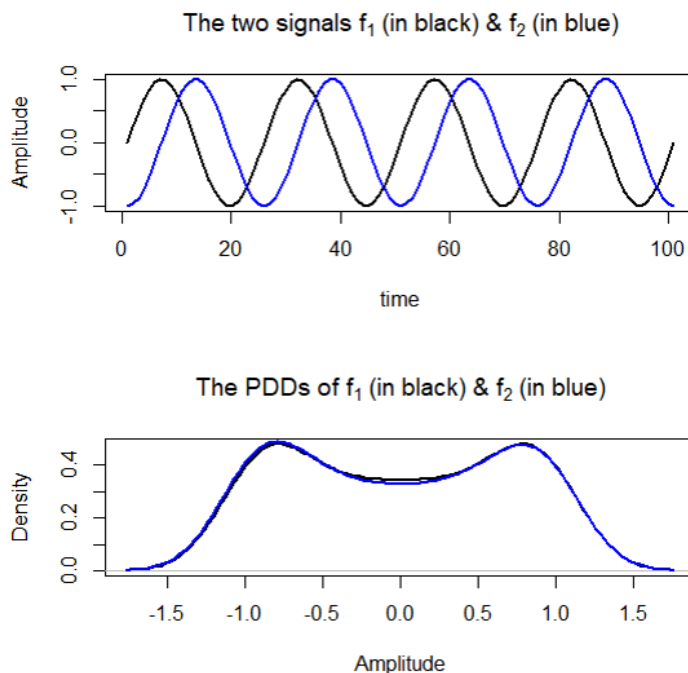


Figure 1.6: The two sinusoidal signals and their PDDs.

The classifier in Eq. 1.2 is based on Bayes theorem and is a generalization of the one proposed by Hall et al. (2001) who formulated the problem of curve discrimination in terms of the posterior probability estimation where $\sum_{i=1}^n \mathbb{1}_{Y_i=g} \times K(h^{-1}d(X, X_i))$ is the likelihood that a new curve X belongs to a given class g . They used a uniform prior equal to $\frac{1}{\text{number of classes}}$. The arguments that motivate our choice for this classifier is that Hall's classifier uses the projection of the curves, into a basis to be chosen, for the classification, whereas the classifier in Eq. 1.2 uses directly the original curves, which means that it avoids the loss of information due to the projection and the problem of selecting the proper projection basis.

The idea behind this classifier as explained by Ferraty et al. (2003) is that in order to obtain the posterior probability that a curve belongs to a given class g , we only need the curves of the class g from the training data at a distance of at most h from X (i.e $d(X, X_{i \in g}) \leq h$). The likelihood increases with the closeness between X and $X_{i \in g}$. The curve is then assigned to the class $\hat{Y}^h = g$

where $\hat{P}(g|x)$ is the highest:

$$\hat{Y}^h = \arg \max_g (\hat{P}(g|X)) \quad (1.4)$$

Where h is the used value of the smoothing parameter in the posterior probability computation. This classifier is built by optimizing the value of h , which is done by minimizing the error criterion defined for a given training sample I of pairs $(X_i, Y_i)_{i \in I}$ by the equation:

$$E(h) = 1 - \frac{1}{|I|} \sum_{i \in I} \mathbb{1}_{Y_i = \hat{Y}_i^h} \quad (1.5)$$

Where:

- $|I|$: The number of elements in I ,
- Y_i : The real categorical response of the curve X_i ,
- \hat{Y}_i^h : The predicted categorical response of the curve i using the bandwidth value h ,
- $\mathbb{1}_{Y_i = \hat{Y}_i^h}$: The Heaviside function that equals 1 when the predicted categorical response of a curve X_i is correct.

The minimization of $E(h)$ is then done by cross-validation, which produces an optimal smoothing parameter h^{opt} and a minimum classification error $E(h^{\text{opt}})$.

Finally, we note that with the normalization factor $\sum_{i=1}^n K(h^{-1}d(X, X_i))$, the estimated probabilities satisfy the rule of total probability:

$$\sum_{g=1}^G \hat{P}(g|X) = 1 \quad (1.6)$$

To give an illustration of the method, consider the example shown in Fig. 1.7. For an incoming curve in a binary classification problem, the posterior probability \hat{P}_g is estimated as the ratio between the likelihood, which is the sum of smoothed distances (by the kernel) between X (the incoming curve) and the curves X_i of the class g at most h from X , and the sum of smoothed distances between X and all X_i at most h from X . For a numerical application, we use the Gaussian kernel and $h = 1$ for this example. The likelihood that the incoming curve belongs to the class

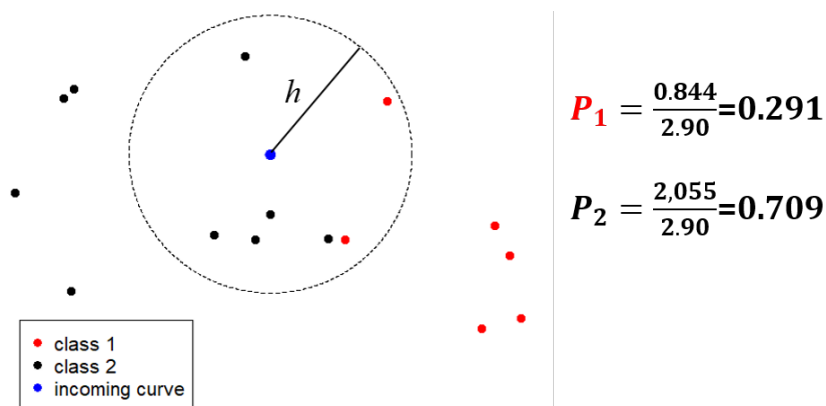


Figure 1.7: An example of classification using the non-parametric kernel classifier.

1 (in red) $\sum_{i=1}^{15} \mathbb{1}_{Y_i=1} \times K(h^{-1}d(X, X_i))$ is equal to 0.844 whereas the likelihood that it belongs to class 2 (in black) $\sum_{i=1}^{15} \mathbb{1}_{Y_i=2} \times K(h^{-1}d(X, X_i))$ is equal 2.055. The posterior probabilities are then estimated as the odd ratio: $\hat{P}(Y = 1|x) = \frac{0.844}{2.90} = 0.291$, $\hat{P}(Y = 2|x) = \frac{2.055}{2.90} = 0.709$. As discussed above, the incoming curve is assigned to class 2 where the posterior probability is the highest. Overall, the classifier can be seen as a probabilistic extension of the classical k -nearest neighbors classifier.

1.3.3 Pipeline of burn-through detection

As discussed in the introduction, the problem of welding burn-through detection and localization requires a method that captures the presence of sudden peaks in a signal and extracts the part where they appear. The central idea of our methodology is the use of the PDDs estimated from the signals to detect and localize the defects. If the signal is stationary, the defect peaks will appear at the tails of the PDD regardless of where they are in the signal thanks to the alignment obtained by the PDD as shown in the methods section. This holds whether we work with the whole signal or a segment of it. Hence, we can use the two-stage approach where the first stage detects if a signal contains peaks that indicate a burn-through, if yes, the signal is segmented and each segment is processed in the second stage to localize the peaks.

Based on the above analysis, we define the adopted methodology for data processing and classi-

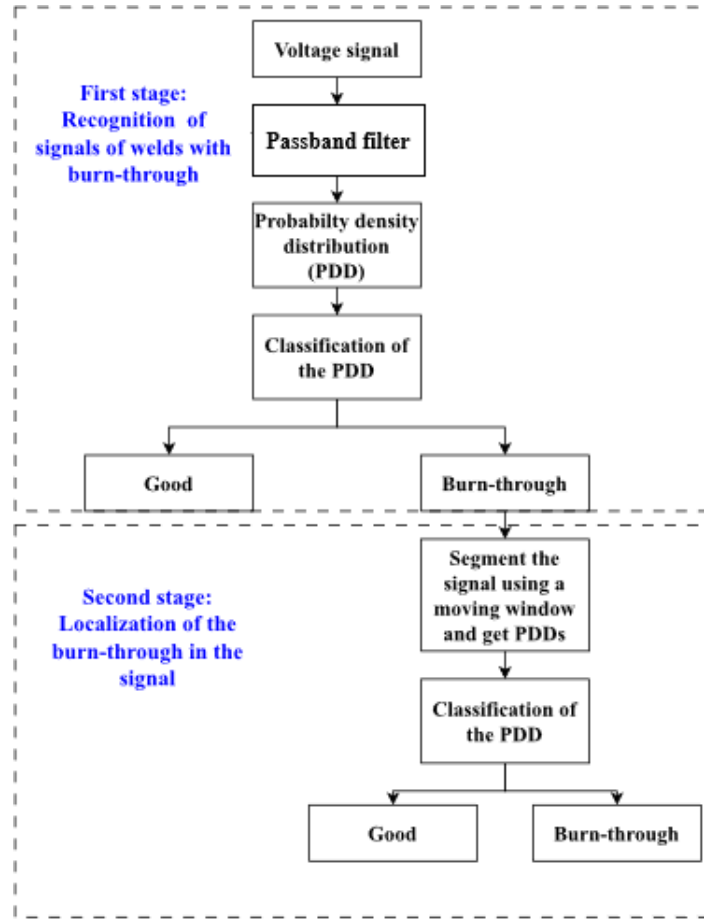


Figure 1.8: Diagram of the adopted methodology for defect detection and localization.

fication in Fig. 1.8. In the first stage, we are interested in predicting if a signal is generated from a defective or defect-free weld. For this purpose, we begin by eliminating the high frequencies and the trend from the signal in order to make it stationary, which can be achieved using a pass band Butterworth filter. We want the signal to be stationary in order for our assumption that the PDDs of defective weld signals having a heavy tail, because of the burn-through peaks, would hold. The PDD composed of 64 points is afterward obtained from the filtered signal using the KDE method with the Gaussian kernel and a value of the bandwidth leading to the highest classification accuracy. The PDD is then classified using the functional classifier as either corresponding to a good or a defective welding signal.

In the second stage, we seek to find the part of the signal where the burn-through occurred as follows: if a PDD is classified as non-conforming, the corresponding signal is split into segments of 200 points (corresponding to 8 seconds) using an overlapping sliding window moving by 100 points. The size of the window was determined by observation, ensuring that a defect is always captured by the window. PDDs estimated from each signal segment are then classified as either containing the burn-through or not, which will allow us to detect the part of the signal where the burn-through occurred. The filter is not needed in this stage because of the small length of the signal segments.

1.4 Results and discussion

1.4.1 Preliminary study of the methodology

An example of a processed signal according to the defined methodology of each of the two categories of the austenitic hot water tanks is shown in Fig.1.9. The passband filter removes both high frequencies and the dominant trend components from the original signal. The PDD of the good weld shows that the signal is centered in the range of 10-10.8V whereas the PDD of the nonconforming weld shows contributions of values at the right tail of the distribution, which indicates the presence of the defect peaks in the signal. Note that the logarithmic transformation is needed in order to highlight these small values in the PDD.

To verify the discrimination ability of the methodology, we apply the Functional Principal Component Analysis (FPCA) on a set composed of 10 PDDs of signals of good welds and 10 PDDs of signals of defective welds carried out on duplex tanks. The FPCA gives the two principal functions and the variation projection shown in Fig. 1.10. The principal function 1 captures 63.4% of the variations in the curves. The PDDs having a positive variation with respect to this function have a higher density of values that are far from the mean. Knowing that trends were removed from the original signals, this indicates the sudden fluctuations or peaks in the original signal that are the result of the disturbance of the electric arc when the defect occurs. The second function shows the variation in the standard deviations of signals; curves with negative variations have a smaller standard deviation. We notice that the PDDs of defective welds (marked in red) are naturally

CHAPTER 1. STUDY OF THE BURN-THROUGH DETECTION IN THE CIRCULAR WELDING

discriminated from those of defect-free, as can be seen from the projection on the two FPCA functions in Fig. 1.10. This shows the ability of the probability density distributions to categorize the welding quality. We also notice from the FPCA functions that the PDDs of good welds and those of welds with burn-through are different almost over the whole voltage axis. Hence, in the distance computation for the classification, we use no specific weights. The weight vector in Eq 1.3 is then fixed to $w^j = 1 \forall j$.

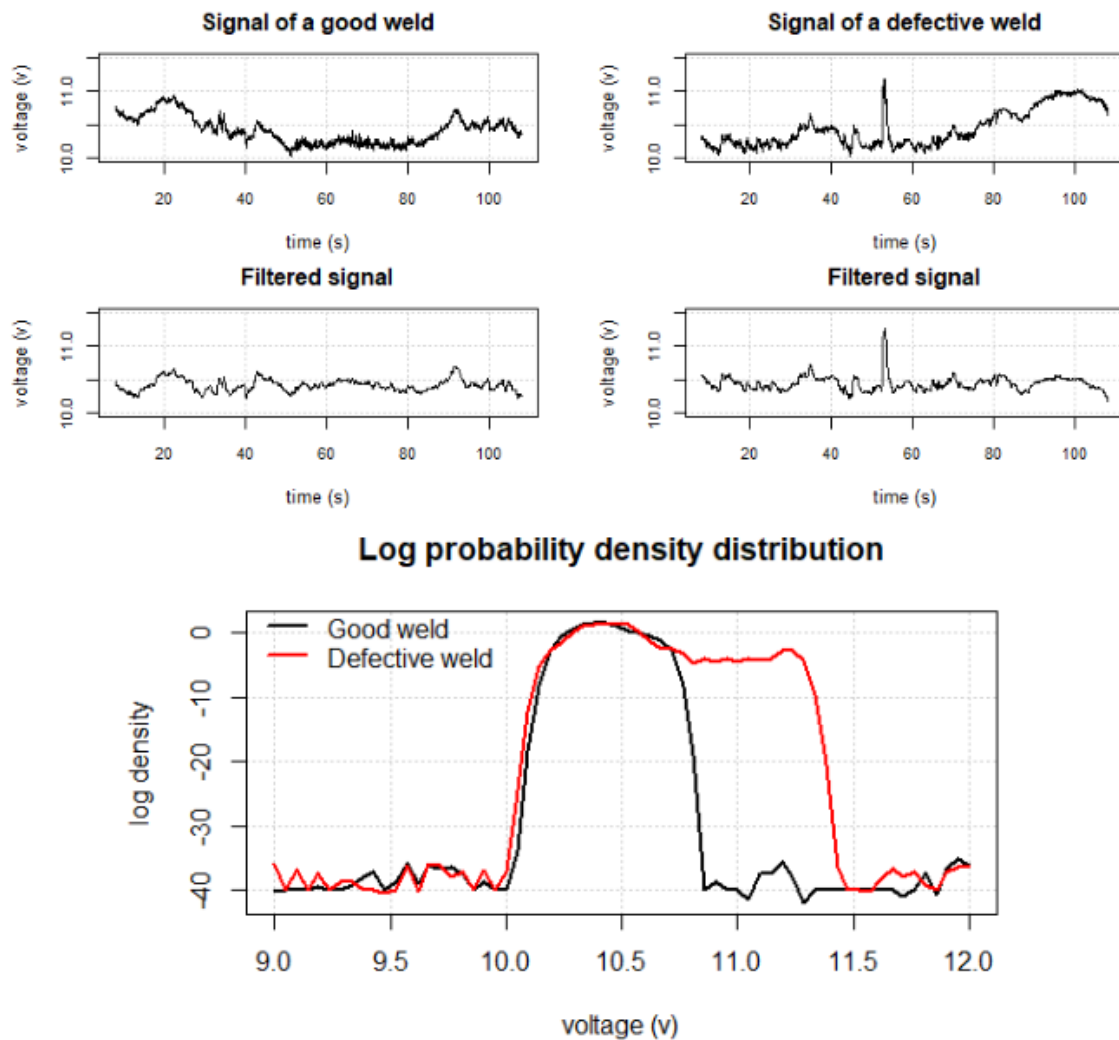


Figure 1.9: Example of processed signals according to the proposed methodology. The PDDs are log-transformed.

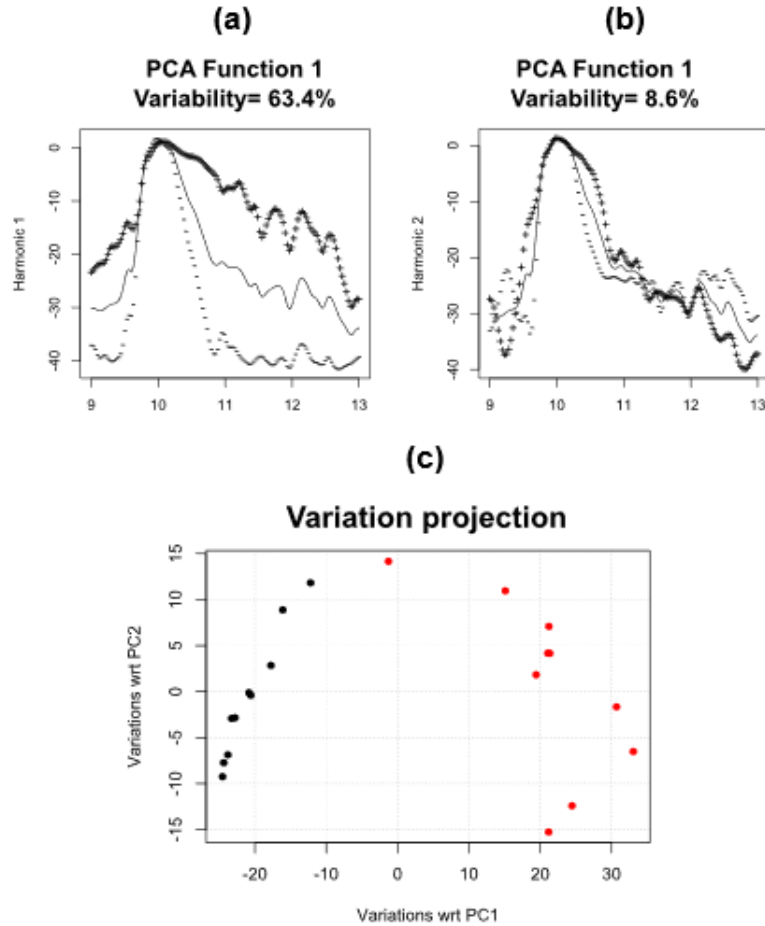


Figure 1.10: (a) The first FPCA function. (b) The second FPCA function and the variation projection (c).

1.4.2 Results

We consider in this study 160 signals generated from the welding of austenitic tanks (equivalent to 80 tanks) and 300 signals when welding duplex tanks. For each of the two data sets, half the number of the signals corresponds to welds with burn-through. As for the creation of classification models, 70% of the total number of signals are used for training, while the remaining 30% is for testing.

Following the methodology described in Fig. 1.8, two functional kernel classifiers are created using the Gaussian kernel and values of bandwidth h optimized on the training data. The first model classifies the PDDs of the austenitic tanks' welding signals, and the second classifies those of the duplex tanks' signals. In what follows, the classifiers are called classifier A and classifier D for clarity (A for Austenitic and D for Duplex). Table 1.2 and Table 1.3 give the results for the training and the test of the models. No misclassification of the austenitic tanks signals and only one duplex tank signal is misclassified in the test data for the second model, resulting in an accuracy of 100% and 98.86% respectively. These results confirm the suitability of the method for the detection of burn-through. Furthermore, the ROC curves (Receiver operating characteristics) of the two classifiers in Fig. 1.11 confirm the perfect performance of the classifiers.

There are three parameters that can influence the classification accuracy in the presented methodology: the pass band of the filter, the range of the PDD, and its bandwidth value. Prior knowledge of the range in which the signals evolve helps in selecting the range of the PDD; we define a range from 9v to 11.5v for austenitic tanks signals and a range from 6v to 15v for those of the duplex tanks. Tuning the pass-band of the filter also needs prior knowledge of the pulse and the wire feed frequency bands to eliminate in order to avoid their interference with the voltage signal. The filtered signal must also attenuate the trend of the original signal in order to prevent the appearance of values at the tails of the PDD for a defect-free welding signal. This can be done by eliminating the 0 Hz frequency component that contains the trend, i.e. by setting the first cutoff of the filter

Table 1.2: The confusion matrix of the classifier A.

Categories	Training		Test	
	Good	Defective	Good	Defective
Good	56	0	24	0
Defective	0	56	0	24
Accuracy	100%		100%	

Table 1.3: The confusion matrix of the classifier D.

Categories	Training		Test	
	Good	Defective	Good	Defective
Good	106	0	44	1
Defective	0	106	0	43
Accuracy	100%		98.86%	

Table 1.4: Optimal parameters of the two classifiers.

Parameters	Classifier A	Classifier B
Pass-band of the filter	0.025-1.75Hz	0.025-1.75Hz
Bandwidth of the PDD	0.1	0.02
Range of the PDD	9V-11.5V	6V-15V
Classifier's optimal bandwidth	9.045	22.356

at a frequency greater than 0 Hz. Here, the pass-band is determined to be from 0.025Hz to 1.75Hz for both signal types. If the information on the pulse and the wire feed frequency is not available, one can estimate the passband using cross-validation.

The last parameter to be tuned is the bandwidth of the PDD. In Fig. 1.12 we show how the accuracy of the classifiers change when varying this parameter, we notice that an accuracy of 100% is achieved when the bandwidth is between 0.005 and 0.2 for classifier A. Classifier D exhibits more sensitivity to this parameter as can be seen from the curve, its optimal accuracy is obtained when the bandwidth is set to 0.02. The optimal parameters for the two classifiers are summarized in Table 1.4.

In practice, it might be expensive to collect and annotate a large number of welding signals. It is then interesting to study the effect of sample size on the accuracy of the classification. Considering

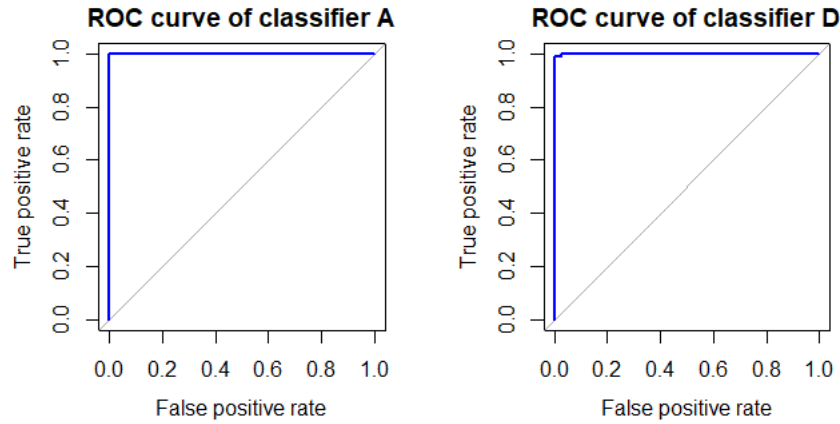


Figure 1.11: The ROC curves of the classifiers A and B.

the classifier A and the 160 austenitic tanks signals, we vary the training sample size from 4 to 112 while keeping the test sample at 48. For both the training and the test datasets, 50% of the PDDs correspond to nonconforming welds. We study the accuracy of the classifier of each partitioning by keeping the optimal parameters discussed above identical except for the value of the classifier's smoothing parameter h , which is optimized by cross-validation for each training set as discussed in the methods. Fig. 1.13 shows the test accuracy as a function of the training sample size. We notice that with only 4 curves, we obtain an accuracy of 95,8% on the 48 signals. The 100% accuracy of the classifier becomes stable with a training sample size of 28. These results show that the methodology can handle the problem of small sample size thanks to the good discrimination provided by the PDDs.

As discussed in the methodology description, if a PDD belongs to the nonconforming group, we are interested in capturing the location of the defect in the signal, which is important information for the study of defect causes, for example, if defects occur at the beginning of the welding cycle then the welding torch would be the most probable cause and needs then to be changed or repaired.

In this second stage, the signal of the defective weld is split into segments of 8 seconds using an overlapping sliding window moving by 4 seconds, which are transformed into PDDs that are subsequently classified in order to obtain the location of the defect. In this context, two other functional kernel classifiers that we call defect localizers A and D are created to process the signals of welds with burn-through of austenitic and duplex water tanks respectively. A total of 60 PDDs

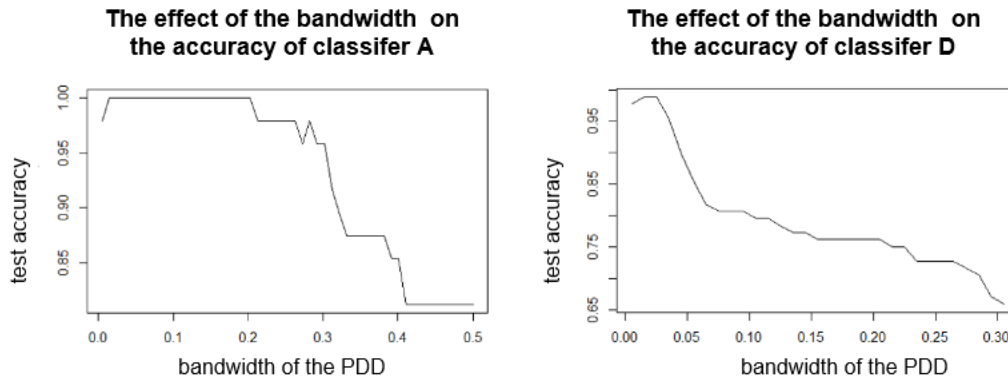


Figure 1.12: The effect of the PDD's bandwidth on the classifiers' accuracy.

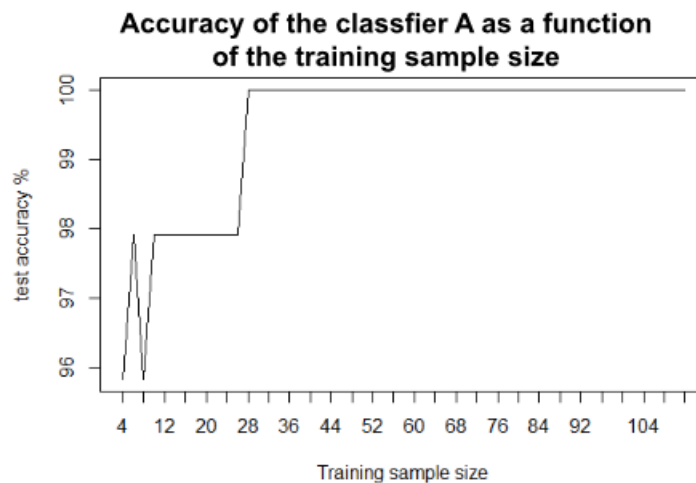


Figure 1.13: The effect of the training sample size on the accuracy of the classifier A.

Table 1.5: The confusion matrix of the defect localizer A.

Categories	Training		Test	
	No defect	Defect	No defect	Defect
No defect	22	0	8	0
Defect	0	22	0	8
Accuracy	100%		100%	

Table 1.6: The confusion matrix of the defect localizer D.

Categories	Training		Test	
	No defect	Defect	No defect	Defect
No defect	22	0	8	0
Defect	0	22	0	8
Accuracy	100%		100%	

are used for each model, with 70% of them for the training and 30% for the evaluation, with equitable distribution of the two categories in the two steps. The signal segments are transformed into PDDs without the application of a filter because of their small length. We maintain the use of the Gaussian kernel for both the PDD estimation and the functional kernel classifier and the same PDD bandwidths as in the first stage classification. The confusion matrices for training and validation are shown in Table 1.5 and Table 1.6.

Both defect localizers had 100% accuracy in the training and validation phases. This perfect

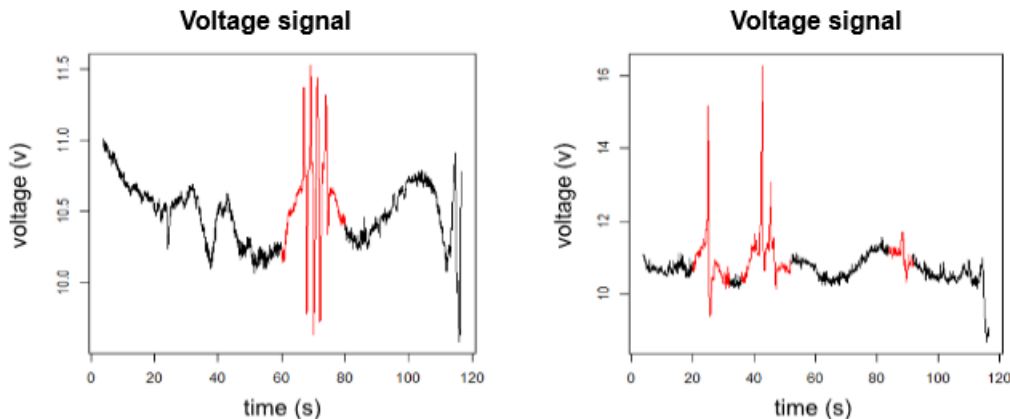


Figure 1.14: Signals of defective welds where burn-through are localized (shown in red).

accuracy is encouraging for the use of this methodology as an online fault detection, where segments of a signal are transformed into PDDs and classified in real time. Fig. 1.14 shows an example of two signals of a defective weld where the burn-through are detected by the localizer and colored in red.

1.4.3 Comparative study

We compare here the proposed approach with the most used ones for the classification of welding signals, which are based on the classification of the signals based on some extracted features from them as seen in the literature review. For this purpose, we consider a feature vector composed of the mean, standard deviation, energy, and entropy of the voltage signals. For the classification of the input features, we use several classifiers: SVM with both the linear and the radial basis kernels, Logistic Regression, Random Forest with 500 trees, and k -NN with $k=2$. We use the same datasets that we used to create our models in the previous section, which is composed of 160 voltage signals of austenitic tanks and 300 voltage signals of duplex tanks. for both datasets, 70% of the signals are used for training, while the remaining 30% for testing. Table 1.7 shows the accuracy for each technique. Our approach outperforms the other ones for both datasets and has very high accuracy. These results confirm the disadvantages of the feature extraction strategy for the classification of non-stationary welding signals because the statistical features may not accurately capture the

difference between defect-free and defective welding signals. We notice that the other classifiers perform better for the signals of duplex tanks, which is explained by the fact that these signals have less degree of non-stationarity than the signals of austenitic tanks. This is because the welding machine of this type of tanks is equipped with an automatic voltage control. Moreover, the peaks indicating the defects can have a high amplitude in this dataset, which makes the classification relatively easier than when working with the signals of austenitic tanks.

We showed in the previous subsection that our methodology has the ability to generalize from a small training sample. To confirm this result, we compare it to the other techniques using a training set composed of only 10% of the whole dataset for each tank type (resulting in 15 out of the 150 austenitic tanks' signals and 30 for those of duplex tanks). The remaining 90% are used for testing. Table 1.8 shows the test accuracy of each technique for this configuration. The accuracy of our methodology remains very high for the two datasets while the other techniques fail to learn from small training samples, especially in the case of austenitic tanks' signals. The other methodologies still perform better for the signals of duplex tanks than for those of austenitic tanks, for the reasons discussed earlier.

The results of this comparative study confirm the good performance of the proposed methodology

Table 1.7: Comparison with other techniques.

Methodology/Dataset	Signals of austenitic tanks	Signals of duplex tanks
Proposed	100%	98.86%
SVM (radial basis kernel)	81.25%	92.04%
Logistic regression	79.10%	90.90%
SVM (linear kernel)	77.00%	89.77%
Random Forest (500 trees)	77.00%	89.77%
k -NN ($k=2$)	66.66%	73.06%

Table 1.8: Comparison with other techniques when training on 10% of the whole dataset.

Approach/Dataset	Austenitic tanks	Duplex tanks
Proposed approach	94.44%	98.13%
SVM (radial basis kernel)	70.83%	86.94
Logistic regression	70.83%	89.17%
SVM (linear kernel)	58.33%	88.80%
Random Forest (500 trees)	59.02%	88.05%
k -NN ($k=2$)	75.00%	70.98%

for the detection of burn-through in welding signals that can be non-stationary and nonlinear and its ability to handle the problem of small sample size, which is very useful for industrial welding where data collection may be expensive and time-consuming.

To summarize, the main advantages of the proposed methodology are the high reduction in the length of the signals and this by transforming them into PDDs consisting of only 64 points, resulting in fast processing of data. The application of the whole methodology from the preprocessing to the defect localization on 100 voltage signals is done in 0.41 seconds only. Moreover, results show that the methodology has very high accuracy and can generalize well when trained on a small sample. In the next section, we study the subject of root cause analysis with the help of the presented approach for burn-through detection.

1.5 Burn-through root cause in the circular welding of hot water tanks

We are interested in this section in the study of the burn-through root cause for the austenitic hot water tanks. Using the presented methodology, we localized the burn-through in 200 historical voltage signals of 200 defective circular welds. Fig. 1.15 shows the histogram of defect localization in the signals. We notice that there is a peak at the time interval between 30 and 40 seconds. This is where the circular welding meets the longitudinal weld of the cylinder. Since the positioning of the cylinder in the circular welding machine can be slightly different each time, the physical localization of the defects appearing in the time interval from 20 to 50 seconds can be considered as the zone of the intersection with the longitudinal weld or nearby. More than 60% of the defects are then situated in this zone.

We noticed that the patterns of the burn-through in the signal can be classified into two types, as Fig. 1.16 shows. The first type is characterized by a gradual increase before the appearance of the peaks (highlighted in orange). In the second type, the defect peak appears suddenly.

Since the voltage is correlated to the length of the electric arc, the gradual increase in the first defect signal type means that there was a gradual misalignment between the cap and the cylinder.

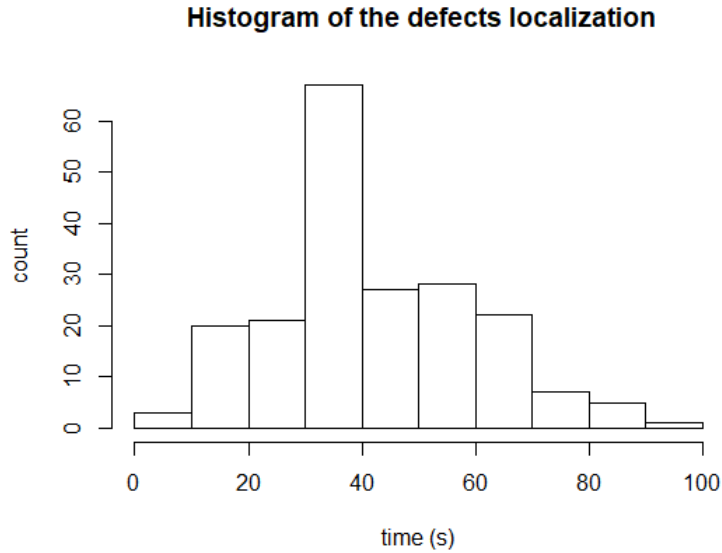


Figure 1.15: Histogram of the defects' localization.

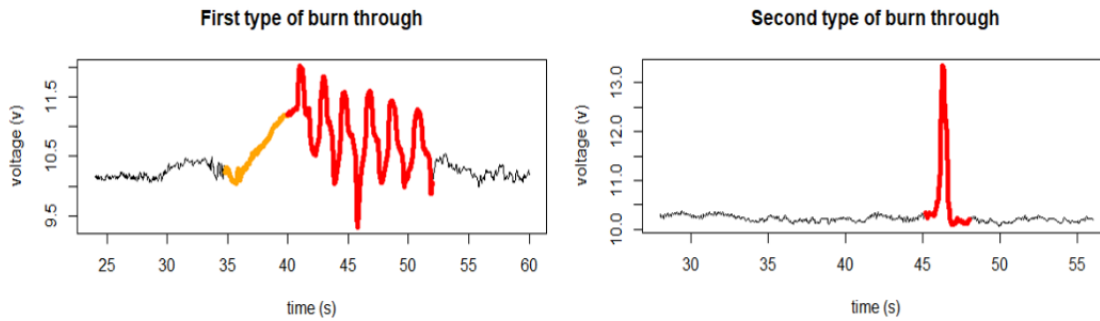


Figure 1.16: The two types of burn-through in the signals.

This happens when one of them is not perfectly circular. The gap between them increases until the welding pool collapses before it comes back to normal when the misalignment decreases as illustrated in Fig. 1.17. The second type indicates that a sudden discontinuity caused the defect. Fig. 1.18 shows an example of each of the defect types. We can see the gradually increasing misalignment until the burn-through in the first type. We also notice that the misalignment begins shortly after the intersection with the longitudinal weld. In the second type, we notice that the defect appears exactly at the intersection with the longitudinal weld and that there is no significant misalignment

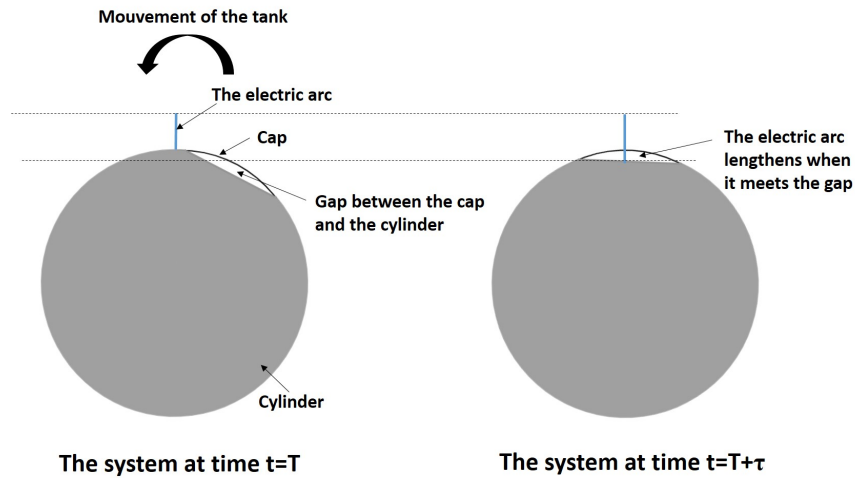


Figure 1.17: An interpretation of the first type of burn-through signature.

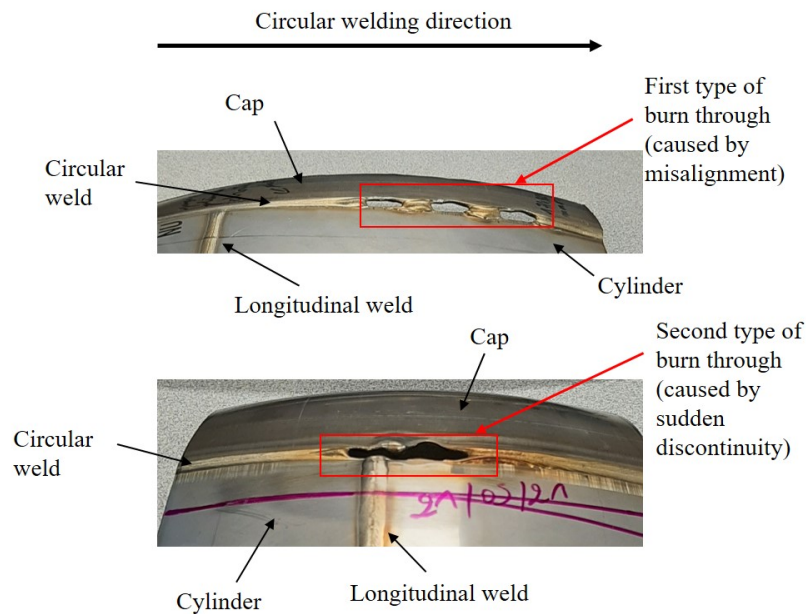


Figure 1.18: The two types of burn-through shown in real pieces.

between the cap and the cylinder.

From these analyses and the histogram in Fig. 1.15, we conclude that most of the defect occurrences caused by the misalignment are generated by a distortion of the cylinder due to the

CHAPTER 1. STUDY OF THE BURN-THROUGH DETECTION IN THE CIRCULAR WELDING

longitudinal welding process. The second type can be caused by a tear of the longitudinal weld, as shown in Fig.1.19, which can occur when the operator removes the run-on and run-off tabs used in the longitudinal welding or when he attempts to redress the shape of the cylinder at this zone. Soni et al. (2013) also found in their study on a similar product that one of the causes of defects is the improper removal of the run-on and run-off tabs. They proposed in their case the use of a gas cutter for this task as a corrective action. The tabs are used to ensure full penetration. However, incomplete penetration might still occur, and it would be a potential cause along with other types of defects at the beginning or the end of longitudinal welding, such as cracks.

An important observation is that the first type of burn-through can be anticipated, and this by detecting the gradual increase of the voltage and predicting the time at which the defect peaks would appear. This can be addressed using techniques from a concept of predictive maintenance called Remaining Useful Life (RUL) estimation, where the goal is to predict the time before the failure of equipment. Another interesting approach would be the early classification of the signal.

We were also interested in this study in searching the cause of the burn-throughs that are not at the intersection with the longitudinal welding. Using the developed method for burn-through detection, we searched in the available data and found that there are signals where the defect is localized always at the end of the cycle, as Fig. 1.20 shows. We notice that the burn-throughs are of the first type defined earlier. This means that there is a misalignment that causes the burn-through

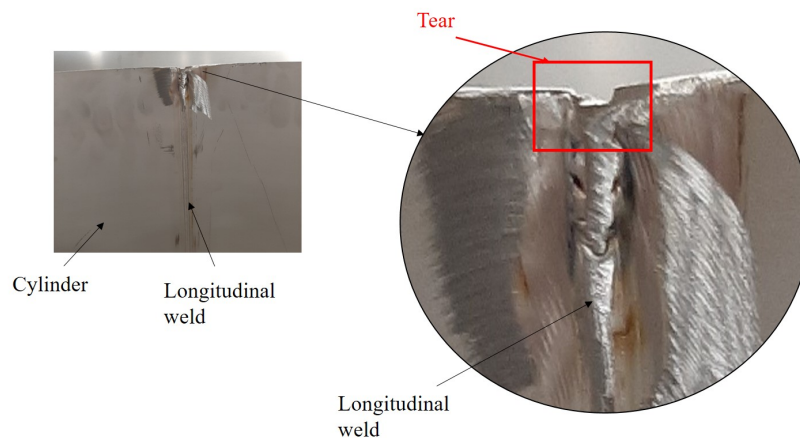


Figure 1.19: Tear of the longitudinal weld.

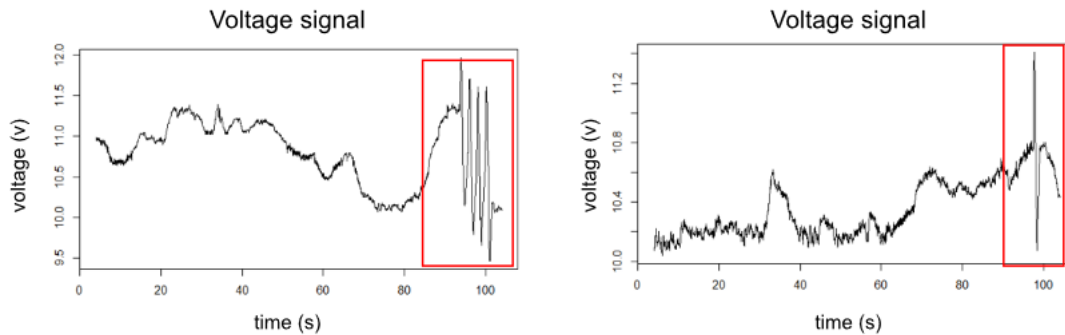


Figure 1.20: Voltage signals where the burn-through is detected at the end of the welding cycle.

here. After investigation, we found that the end of the welding cycle corresponds to the part near the welded muff for those specific hot water tanks. We observed that the welding of this latter induces distortions in the cylinder as we show in Fig. 1.21 which perfectly explains the occurrence of burn-through at this location. As a corrective action after this study, the shape of the cylinder at this location is now corrected before the circular welding.

This study of the burn-through root cause shows that the quality of the circular welding depends highly on the ones of the longitudinal welding and the muff welding. Optimizing the latter would highly reduce the number of burn-through occurrences. This can be done by applying the Design of Experiments to reduce the distortion (Narwadkar et al. (2016)) in order to prevent the misalignment between the cap and the cylinder. Furthermore, it would be beneficial to detect the longitudinal welding defects via their welding signals as an approach to reducing the circular welding defects. To prevent the tears of the longitudinal weld, the run-on and run-off tabs are no longer used after this study, the longitudinal weld is now stopped shortly before the borders of the cylinder and is finished by another machine after the circular welding is performed.

In some cases, we noticed that the signature of the burn-through appears also in the wire speed signal. In Appendix A we study if abnormal movements of the wire caused the defect in these cases using the concepts of signal decomposition and causality analysis (Dragomiretskiy et al. (2013); L. Ma et al. (2018)).

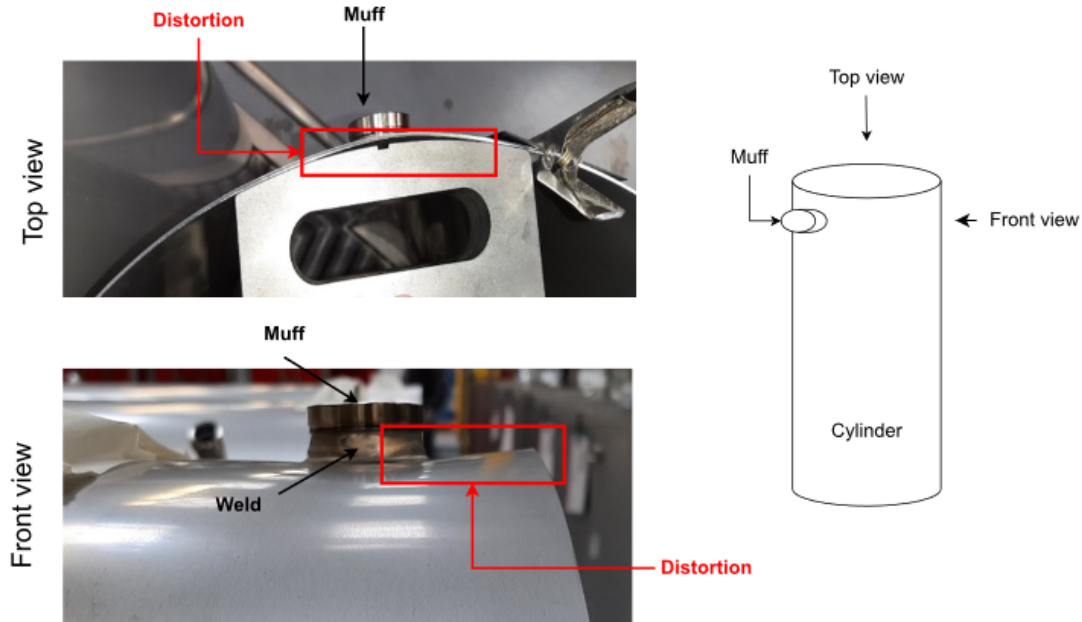


Figure 1.21: The distortion caused by the welding of the muff.

1.6 Conclusion

In this chapter, we reviewed methods used for defect detection from welding signals, and we proposed a two-stage method for burn-through detection in the circular welding process of hot water tanks. Results show that the methodology can classify welding voltage with high accuracy thanks to the information summarized by the probability density distributions and the use of a non-parametric classifier. Moreover, our method can localize defects in the signal with high precision and can be then used in real-time fault detection.

With the help of the presented methodology used to localize the defects, we studied the root cause of the defects by the interpretation of the defect signatures. We then showed the possibility of automatic extraction of the root cause from the signal and demonstrated the feasibility of the burn-through anticipation when it is caused by a misalignment between the cap and the cylinder. Furthermore, we proposed solutions that would allow practitioners to avoid scrap and rework costs.

After this first study about welding signals and the automated detection of burn-through, we were interested in exploring other crucial welding processes and generalizing the automatic defect detection. To that purpose, we carried out efforts to incorporate sensors in these machines. Nevertheless, one disadvantage of the approach proposed in this chapter is that it is supervised, whereas, for the new processes in question, there are much fewer accessible labels and no historical data. Furthermore, the approach only identifies burn-through, whereas we are interested in detecting other welding flaws for which we do not have labeled signals. To address these limitations, we will look at the problem of welding defect detection from another point of view in the next chapter, which is the semi-supervised time series anomaly detection.

Chapter 2

One-class classification for welding fault detection

Contents

2.1	Introduction	44
2.2	Literature review on abnormal time series subsequence detection	47
2.2.1	Methods for anomaly detection in the raw and discrete representations	48
2.2.2	Methods based on features for anomaly detection	52
2.3	Methods and materials	53
2.3.1	Definition and notations	53
2.3.2	Problem Formulation	55
2.3.3	One-Class SVM with distance substitution kernels	56
2.3.4	Time series dissimilarity measures	62
2.3.5	Experimental protocol	65
2.3.6	Evaluation metric	68
2.4	Description of welding processes and preprocessing	69
2.4.1	The circular welding	69
2.4.2	The orbital welding	70
2.4.3	Cold Metal Transfer welding	77
2.5	Results and discussion	82
2.6	Welding defect diagnosis using Random Convolutional Kernel Transform	89
2.7	Conclusion	96

2.1 Introduction

This chapter treats the problem of detecting welding faults using the concept of One-class classification. The need for such semi-supervised welding anomaly identification stems from the fact that normal signals can be easily obtained, while defective weld signals are rare and mostly unlabeled. Moreover, we are interested in detecting anomalies in multiple welding processes with different physiqes. Collecting labels of multiple types of defects for different welding processes would be very time-consuming. Therefore, we are interested here in exploring the possibility of developing a method that can be generalized to different welding processes. Given this formulation of the problem, a suitable method would originate from the field of time series anomaly detection.

Time series anomaly detection is a research subject that gained a lot of interest due to its numerous applications across various fields, such as fault detection in manufacturing, diagnosis in medicine, intrusion detection, and cybersecurity. Many real-world problems focus on finding outliers from time series datasets (Lu et al. (2018)). Anomalies might be hard to define, multiple definitions of the term anomaly (also known as outlier, novelty, and rare event) are suggested in the literature. According to Ord (1996), an anomaly is an observation that is inconsistent with the rest of the data. Chandola, Banerjee, et al. (2009) define an anomaly as a pattern that does not conform to a well-defined notion of normality. Braei et al. (2020) state that anomalies have two main characteristics: the distribution of anomalies deviates significantly from the general data distribution and the majority of the data consist of normal observations.

There are 3 types of time series anomalies depicted in Fig 2.1:

- Point anomaly: a data point whose value is different from the neighboring values (local outlier) or that is different from all values of the time series (global outlier).
- Subsequence anomaly: also known as a collective anomaly, which is defined as consecutive points in time that form an abnormal pattern.
- Whole time series anomaly: an entire time series that differs significantly from usual behavior.

As anomalies are patterns that do not conform to a well-defined normality, the reference of nor-

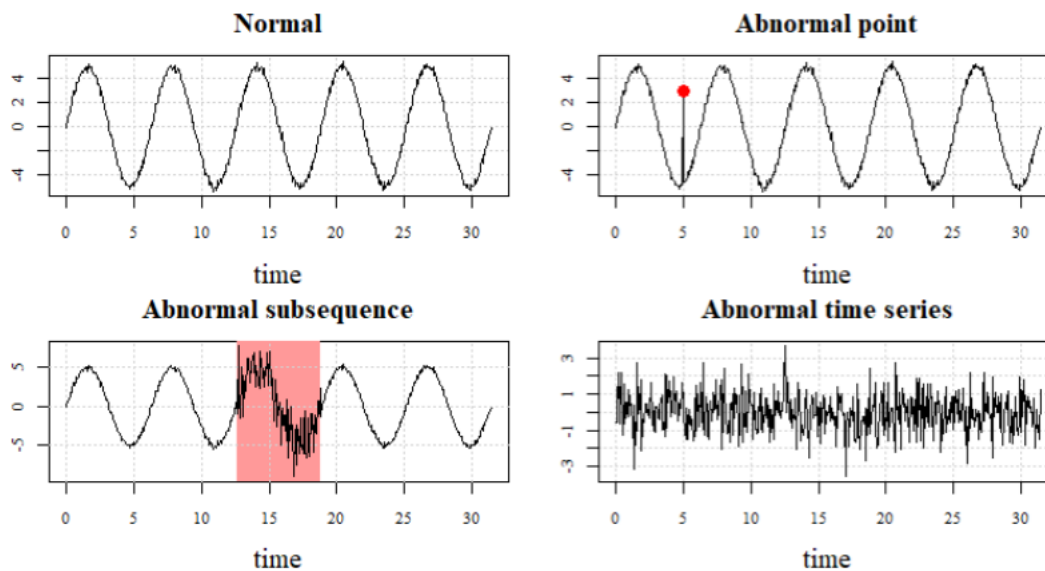


Figure 2.1: Types of univariate time series anomalies.

mality is important in the detection of these types of time series anomalies and helps in the selection of the appropriate methods. For the point anomaly, the reference can be the neighboring values if one is interested in detecting a local outlier (also known as contextual anomaly) or the whole time series values to detect a global point outlier. For abnormal subsequence detection, the references can be the subsequences of the same time series, the previous subsequence, or subsequences of external time series depending on the problem at hand. The references for abnormal whole time series are external time series in the univariate case. In the multivariate case, the references can be the time series of the other variables in the multivariate time series or external multivariate time series.

Most of the methods in the literature focus on the detection of abnormal points in time series (Blazquez-Garcia et al. (2021)). In our case, we are interested in the detection of abnormal subsequences in the univariate case where the variable is the voltage signal. This is due to the fact that a welding defect occurs very often in a small part of the weld seam. The defect is then observed as an abnormal subsequence in the signal. This applies to all the welding processes considered in this chapter. Hence, to be able to detect abnormal subsequences in the voltage signal, we follow the general procedure depicted in Fig. 2.2 in the work of this chapter. When a new voltage signal

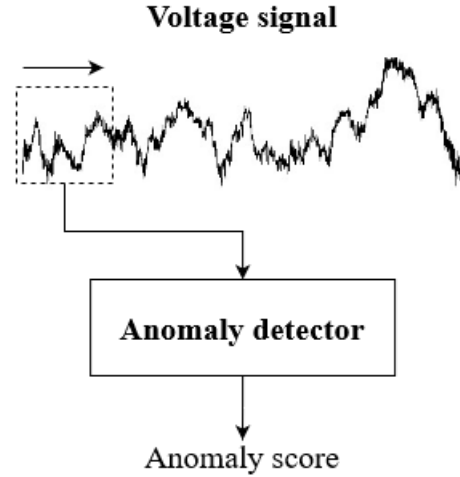


Figure 2.2: The procedure followed for the detection of abnormal subsequences.

arrives, its subsequences are extracted using a moving window, whose size is to be set for each welding process, and passed to an anomaly detector, which outputs an anomaly score for each subsequence that indicates the degree of abnormality after which a threshold is used to transform it into a binary label. Preprocessing or post-processing might be added to this general procedure in order to tackle specific problems. As we shall see later in this chapter, we add a post-processing step for the circular welding process to predict the type of the detected anomaly, while for the other processes, we add a preprocessing to despike the signals.

The following summarizes our work in this chapter:

- We propose a method based on the One-Class Support Vector Machine with distance substitution kernels to detect abnormal times series subsequences for anomaly detection in different welding processes.
- We show that the proposed approach allows working with the raw subsequences while having a lower algorithmic complexity than most of the existing methods dealing with the raw data.
- We propose an automatic diagnosis of the circular welding defects based on a method that treats a specific problem of time series classification.
- We propose techniques for signal despiking.

The chapter is organized as follows: section 2.2 gives a literature review of methods used in abnormal time series subsequence detection. We formulate the problem and present the One-Class SVM and how to adapt it to the problem of anomaly detection from the raw subsequences in section 2.3. In section 2.4 we introduce the three welding processes we are interested in along with signal preprocessing. In section 2.5 we give the results of the anomaly detection in the three considered processes. In section 2.6 we conduct a study to propose an automatic welding defect diagnosis, and we finish the chapter with conclusions and future works.

2.2 Literature review on abnormal time series subsequence detection

In machine learning, methods for anomaly detection can be classified based on the level of supervision, i.e: supervised, semi-supervised, and unsupervised. (Chandola, Banerjee, et al. (2009)).

- *Supervised methods*: these methods assume that the labels for the normal and the anomaly classes are available, which is a challenging requirement in applications such as welding where it is hard to obtain the labels of all the anomaly classes.
- *Semi-supervised*: this class of methods assumes that labels for normal data are available. They build a model that learns the normal behavior. A new instance is accepted if it belongs to the known class, otherwise, it is classified as abnormal.
- *Unsupervised*: the unsupervised methods do not require any knowledge or labels of the data, which is their most notable advantage. They rely on the assumption that the majority of the data is normal, while anomalies are rare and live in low-density regions.

In what follows we will be only interested in semi-supervised and unsupervised methods for anomaly detection since labels for anomaly classes are rarely available in our case study as stated before.

In most mining tasks, three types of representations exist for working with temporal data :

- *Raw data*: working with the raw data has the advantage of avoiding information loss. How-

ever, methods working directly with the original data often suffer from high computational complexity.

- *Discretization*: the continuous time series are transformed here into discrete sequences using methods such as Symbolic Aggregate Approximation (SAX). This representation compresses the original data, thus allowing to speed up the processing, but can cause loss of information.
- *Numeric Multidimensional transformation*: consists in summarizing the temporal data into a multidimensional feature vector. This can be achieved by feature engineering or by automatic feature extraction using neural networks.

We group the approaches used for subsequence anomaly detection into two main categories. The first deal with subsequences in both the raw and the discrete representations, while the second is intended for detecting anomalies after transforming the subsequences into a multidimensional vector.

2.2.1 Methods for anomaly detection in the raw and discrete representations

Discord detection

A famous unsupervised method for abnormal subsequence detection in the literature is called the discord detection proposed by Keogh, Lin, and Fu (2004). It seeks to detect the most unusual subsequence in a time series called the discord, which is defined as the subsequence of length m , fixed by the user, having the highest distance to its nearest neighbor in the time series. The distance used depends on the types of time series and the anomalies to be detected. In most cases, The Euclidean distance is well-suited and provides good detection (Keogh, Lin, and Fu (2004)). The brute force algorithm has $O(m^2)$ complexity, where m is the length of the discord, and is therefore not possible to use for long time series. Keogh, Lin, and Fu (2004) proposed to use a discretization called Symbolic Aggregate ApproXimation (SAX) to reduce the dimensions of the data along with pruning to speed up the computations. Bu et al. (2007) extended the technique to detect top k discords by employing the Haar wavelet transform along with augmented trie. To overcome the

problem of discord length selection, Kha et al. (2015) used a segmentation technique to retrieve variable length candidates and used a homothetic transformation to scale the subsequences to the same length. After that, clustering is performed on the transformed subsequences, and the Cluster-Based Local Factor (CBLOF) algorithm is used to detect K top discords. A shortcoming of these techniques is that, since discord detection is fully unsupervised, it does not rely on the use of a threshold or known normality references, it then requires user intervention to decide whether a discord is an anomaly.

Clustering

The clustering techniques can be extended to perform anomaly detection. The main idea is that observations that do not belong to any cluster are considered abnormal. Generally, if the distance d of a subsequence s to its closest centroid \hat{s} is greater than threshold τ , i.e: $d(s, \hat{s}) > \tau$, s is considered abnormal. In this kind of dissimilarity-based approach, the distance d should be chosen depending on the problem and the nature of the data. Chao Chen et al. (2011) transformed time series into discrete representation and uses the K-means algorithm with the Euclidean distance to cluster the normal patterns. They then use the general rule discussed above to detect abnormal patterns. Boniol et al. (2020) proposed a method that consists of summarizing the subsequences of a time series by only one subsequence that best captures the normal behavior. This is done by clustering the subsequences and choosing the centroid of the cluster that represents the normality, depending on the criteria of frequency and coverage. The abnormal subsequences are then detected based on the distance between them and the normal subsequence.

There are some issues with the clustering methods; the choice of the number of clusters may be difficult, and they consider the clusters to be spherical (Bigdeli et al. (2017)). Furthermore, it was shown that clustering overlapping subsequences is meaningless and always produces sinusoidal centroids independently of the dataset and the clustering algorithm (Keogh and Lin (2005)).

Nearest neighbors

An important number of anomaly detection methods are based on the k Nearest Neighbors (k -NN) algorithm and its variants (Munir et al. (2018)). Since anomalies are in low-density regions, the assumption is that the distances of abnormal observations to their k nearest neighbors are significantly higher compared to those of normal observations to their k Nearest neighbors. L. Lei et al. (2023) used the Local Outlier Factor (LOF) with the Dynamic Time Warping (DTW) dissimilarity in order to detect abnormal subsequences in energy consumption time series. Ishimtsev et al. (2017) used the average of the distances of the subsequence of interest s to its k nearest neighbors as the anomaly score. Chandola, Cheboli, et al. (2009) used k -NN and considers the distance of subsequence of interest s to its k^{th} neighbor in the set of subsequences S as the anomaly score. Teng (2010) proposed a k -NN approach with the DTW. The authors attempted to reduce the computational complexity by using a lower bound of the distance and by reducing the number of training instances by averaging similar ones.

Despite their simplicity and straightforward implementation, these methods suffer from high computational complexity, since they require to compute the distances between a subsequence of interest s and every subsequence in the dataset.

Forecasting

These methods are based on fitting a forecasting model to the training data and the use of the forecasting error as the anomaly score. The assumption is that large forecasting errors indicate abnormal points. Classical statistical forecasting methods were used in several works. Pincombe (2005) used Autoregressive Moving Average (ARMA) model to detect anomalies in time series of graphs. To deal with nonstationarity, some works adopt Autoregressive Integrated Moving Average (ARIMA) for the time series modeling, as in the works by Zhu et al. (2011) and Moayedi et al. (2008). To account for the seasonal component in the time series, Kromkowski et al. (2019) used the Seasonal ARIMA (SARIMA) for network traffic anomaly detection. Other works employ regression techniques to model the data. One of the most used approaches is the Support Vector Regression that was used by Kromanis et al. (2013) and Y. Yang et al. (2021). Recent works leverage deep

learning for forecasting and anomaly detection. For instance, Malhotra et al. (2015) employed a Long Short Time Memory (LSTM) neural network to learn the normal dynamics of the time series. Chauhan et al. (2015) used a deep LSTM network to learn the normal Electrocardiogram signals and fit a Gaussian Mixture Model to the residuals for the final anomaly score. Munir et al. (2018) proposed a predictor based on a convolutional neural network and considered the points for which the error is higher than a preset threshold as anomalies.

Reconstruction

Similar to forecasting-based methods, these methods consider reconstruction errors as anomaly scores. Most of the techniques are based on autoencoders. Theumer et al. (2021) proposed an autoencoder composed of gated recurrent units to detect both abnormal points and subsequences. T. Chen et al. (2020) used a variational autoencoder based on two-dimensional convolutions to detect abnormal subsequences in multivariate time series. J. Chen et al. (2020) used a stacked denoising autoencoder to reconstruct the time series from corrupted versions using multiple noise levels. Choi et al. (2022) proposed a model to detect anomalies in multivariate time series named SeqVAE-CNN, which is a variational autoencoder where the encoder is composed of one convolutional layer followed by one LSTM layer.

Information theory

This class of methods uses the information carried by the subsequences to detect anomalies. They rely on measures of information such as entropy, conditional entropy, and information gain to detect infrequent observations after discretizing the data. J. Yang et al. (2004) uses the information gain to detect abnormal periodic patterns. Bereziński et al. (2015) investigated the use of Shannon, Renyi, and Tsallis entropy for network anomaly detection.

2.2.2 Methods based on features for anomaly detection

In order to reduce the dimensionality of the data and reduce noise, a large body of research proposes to work with a multidimensional transformation of the subsequences by feature extraction. In this case, any method intended for anomaly detection in tabular data can be employed. There are two types of feature extraction for time series: engineered features and deep features.

Engineered features

Engineered features are meaningful characteristics of the time series subsequences that are hand-crafted prior to the use of an anomaly detector. They can be extracted from the time domain, the frequency domain, or the time-frequency domain. Hu et al. (2018) proposed a method based on the extraction of 6 statistics and the use of the One-Class SVM (OC-SVM). When a new subsequence arrives, its 6 statistics are extracted, and then the OC-SVM predicts whether they belong to the learned normal regions. N. Huang et al. (2015) used wavelet transform to extract time-frequency features and used OC-SVM to detect mechanical faults of high voltage circuit breakers. Xu et al. (2019) extracted features from both time and frequency domains for the detection of vibration signal anomalies. H. Wang et al. (2022) extracted 15 statistical characteristics from the vibration signal of rolling-element bearing and used the Isolation Forest algorithm to detect defects.

The challenge with this form of feature extraction is that designing the proper features may necessitate a high level of human knowledge (Janssens et al. (2016)). Moreover, as the extracted features depend on the problem at hand, the same features might not be efficient for different problems where time series and anomalies are of different natures. Furthermore, this transformation of subsequences into tabular data may cause loss of information (Teng (2010)).

Deep features

Instead of manually designing the appropriate features, some works make use of deep neural networks for automatic feature extraction. They are known in the literature as deep features. Zilong Wang et al. (2021) used an autoencoder to extract features from the latent space and employed

OC-SVM to detect abnormal time series. Some other works as in C. Liu et al. (2021) replace the kernel function of the Support Vector Data Description (SVDD), which is an alternative formulation of the OC-SVM, by a convolutional neural network. In this setting, the loss functions of the SVDD and the reconstruction loss function of the autoencoder are simultaneously optimized, which forces the features learned by the autoencoder to be in a minimum volume hypersphere.

2.3 Methods and materials

The above literature review shows that there are a plethora of methods proposed for time series anomaly detection. In several recent benchmarks, it was shown that classical statistical and machine learning methods can outperform deep learning for time series anomaly detection (Braei et al. (2020); Wu et al. (2021); Schmidl et al. (2022)). Particularly, dissimilarity-based techniques dealing with the raw data are effective for the problem of anomaly detection (H. Ren et al. (2018); Z. Lei et al. (2020)). Furthermore, they can be easily generalized to diverse problems. In our case, this would allow us to generalize anomaly detection for different welding processes. However, they often suffer from high computational complexity, which could limit their use, especially with the need for real-time predictions in an industrial environment. In this context, we present our contribution, which is the use of the OC-SVM for the detection of abnormal time series subsequences. The use of OC-SVM is advantageous because it only requires distances to the support vectors for the inference, unlike most of the distance-based methods that require distances to all normality references. Moreover, unlike clustering techniques, the OC-SVM can adapt to any cluster shape. However, an issue is that the OC-SVM is designed for vector data and not temporal data. To address this issue, our contribution consists in integrating a dissimilarity measure in the formulation of the OC-SVM using distance substitution kernels.

2.3.1 Definition and notations

- **Time series:** A time series x_t is a sequence of real values ordered in time, where $t \in [1, 2, \dots, n]$ with n is the length of the time series.

- **Time series subsequence:** Given a time series x_t with $t \in [1, 2, \dots, n]$, a subsequence s of x_t is a segment of length m with $m \ll n$, starting at the index p and ending at $p + m - 1$. i.e : $s^p = x_p, \dots, x_{p+m-1}$ with $1 \leq p \leq n - m - 1$
- **Dissimilarity :** Given two subsequences s and s' of length m and n respectively, a dissimilarity measure is a mapping $d(s, s') : \mathbb{R}^m \times \mathbb{R}^n \rightarrow \mathbb{R}^+$ that indicates the proximity between s and s' . The higher the value of d the more distant are the subsequences s and s' .

There are two types of dissimilarity measures in the time series domain, lock-step and elastic measures illustrated in Fig. 2.3). The lock-step dissimilarity measures are defined only when $n = m$ and compare the i^{th} point of s to the i^{th} point of s' whereas elastic dissimilarity measures can work with subsequences of different lengths and also allow alignment of the subsequences by performing nonlinear mappings.

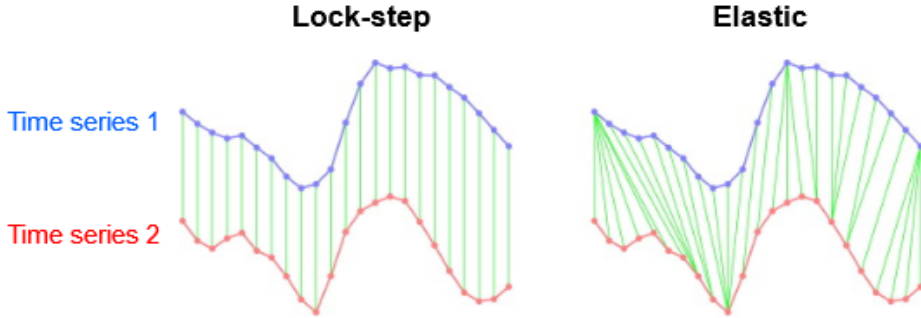


Figure 2.3: Illustration of lockstep and elastic dissimilarity measures.

- **Anomaly detector:** An anomaly detector for a univariate subsequence s of length m is a mapping $A : \mathbb{R}^m \rightarrow \mathbb{R}$, $A(s) = \gamma$ Where $\gamma \in \mathbb{R}$ is the anomaly score, which reflects the degree of abnormality of s . Generally, the higher the score, the more s is abnormal.

In order to convert the anomaly scores into binary labels, a mapping A_{binary} is performed by applying a threshold $\tau \in \mathbb{R}$ to the anomaly score γ . An observation whose anomaly score is higher than τ is assigned the label *abnormal*.

$$A_{binary} = \mathbb{R} \rightarrow \{normal, abnormal\}$$

$$\begin{cases} \text{Abnormal,} & \text{if } A(s) > \tau \\ \text{Normal,} & \text{Otherwise} \end{cases}$$

- **Centering:** Centering a subsequence s is a transformation such that the mean of the subsequence is equal to 0. i.e: $s_c = s - \bar{s}$. Where \bar{s} is the mean of the subsequence.
- **Z-normalization:** Z-normalization of a subsequence s is a transformation such that s has a mean of 0 and a unit standard deviation, i.e. $s_z = \frac{s - \bar{s}}{\sigma_s}$, where σ_s is the standard deviation of the subsequence s .

2.3.2 Problem Formulation

Given a time series x_t of real values ordered in time with $t \in [1, 2, ..n]$ where n is the length of the time series, we seek to detect abnormal subsequences of a fixed length $m \ll n$ by analyzing them using a model trained to recognize the normal behavior.

For this purpose, the set S of all possible subsequences $s^p = x_p, \dots, x_{p+m-1}$ of length m with $1 \leq p \leq n - m - 1$ are extracted from x_t with a moving window of length m and step 1. Depending on the problem at hand, z-normalization or centering might be needed. The former is used when one is interested in detecting subsequences with abnormal shapes, while the latter is used when the abnormal subsequences are characterized by their abnormal amplitude. The extracted subsequences are analyzed by the normality model, which is trained on a set \hat{S} composed only of normal subsequences, also of length m , extracted from normal time series. The model produces an anomaly score $A(s^p)$ for each $s^p \in S$, which is then transformed to a binary label using A_{binary} .

In the next section, we show how to obtain the normality model using OC-SVM directly from the raw subsequences.

2.3.3 One-Class SVM with distance substitution kernels

In many applications, it is preferable to rely on an external reference of normality in order to detect abnormal subsequences in an incoming time series, which is the case for our case study where the reference of normality is subsequences of voltage signals of defect-free welding. Learning the normal class of subsequences can be done with a one-class classification algorithm, such as the One-Class SVM (OC-SVM). OC-SVM learns the boundaries of the hypersurface enclosing the normal data class and rejects any instance that does not belong to it. More formally, the method seeks to find the support of a high-dimensional data distribution.

We use here the OC-SVM proposed by (Scholkopf et al. (2000)) formulated by the following quadratic optimization problem:

$$\min \frac{1}{2} \|w\|^2 - \rho + \frac{1}{\nu N} \sum_{i=1}^N \xi_i \quad (2.1)$$

$$\begin{aligned} s.c : \langle w, x_i \rangle &\geq \rho - \xi_i \\ \xi_i &\geq 0 \end{aligned} \quad (2.2)$$

With :

- w : the vector normal to the hyperplane.
- ρ : the distance between the origin and the hyperplane.
- $\nu \in]0; 1]$: the proportion of outliers in the training data.
- ξ : slack variables used to account for outliers.
- N : the number of the training data.

The OC-SVM (Fig. 2.4 (a)) seeks to find a hyperplane that maximizes the distance ρ between the origin of the space and the normal training data. It is a soft-margin problem controlled by the proportion of outliers in the training data ν which is both an upper bound on the proportion of

outliers and a lower bound on the proportion of support vectors.

In order for the OC-SVM to be able to learn nonlinear decision boundaries (Fig. 2.4 (b)), a nonlinear kernel k is used in the dual problem. The dual problem is obtained by introducing the Lagrangian multipliers $\alpha_i > 0$ and $\eta_i > 0$ as follows:

$$L(w, \xi, \rho) = \frac{1}{2} \|w\|^2 - \rho + \frac{1}{\nu N} \sum_{i=1}^N \xi_i + \sum_{i=1}^N \alpha_i (\rho - \xi_i - \langle w, x_i \rangle) - \sum_{i=1}^N \eta_i \xi_i \quad (2.3)$$

For optimality, the partial derivatives of L must be computed with respect to w , ξ , and ρ and set to 0. They are given as:

$$\frac{\partial L}{\partial w} = 0 \implies w = \sum_{i=1}^N \alpha_i x_i \quad (2.4)$$

$$\frac{\partial L}{\partial \xi_i} = 0 \implies \frac{1}{\nu N} = \alpha_i + \eta_i \quad (2.5)$$

$$\frac{\partial L}{\partial \rho} = 0 \implies \sum_{i=1}^N \alpha_i = 1 \quad (2.6)$$

By substituting these equations in Eq. 2.3, we obtain the dual problem given as follows:

$$\min \sum_{i=1}^N \sum_{j=1}^N \alpha_i \alpha_j x_i x_j \quad (2.7)$$

$$\begin{aligned} \text{s.t. } & 0 \leq \alpha_i \leq \frac{1}{\nu N} \\ & \sum_i \alpha_i = 1 \end{aligned} \quad (2.8)$$

Since the dual problem involves the inner product, a nonlinear kernel k can be used to compute the similarities in a feature space A to which the data x could be mapped from the original space X by $\phi: X \rightarrow A, x \rightarrow \phi(x)$ without going through the mapping ϕ , i.e: $k(x_i, x_j) = \phi(x_i)\phi(x_j)$. Hence, the kernelized dual problem is then given by:

$$\min \sum_{i=1}^N \sum_{j=1}^N \alpha_i \alpha_j k(x_i, x_j) \quad (2.9)$$

$$\begin{aligned} s.t : 0 \leq \alpha_i \leq \frac{1}{\nu N} \\ \sum_i^N \alpha_i = 1 \end{aligned} \tag{2.10}$$

which allows learning a nonlinear decision function.

To detect if an instance x' is normal, the OC-SVM uses a decision function that determines whether the instance belongs to the learned hypersurface or to its complement. It is defined as follows:

$$F(x') = \left(\sum_i^N \alpha_i k(x', x_i) - \rho \right) \tag{2.11}$$

The prediction is made as follows:

$$\begin{cases} \text{Normal,} & \text{if } F(x') > 0 \\ \text{Abnormal,} & \text{Otherwise} \end{cases}$$

If the sign of $F(x')$ is positive, x is in the normal region, otherwise, it is outside this region and is then abnormal. The anomaly score is the value of the decision function $F(x')$, the smaller the value, the more anomalous the instance. The decision function in Eq. 2.11 is calculated using only the support vectors i.e. the training instances x_i with $0 \leq \alpha_i \leq \frac{1}{\nu N}$, which makes the prediction fast comparing to other methods that require distances to all training data. Moreover, the proportion of support vectors in the training data $\frac{N_{sv}}{N}$, where N_{sv} is the number of the support vectors, is an estimator of the classification error of the normal class. These statistical guarantees associated with the OC-SVM make it more attractive than other approaches.

The OC-SVM is formulated originally for vector data. Therefore, it has not been widely explored for direct learning from ordered sequences such as time series subsequences. Previous works using OC-SVM transform the time series into vector data by performing feature extraction. J. Ma et al. (2003) stated that one needs to find a method to convert the time series to vectors in order to be able to use OC-SVM. The works following this strategy are numerous as we saw in the literature such as in Su et al. (2015), Hu et al. (2018), and Zilong Wang et al. (2021). Beggel et al. (2019) stated that OC-SVM is applicable to time series only after extracting some features from them.

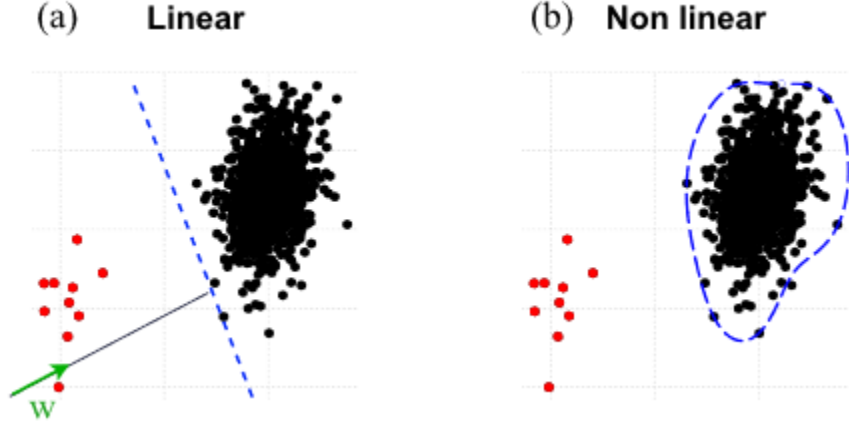


Figure 2.4: Illustration of OC-SVM with the linear (a) and nonlinear (b) kernels.

Braei et al. (2020) highlighted in their review on time-series anomaly detection that previous works stated that the OC-SVM is able to detect anomalies only in a set of vectors and not on time series.

However, to be able to use the OC-SVM with temporal data, in fact, one must find a way to incorporate a dissimilarity measure in the kernel rather than necessarily transforming the data into a set of vectors. The work in Schölkopf (2000) demonstrated the existence of a class of kernels that allows the integration of a dissimilarity measure and transforms kernel methods into dissimilarity-based methods, which were introduced to treat the problem of computing distances in the feature space. These kernels are known as Distance Substitution (DS) kernels, which we propose to use in the OC-SVM to be able to learn the normal class directly from the raw subsequences, which is the novelty of our work. In time series classification, these kernels have been used in some works with multi-class SVM as in Bahlmann et al. (2002) and D. Zhang et al. (2010). However, they have not gained widespread adoption for abnormal time series subsequence detection with the One-class SVM, despite the discussed advantages that the OC-SVM can offer.

We propose in this study the use of the Radial Basis (RBF) and the Negative Distance (ND) DS kernels, which are defined as follows:

- $k_{RBF}(x, x') = e^{-\gamma d(x, x')}$
- $k_{ND}(x, x') = -d(x, x')^\beta$

where γ and β are smoothing parameters that control the degree of the non-linearity of the decision boundaries. For $\beta = 2$, the ND kernel produces a perfectly spherical decision boundary in the OC-SVM. To ensure that the optimization problem is convex, the dissimilarity d used must be a metric (for the kernel to be positive definite and therefore a valid Mercer kernel), i.e. it must satisfy the following conditions:

- Symmetry: $d(x, x') = d(x', x)$
- Separation $d(x, y) = 0 \implies x = y$
- Positivity: $d(x, y) > 0$
- The triangular inequality: $\forall x, y, z, d(x, y) \leq d(x, z) + d(z, y)$

The RBF DS kernel is positive definite for any metric and the ND kernel is conditional positive definite for $\beta \in]0, 2]$, which is a valid kernel for translation invariant problems (Schölkopf (2000)). This ensures the existence of a space A in which the similarities are computed with the kernel trick without going through the projection: $K(x, x') = \langle \phi(x), \phi(x') \rangle$.

The new formulation of OC-SVM that we propose in order to work with time series subsequences is given in Eq.2.12:

$$\min \sum_{i=1}^N \sum_{j=1}^N \alpha_i \alpha_j DSk(\hat{s}^i, \hat{s}^j) \tag{2.12}$$

$$\begin{aligned} s.t : 0 \leq \alpha_i \leq \frac{1}{\nu N} \\ \sum_i^N \alpha_i = 1 \end{aligned} \tag{2.13}$$

Where DSk is a DS kernel employing a dissimilarity d , N is the number of the training subsequences \hat{S} , and \hat{s}^i and \hat{s}^j are two training subsequences in \hat{S} .

A pseudocode for training the OC-SVM with a DS kernel is given in Algorithm 1. In this stage, the dissimilarity matrix of the training subsequences is computed and transformed into a kernel

matrix using a DS kernel. This matrix is then used to fit an OC-SVM model with the predefined parameter ν . In the test stage detailed by Algorithm 2, the test dissimilarity matrix is obtained by computing the dissimilarities between the test subsequences and the support subsequences of the trained model. The model uses then this information to compute the anomaly scores by Eq. 2.11.

For the detection of abnormal subsequences, the Euclidean distance is the most used. However, some problems require the use of elastic measures, which are mostly non-metric. In the multi-class SVM, results of the works by Bahlmann et al. (2002) and D. Zhang et al. (2010) show that the Dynamic Time Warping, which is theoretically non-metric dissimilarity, can still produce a good

Algorithm 1 Train OC-SVM with DS kernel

```

1:  $\hat{S}$                                 ▷ Subsequences of some normal time series
2:  $\gamma$                                 ▷ kernel parameter
3:  $\nu$                                   ▷ proportions of outliers
4:  $D$                                   ▷ Dissimilarity matrix of normal subsequences
5:  $KM$                                   ▷ Kernel Matrix
6: for (i =1 to  $|\hat{S}|$ ) do
7:   for (j =1 to  $|\hat{S}|$ ) do
8:      $D[i, j] \leftarrow d(\hat{S}^i, \hat{S}^j)$ 
9:   end for
10: end for
11:  $KM \leftarrow k(D)$                   ▷  $k$  is the kernel. For example  $k = \exp(-\gamma D)$  for the RBF kernel.
12:  $model \leftarrow solve\_ocsvm(KM, \nu)$   ▷ Fit the OC-SVM model

```

Algorithm 2 Predictions with OC-SVM using DS kernel

```

1:  $x_t$                                 ▷ The test time series
2:  $SV$                                 ▷ The support vectors of the trained model (support subsequences in our case).
3:  $w$                                   ▷ Length of the subsequences
4:  $D\_test$   ▷ Dissimilarity matrix between the test subsequences and the support vectors of the
   trained model.
5:  $\tau$                                   ▷ Threshold of the anomaly scores.
    $S = \text{get\_subsequences}(x_t, w)$   ▷ Subsequences of the test time series
6: for (i =1 to  $|S|$ ) do
7:   for (j =1 to  $|SV|$ ) do
8:      $D\_test[i, j] \leftarrow d(S^i, SV^j)$ 
9:   end for
10:  $KM\_test = k(D\_test)$                 ▷ Kernel Matrix
11:  $Anomaly\_scores \leftarrow model.predict(KM\_test)$ 
12:  $Final\_predictions \leftarrow convert\_to\_binary(Anomaly\_scores, \tau)$   ▷ 0 if
    $Anomaly\_scores[i] > \tau$ , 1 otherwise.

```

classification accuracy when used in DS kernels. We also investigate in our experiments the use of an elastic dissimilarity measure with the DS kernels in OC-SVM and study its accuracy.

2.3.4 Time series dissimilarity measures

We consider in this work two dissimilarity measures. The Euclidean distance, also known as L_2 distance, defined for two sequences $x = (x_1, x_2, \dots, x_m)$ and $y = (y_1, y_2, \dots, y_m)$ as follows:

$$ED(x, y) = \left(\sum_{i=1}^m |x_i - y_i|^2 \right)^{\frac{1}{2}} \quad (2.14)$$

and a lower bound of the Dynamic time warping (DTW) in order to deal with phase shifts between the signals of some welding processes. To obtain DTW distance between two sequences $x = (x_1, x_2, \dots, x_m)$ and $y = (y_1, y_2, \dots, y_n)$ of length m and n respectively, the algorithm begins by constructing the cost matrix $M \in R^{m \times n}$ of all pairwise distances, where each element $M_{i,j}$ is generally the L_2 distance between x_i and y_j . The warping path P (also called the alignment path) is a sequence of points $P = (p_1, p_2, \dots, p_k)$ with $p_l = (p_i, p_j)$ for $l \in [1 : K]$, where K is the length of the warping path. The warping path must satisfy three conditions (Senin (2008); Keogh and Ratanamahatana (2005)):

- **Boundary conditions:** $p_1 = (1, 1)$, $p_K = (m, n)$. This means that the warping path must start at the first points of the aligned sequences and end at their last points.
- **Continuity:** Given $p_l(a, b)$ then $p_{l-1}(a', b')$ where $a - a' \leq 1$ and $b - b' \leq 1$. This restricts steps to adjacent cells.
- **Monotonicity** Given $p_l(a, b)$ then $p_{l-1}(a', b')$ where $a - a' \geq 0$ and $b - b' \geq 0$ which preserves the time-ordering of points.

The optimal warping path P^* that gives the best alignment between x and y is the one that minimizes the dissimilarity, i.e: $DTW(x, y) = \min_P (\sum_{l=1}^K M_{P_l}/K)$ obtained by dynamic programming.

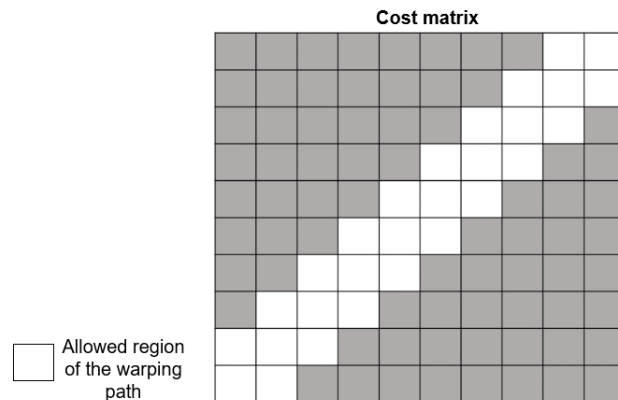


Figure 2.5: An illustration of a Sakoe-Chiba constraint. The white cells indicate the allowed shifts from the diagonal.

The time complexity for the DTW computation is $O(mn)$. However, we can reduce this complexity using a constraint on the warping window such as the Sakoe-Chiba constraint that limits the warping path to be inside a region that determines the largest temporal shift allowed from the diagonal of the matrix M i.e: $w_t = (i, j)_t$ such that $j - r \leq i \leq j + r$, where r is a positive integer (Keogh and Ratanamahatana (2005)), as illustrated by Fig. 2.5. Moreover, since we are dealing with subsequences of the same length as formulated earlier, there exist techniques for computing lower bounds of DTW in much lower time complexity. Keogh and Ratanamahatana (2005) proposed a lower bound named *lb_keogh* that is defined for same length sequences. To compute the $lb_keogh(x, y)$ between x and y of the same length n , the technique starts by creating an upper and a lower envelope U and L of x defined as:

- $U_i = \max(x_{i-r}, x_{i+r})$
- $L_i = \min(x_{i-r}, x_{i+r})$

Where r is a positive integer corresponding to the window constraint. For the Sakoe-Chiba

constraint, r is independent of i . The lower bound is then obtained by the following formula:

$$lb_keogh(x, y) = \begin{cases} d(y_i, U_i) & \text{if } y_i > U_i \\ d(y_i, L_i) & \text{if } y_i < L_i \\ 0 & \text{Otherwise} \end{cases} \quad (2.15)$$

where d here is the Euclidean distance. An illustration of the lb_keogh is given in Fig. 2.6.

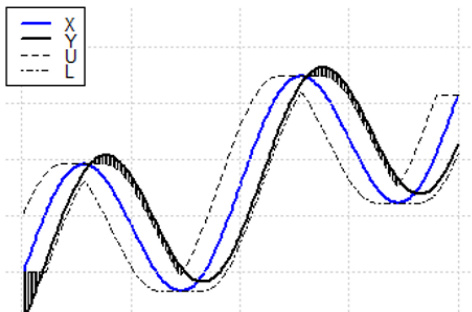


Figure 2.6: Illustration of the lb_keogh . The hatched region is the lower bound.

Another technique that gives a tighter lower bound is proposed by Lemire (2009) and is known as $lb_improved$. It is based on two passes of lb_keogh as follows:

$$lb_improved(x, y) = lb_keogh(x, y) + lb_keogh(y, x') \quad (2.16)$$

Where x' is the projection of x on the envelopes of y and is defined as:

$$x'_i = \begin{cases} U(y)_i & \text{if } x_i \geq U(y)_i \\ L(y)_i & \text{if } x_i \leq L(y)_i \\ x_i & \text{Otherwise} \end{cases} \quad (2.17)$$

In the present study, we consider the $lb_improved$ since it gives a better lower bound of the DTW dissimilarity.

2.3.5 Experimental protocol

Fig. 2.7 shows the steps of the experimental protocol followed in our work. In the training stage, we fit an OC-SVM model with a DS kernel employing an adequate dissimilarity measure. We use the L_2 distance when dealing with the signals of the circular welding, while for the rest of the welding processes considered in this study, we use the *lb_improved* to account for the phase shifts. We use the Sakoe-Chiba constraint with a width r that we fix to at least the length of one period of the signal. Note that since the *lb_improved* might not be symmetric, we compute the distance from the test subsequence to the support subsequences in Eq. 2.11 i.e $F(s) = (\sum_i^N \alpha_i DSk(s, \hat{s}^i) - \rho)$, where s is the test subsequence, in order to get the anomaly score.

Only normal data is used for training since we are dealing with a semi-supervised problem. The training subsequences are extracted from voltage signals with a non-overlapping moving window. This is because we want the subsequences to be different in order to capture more variations of the normal behavior. Furthermore, if the subsequences are overlapping, they are then embedded in the phase space. This would create a complex representation, which would make it difficult to learn the boundary of the normal class by the OC-SVM. Moreover, the model would require a large number of support vectors to describe the boundary, which results in higher inference time. To

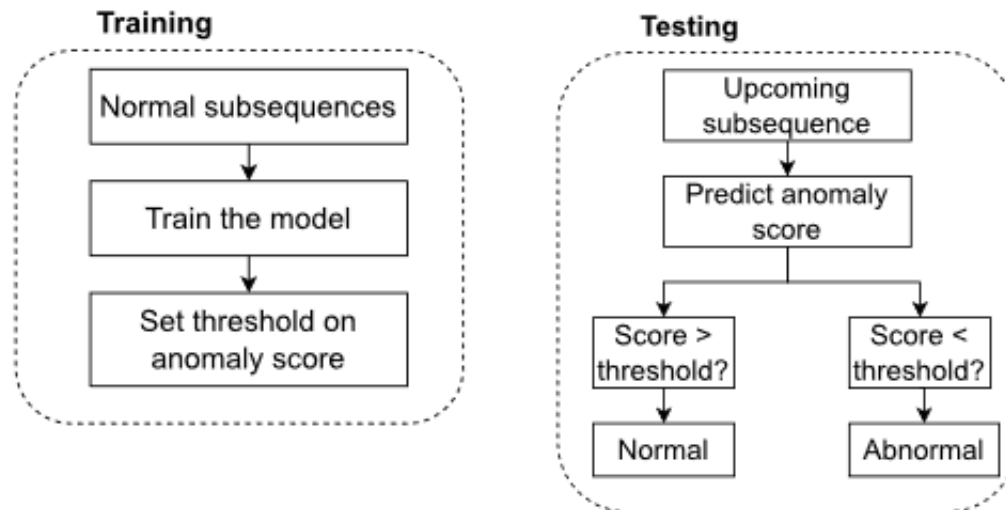


Figure 2.7: The experimental protocol.

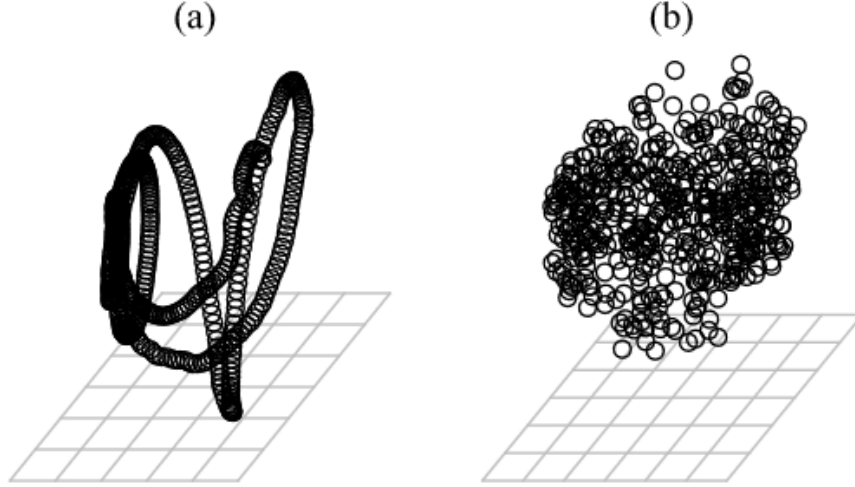


Figure 2.8: The representation of the subsequences obtained by the MDS. (a) overlapping subsequences, (b) non-overlapping subsequences.

show this, we employed Classical Multidimensional Scaling (MDS) to produce a visualization of the subsequences of a voltage signal acquired during the circular welding using the distance matrix for the two cases. Fig. 2.8 (a) shows the representation of overlapping subsequences. As stated above, we notice that they form a complex shape whereas non-overlapping subsequences form a simpler cluster shape as shown in Fig. 2.8 (b). Thus, in all the problems in this work, the training dataset consists of non-overlapping subsequences.

We employ both the *RBF* and the *ND* kernels. The γ parameter of the former will be fixed at $\frac{1}{m}$ where m is the length of the subsequences, following the well-known heuristic $\frac{1}{\text{number of features}}$ used in the classical SVMs. We are not aware of the existence of a method for the choice of the β parameter of the *ND* kernel. Nonetheless, because the training subsequences do not overlap, we expect to obtain a cluster that is nearly spherical as indicated by the visualization in Fig. 2.8 (b) produced by the MDS technique. Consequently, we will set the value of β to 2. The ν parameter is kept at 10^{-5} while the threshold τ on anomaly score of the OC-SVM model is estimated as follows:

$$\tau = \bar{F}(\hat{S}) - 3 \times \sigma_{F(\hat{S})} \quad (2.18)$$

Where $\bar{F}(\hat{S})$ is the mean of the anomaly scores obtained for the training subsequences and $\sigma_{F(\hat{S})}$ refers to their standard deviation. At the test stage, we predict the anomaly score of the new subsequences using the trained model. If it is lower than τ , the subsequence is declared abnormal.

We compare our approach to four other approaches:

1. **Mean k -NN:** this first approach is similar to the one proposed by Ishimtsev et al. (2017) where the mean of the distances to the k nearest neighbors is the anomaly score: $M_NN(s, k, \hat{S}) = \frac{1}{|N_k(s)|} \sum_{\hat{s} \in N_k(s)} d(s, \hat{s})$. where $N_k(s)$ are the k -nearest neighbors of the test subsequence s in \hat{S} and d the dissimilarity measure. We fix the value of k is fixed to 5.
2. **k^{th} -NN:** in the second method, the anomaly score is the distance to the k^{th} nearest neighbors, as in Chandola, Cheboli, et al. (2009). The value of k is fixed to 1 in this approach. We use the same dissimilarity d for the OC-SVM and the k -NN-based methods in each problem.
3. **Feature-based:** this third approach consists of extracting statistical features from the subsequences and the use of an Isolation Forest similar to H. Wang et al. (2022). We extract 8 features that we design based on our knowledge of the welding signals and the anomalies, namely we extract kurtosis, skewness, maximum level shift, maximum variance shift, and other frequency and decomposition statistics.
4. **Autoencoder:** The last approach is based on an autoencoder, where the encoder is composed of two convolutional layers with 32 and 16 filters respectively and a kernel size of 3. In order to optimize the autoencoder by preventing it from overfitting the relatively small training sample, we employ a dropout rate of 0.2 as a regularization. The decoder is composed of two transpose convolution layers with the same number of filters and kernel size. We train the autoencoder with 50 epochs and a batch size of 4.

The threshold for all these approaches is estimated in the same manner as in Eq. 2.18 while adapting the sign of the 3 standard deviations depending on the method.

For a reliable assessment of the approaches, we use the k-folds technique with $k=5$; we decompose the normal dataset into 5 subsets. For each of the 5 iterations, the models are trained using 4 subsets of the normal data while the remaining set is combined with some abnormal subsequences to form



Figure 2.9: Illustration of the 5-folds evaluation technique.

the test dataset as shown in Fig. 2.9. We evaluate the approaches using the F1-score that we present in the next subsection.

2.3.6 Evaluation metric

To obtain a binary classification from an anomaly detector, a threshold must be set on the anomaly score, as seen before. Once done, we evaluate the models based on the F1-score that is computed based on the precision and the recall, which are derived from the confusion matrix illustrated in Table 2.1.

Table 2.1: The confusion matrix.

	Actual anomaly	Actual normal
Predicted anomaly	<i>True positives (TP)</i>	<i>False Positives (FP)</i>
Predicted normal	<i>False Negatives (FN)</i>	<i>True Negatives (TN)</i>

- Precision: The proportion of identified anomalies that are actual anomalies, given by Eq. 2.19.

$$Precision = \frac{TP}{TP + FP} \quad (2.19)$$

- Recall: The proportion of true anomalies in the predicted anomalies. The recall is given by Eq. 2.20

$$Recall = \frac{TP}{TP + FN} \quad (2.20)$$

- F1-score: gives the overall performance by computing the harmonic mean of the precision and recall, it is computed by Eq 2.21.

$$F1\text{-score} = \frac{2 \times Precision \times Recall}{Precision + Recall} \quad (2.21)$$

2.4 Description of welding processes and preprocessing

2.4.1 The circular welding

The first welding process we consider in this study is the circular welding, which was discussed in Chapter 1. We briefly recall here the process and the characteristic of the signal and the anomalies. This welding is carried out by a semi-automatic machine employing Gas Tungsten Arc Welding (GTAW), which simultaneously performs the welding of the two caps of the hot water tank. During the circular welding process, the tank rotates at a constant speed, whereas the two torches are immovable. The wire is automatically fed to the pool at a constant speed and the welding is conducted using a constant current level. Two voltage signals per tank are acquired in real-time (one voltage for each side of the tank) with a sampling rate of 25 Hz. We obtain signals consisting of 2800 points. An example of a voltage signal from a normal welding cycle is shown in Fig. 2.10 (a). The normal voltage signal is non-periodic with a global trend that reflects the overall shape of the cap and the cylinder as voltage correlates to the electric arc length. The trend can be different from one signal to another and the signal can be non-stationary without presenting any anomalies, as we saw in Chapter 1.

The anomalies are very often subsequences with unusual shapes and amplitudes that would indicate burn-through, misalignment, etc. Fig. 2.10 (b) shows a signal with an anomaly highlighted in red, corresponding to a hole in the weld. Since the anomalies have high amplitudes, it is important

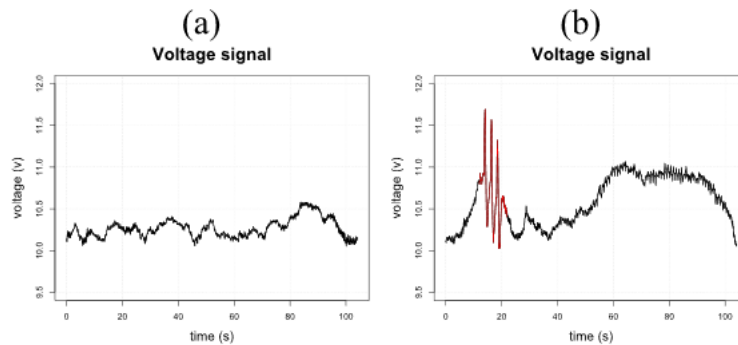


Figure 2.10: Example of a normal signal (a) and a signal with an abnormal subsequence (b).

that the subsequences are not z-normalized. We only center them, since the difference in the mean is not an indication of a defect.

2.4.2 The orbital welding

Another welding process we are interested in is called the orbital welding, which consists in joining a connection part known as the nipple to the hot water tank tubes (Fig. 2.11). The welding of these parts is conducted using an automatic machine employing pulsed current GTAW process. During the welding cycle, the workpiece is fixed while the electrode orbits around it (Hence the name orbital welding). The pulse frequency is changed two times during the cycle: first when the electrode is situated below the tube, and then shortly before the end of the welding cycle. The location of the three frequencies that we shall refer to as $freq1$, $freq2$ and $freq3$ are shown on the voltage signal in Fig. 2.12. Varying the frequency was found to help avoid the effects of gravity on the weld pool and in getting better coalescence for upward welding. The voltage signals of this process are sampled at 20Hz, which produces signals of 1050 points for each welding cycle.

The voltage signal of the orbital welding is sometimes contaminated with spikes whose number is variable. In the $freq1$ part, which we shall call the first part of the signal, the number of spikes tends to be low while in the rest of the signal, called the second part, there can be signals with an important number of spikes as Fig. 2.13. shows.

One of the challenges in the anomaly detection domain is to differentiate between noise and

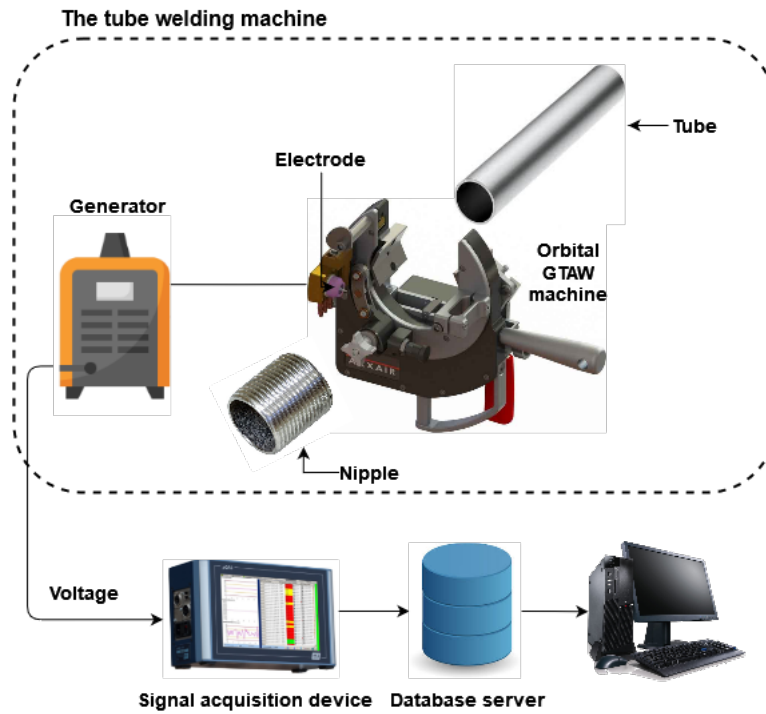


Figure 2.11: The setup of the orbital welding of nipples.

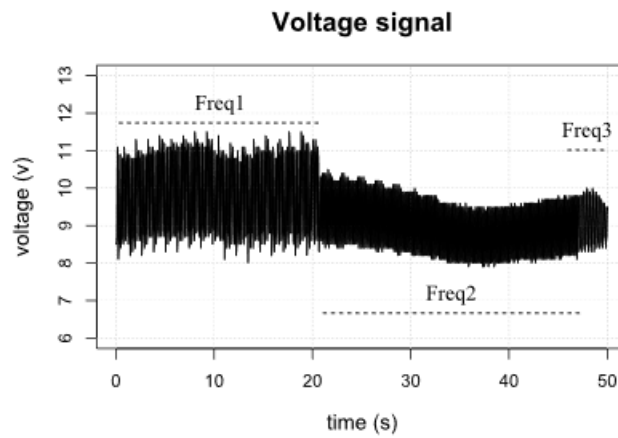


Figure 2.12: An example of a normal voltage signal of the orbital welding.

anomalies (Shaukat et al. (2021)). Therefore, it is more convenient to clean the signals at the preprocessing stage for more efficient anomaly detection.

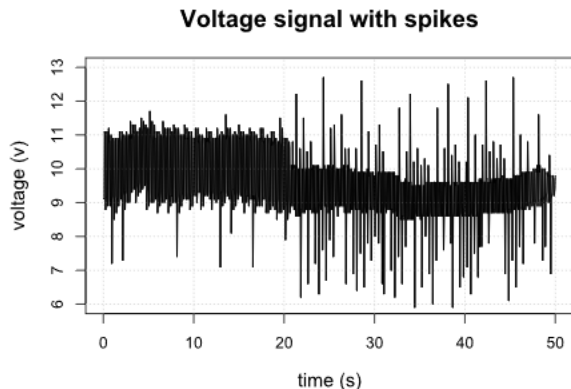


Figure 2.13: An example of a signal with spikes.

There exist some methods in the literature for spike elimination. The most simple one is to eliminate the points that are higher or lower than some threshold. Costabel et al. (2014) employs an approach in which points outside the interval $[\bar{x} - \tau * \sigma_x; \bar{x} + \tau * \sigma_x]$ are considered spikes where \bar{x} is the mean of the signal x_t and σ_x its standard deviation while τ is a predefined factor. This technique might be effective. However, it implicitly assumes that the time series follows a normal distribution and is stationary. Furthermore, it can be difficult to determine the appropriate factor τ as the number of spikes is variable in our case. We test this method in our study with $\tau = 3$ and we refer to it as temporal thresholding in what follows. In order to meet the assumption of stationary, first the signal trend is extracted using a low pass filter, and the thresholding is applied to the detrended part. The signal is then reconstructed by summing the trend and the thresholded oscillations.

Wavelet transform can also be used to remove spikes and noise from signals. In Costabel et al. (2014), the signal is decomposed using wavelet transform and subsequently reconstructed after eliminating the points outside a predefined range in the multi-resolution detail coefficients D_i for $i = 1, \dots, N$ where N is the number of the decomposition levels, the authors propose to eliminate the values that are above the so-called universal threshold defined as $\sqrt{2\sigma_i^2 \log(|D_i|)}$ where σ_i^2 is the variance of the detail coefficients D_i and $|D_i|$ the number of points in D_i . We consider this technique in our study, and we call it wavelets thresholding. We decompose the signal using the symlet6 mother wavelet, as proposed by Costabel et al. (2014).

The median filter is also a well-known despiking technique that has been used in several works (Brock (1986); Stone (1995); Ariannik et al. (2020)). A median filter of order $2K + 1$ replaces the value of the signal x_t by the median value of the sequence $[x_{t-k}, x_{t-k+1}, \dots, x_t, \dots, x_{t+k}]$. In our study, we use a median filter of order 3.

Fig. 2.14 shows the despiked signal obtained by the three considered methods for the *freq2* part of the signal in Fig. 2.13. The wavelets thresholding achieves some degree of despiking but produces a signal that looks very different from the original signal. Since there are a lot of spikes in this signal, the temporal thresholding keeps it almost identical, since only a small fraction of values are outside the predefined range. It is possible to reduce the value of the factor τ to obtain better results. However, when the signal has no spikes, this would still eliminate values from it, resulting in an altered signal. The median filter suppresses the unwanted spikes, but it also alters the signal as it eliminates some of the pulse waves, which results in flat regions.

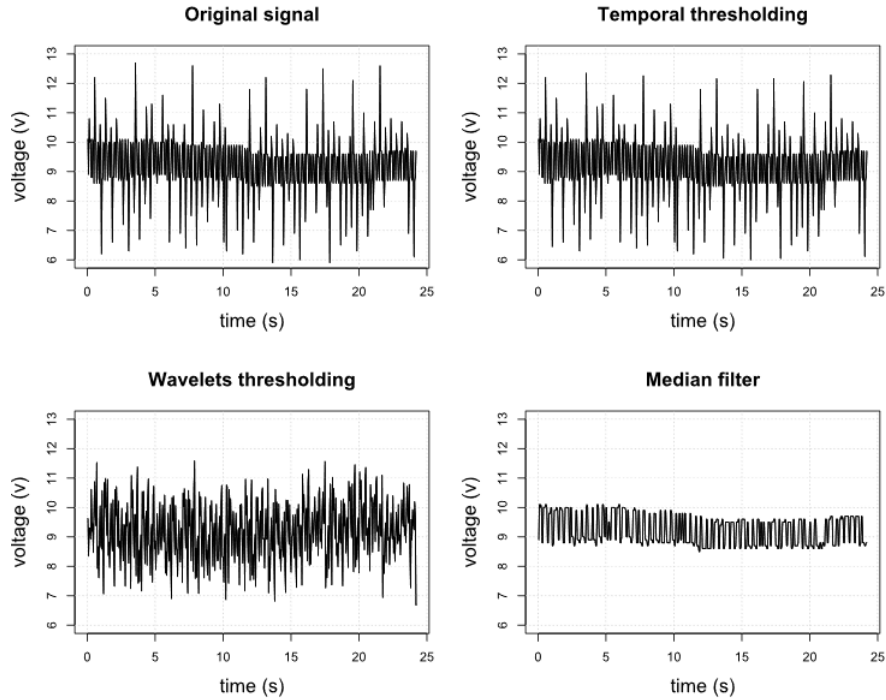


Figure 2.14: The despiked signal obtained by the despiking methods.

The three tested techniques do not give satisfactory despiking as they either do not eliminate the spikes as in the temporal thresholding, or modify the signal as in the wavelet thresholding and the median filter. These results might be due to the fact that the spikes in our signals do not follow assumptions of outliers; as stated earlier and illustrated by the second part of the signal in Fig. 2.13, there can be signals where spikes are present at every rising and falling edge, which does not match the assumption of the rarity of outliers.

This suggests that we need a more adaptive technique that does not make such assumptions. From Fig. 2.14, we notice that the envelope of the despiked signal obtained by the median filter corresponds to the envelope of an uncontaminated signal. We make use of this observation to derive

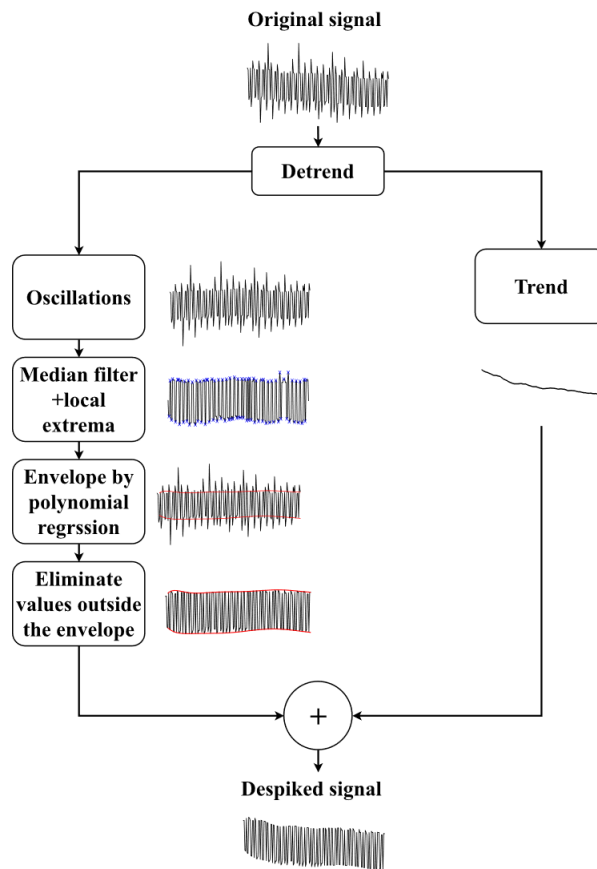


Figure 2.15: The proposed despiking method.

a more reliable despiking method for our signals.

The steps of the proposed method are shown in Fig. 2.15. First, the trend T_t is extracted from the signal x_t using a pass band filter with a cutoff equal 0.5Hz, and the oscillations O_t are obtained by subtracting the trend from the signal $O_t = x_t - T_t$. A median filter of order 3 is applied to O_t to obtain the filtered oscillations OF_t then the local minima and maxima are detected using a simple rule: if $OF_t > OF_{t-1}$ and $OF_t > OF_{t+1}$, OF_t is declared local maxima. Local minima are detected by inverting the inequalities: OF_t is local minima if $OF_t < OF_{t-1}$ and $OF_t < OF_{t+1}$. A polynomial regression model of order 20 is afterward fitted to the local extrema to detect the envelope of OF_t (The order was chosen based on observations of the fit). In the last step, we eliminate the values of the O_t that are outside the range given by the envelopes of OF_t and we sum the resulting signal with T to obtain the despiked signal. The obtained output signal with the proposed method for the considered signal is shown in Fig. 2.16. We notice that the spikes are completely eliminated

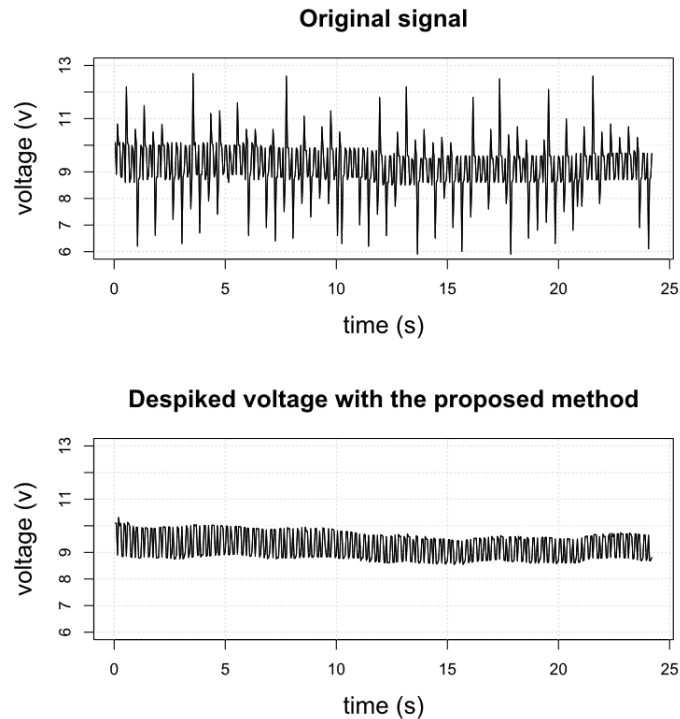


Figure 2.16: The despiked signal obtained with the proposed method.

without significantly altering the component of the signal we are interested in, which shows that the proposed technique is better than the three methods from the literature for these signals with a high number of spikes.

The technique is applied to the two parts of the signal separately (Fig. 2.17), the first part is composed of the waves of the first frequency $freq1$ while the second is the rest of the signal composed of $freq2$ and $freq3$. We do this because there is a drop in the amplitude at the transition from the first to the second frequency that can be difficult to fit with the polynomial regression. We consider the second part to be composed of $freq2$ and $freq3$ because $freq3$ represents a small portion of the whole signal, and there is no noticeable amplitude shift between $freq2$ and $freq3$.

The transition between frequencies is always at the same point in the signals. Thus, the parts can be easily separated without the need for automatic change point detection.

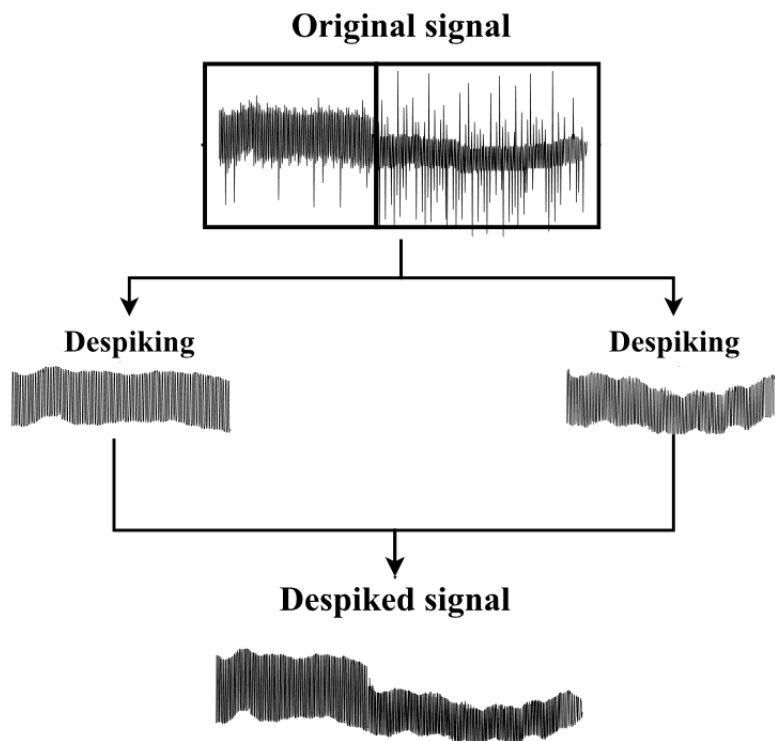


Figure 2.17: The strategy followed for signal despiking.

For anomaly detection, we also split the signal into two parts as in the signal despiking problem, and treat each of them separately. This is because the subsequences that are at the transition between *freq1* and *freq2* tend to be detected as anomalies, as they are rare events in the signal. Considering the whole signal would then generate a high false positive rate. Furthermore, splitting the signal in this manner simplifies the problem, as subsequences would be homogeneous in each case. As for the dissimilarity measure, we use the *lb_improved* since there can be phase shifts between the signals. The warping window constraint is set to 5, which is equal to the length of the longest period in the signal.

2.4.3 Cold Metal Transfer welding

We introduce here the welding of the connection tubes with the hot water tank cylinder conducted by a robotic arm shown in Fig. 2.18 that employs the cold metal transfer (CMT). CMT is a subset of the Gas Metal Arc Welding family. During this welding process (Fig 2.19), the wire travels forward until it contacts the welding pool, which causes a short circuit. As soon as the short circuit is detected, a signal is sent to the servomotor to retract the wire. The current is kept at a low level, which gives time for the drop to cool. The arc is then reignited, and the process restarts in a loop until the weld ends (Selvi et al. (2018)).

Fig. 2.20 shows voltage and current signals acquired during this process. Since there are multiple tubes in the hot water tank (their number ranges from 2 to 6), we obtain a signal composed of several sub-signals. Moreover, this welding is used to reinforce the intersection between the circular and the longitudinal welds, the last two sub-signals correspond to this operation. We notice that there is a peak in voltage before every welding. This corresponds to the signal used by the robotic arm feeler before the arc ignition.

The first task that we need to complete to work with this data is to separate the sub-signals, for this, we use a segmentation method shown in Fig 2.21 that works as follows:

- Transform the current signal using the roll-max function, which consists in returning the maximum value of every sequence of length w in the signal extracted by a moving window. This helps in detecting the upper envelope of the signals.

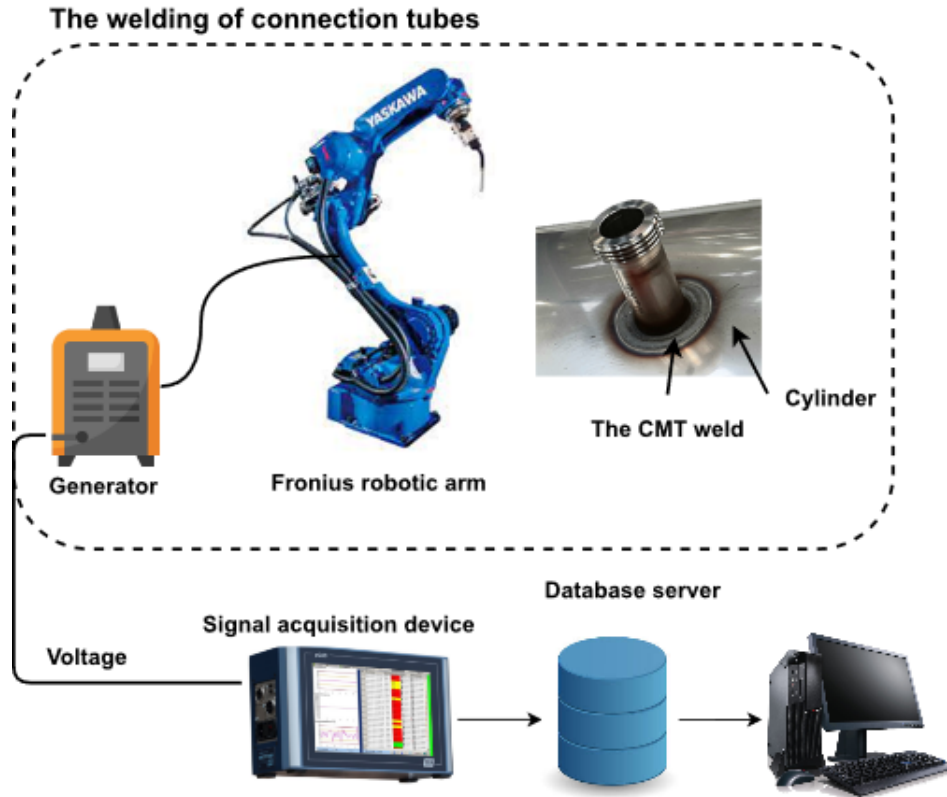


Figure 2.18: The setup of the CMT process.

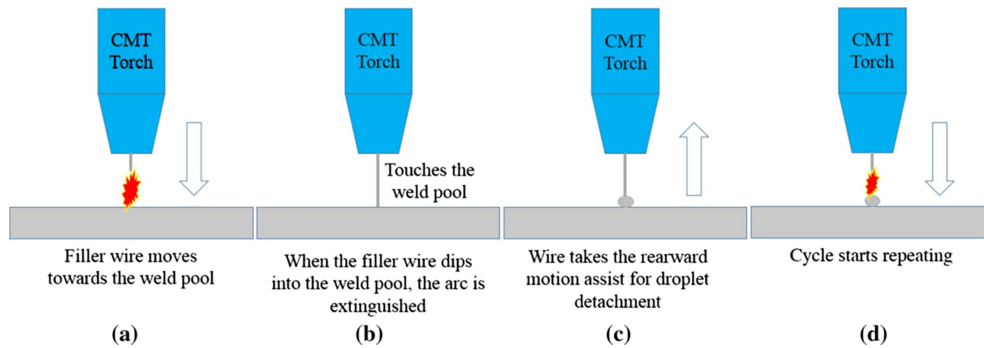


Figure 2.19: Illustration of the CMT process (Srinivasan et al. (2022)).

- Compute a binary mask by thresholding the transformed signal. This gives the value of 1 for regions where there is a sub-signal and 0 elsewhere.

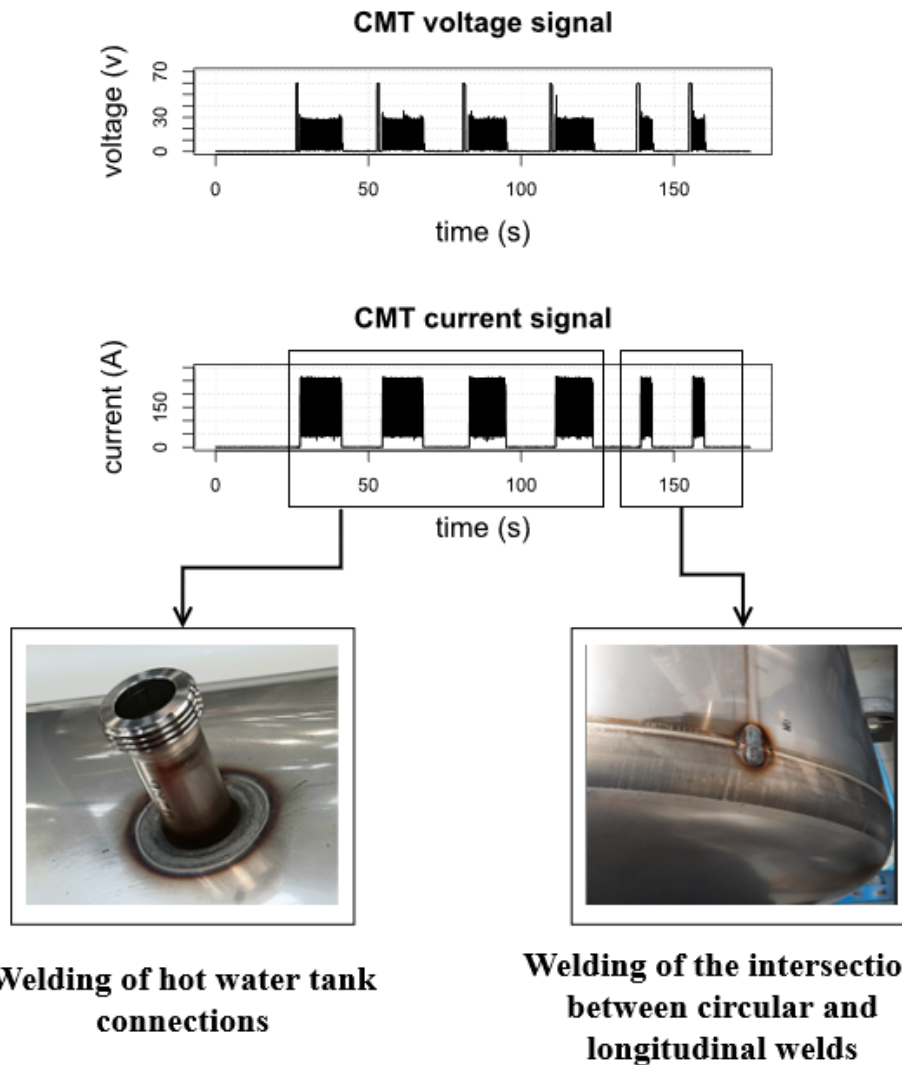


Figure 2.20: Voltage and current signals and the corresponding welds of the sub-signals.

- Compute the first lag difference of the binary mask in order to obtain the location of the change points. The value of 1 indicates the beginning of a sub-signal, and -1 indicates its end.

These voltage signals can also be contaminated with spikes. Their elimination is simpler here since the signals have a slow-changing trend and the peaks are rare. We then apply the method shown in Fig 2.22. We use a non-overlapping moving window, and for each window, we detect

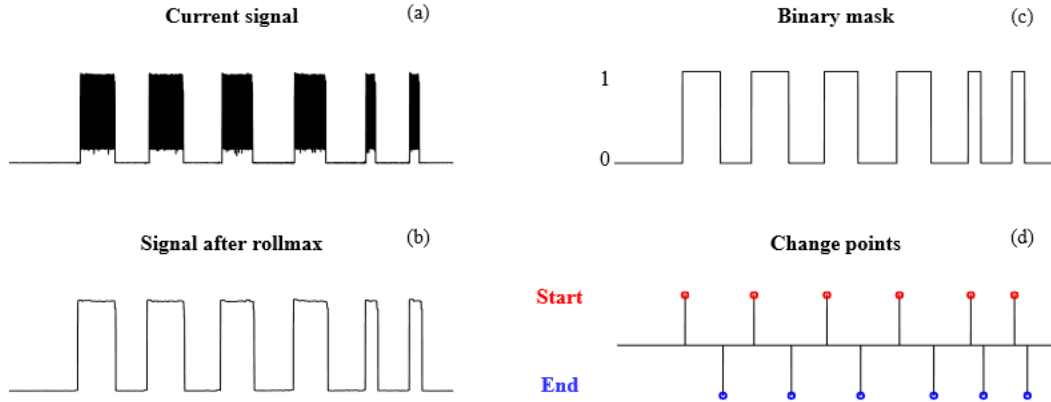


Figure 2.21: The segmentation method.

extrema by employing the same technique used for the problem of the despiking of the orbital welding signals. We then replace the values at these locations with the median of the extrema. The size of the window is fixed at 50 points in order to not eliminate anomalies and to preserve the global trend of the signal.

An important observation is that the length of the sub-signals is variable. A histogram of the lengths of a sample of 3000 sub-signals is given in Fig. 2.23. We notice that there are three distinct sub-signal groups. The first has a median of 599 and a standard deviation of 38.81. This corresponds to the two last welds of the intersection between the longitudinal weld and the circular weld, as shown in Fig. 2.20. The second and the third groups, which correspond to the welding of the connections, have medians of 1930 and 2144 with a standard deviation of 25.74 and 29.77 respectively. This is because there are in fact tubes with two different diameters. The variations in the length for each sub-signal group might be due to errors in the segmentation and the differences in the diameter of the tubes in each group.

Unlike the two previous processes, the current signal in CMT is not constant for all the cycles and seems to provide more information about the welding operation. When computing the Pearson correlation between each voltage sub-signal and its corresponding current in the sample considered earlier, we found that the mean correlation is 0.862 with a standard deviation of 0.015. A histogram showing the correlation values is given in Fig. 2.24. We also noticed that there is an outlier instance

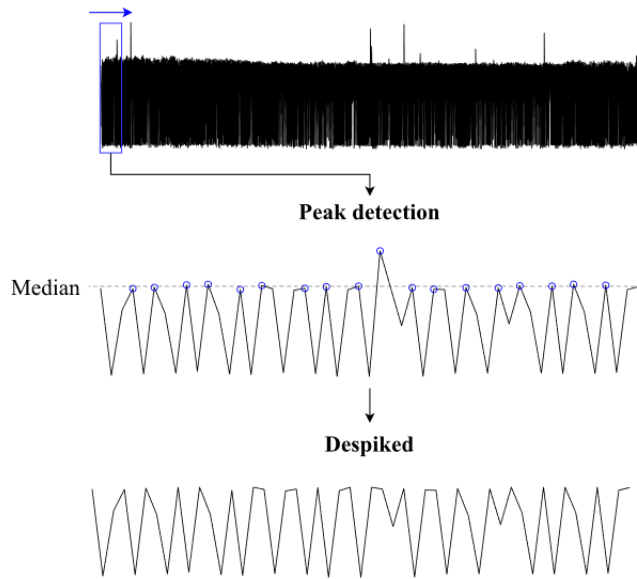


Figure 2.22: The despiking technique used for the CMT signals.

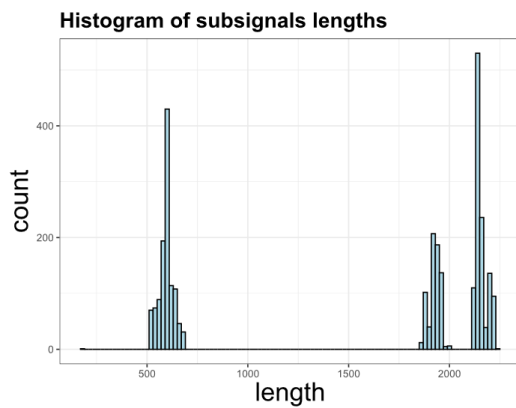


Figure 2.23: Histogram of the sub-signals lengths.

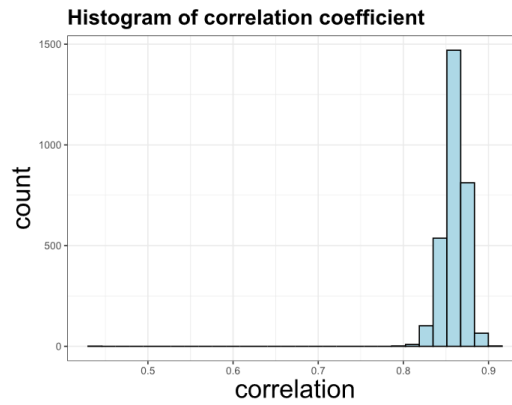


Figure 2.24: Histogram of the correlation between current and voltage.

where the correlation value is equal to 0.5. The corresponding weld was in fact faulty, which suggests that the correlation between current and voltage can be an interesting feature for anomaly detection. However, it might be a strong assumption to consider that only the correlation can be used to detect anomalies, we can imagine a scenario where the current and the voltage are highly correlated but still abnormal. We will see later in the manuscript that this is still a relevant observation when

we introduce the problem of multivariate time series anomaly detection. For now, we maintain the assumption that the voltage signal is the variable that holds most of the information for welding defect detection.

A final observation to take into consideration for anomaly detection is that the welding of the connection tubes and the welding of the intersection can have different dynamics. Hence, we believe that it is more convenient to treat each of them separately in the anomaly detection process. Furthermore, there can be phase shifts between the signals. Therefore, in the distance-based techniques and in our approach, we employ the DTW lower bound *lb_improved* to align the subsequences with a warping window of 3.

2.5 Results and discussion

In this section, we give the results of abnormal subsequence detection in the signal of the three welding processes following the defined strategies and the experimental protocol presented in section 2.3.5. Table 2.2 gives the number of the normal and abnormal subsequences used for each welding process along with their lengths, which are set by prior knowledge of the length of anomalies in the signals.

We begin with the circular process. Table 2.3 gives the F1-scores of the approaches for each of the 5 test subsets, along with the average F1-score and the average inference time. The OC-SVM models with both kernels have the best performance in terms of the average F1-score and the prediction time. The maximum mean F1-score of 0.947 is obtained with the OC-SVM model with

Table 2.2: Number and length of the subsequences used for each signal.

Process	Normal subsequences	Abnormal subsequences	length
Circular welding	6000	200	200
1 st part of the orbital welding	5000	50	100
2 st part of the orbital welding	5000	100	100
CMT connection welding	2000	200	200
CMT intersection welding	2000	200	100

the *RBF* kernel. The OC-SVM models are the fastest since they only require the distances to the support subsequence. For the one with the *RBF* kernel, one single support subsequence is used for the prediction for each subset, while the OC-SVM model with the *ND* kernel needed 3 support subsequences on average for each subset. The next fastest method is the autoencoder. However, it has a much higher training time compared to the OC-SVM models. The k -NN based methods do not require any training, but they needed 6.11 seconds for the prediction. Given that the number of the test subsequences used here is less than the number of the subsequences of a single voltage signal, these methods might not be adequate for real-time monitoring. The approach combining the features and Isolation forest is the slowest, namely because calculating the designed features requires a considerable amount of time. Overall, although all approaches exhibit good accuracy in detecting anomalies in the circular welding process, the proposed approach is much faster.

We move now to the signals of the orbital welding process. Table 2.4 gives the results of the models

Table 2.3: Results for abnormal subsequence detection in the circular welding process.

Model	F1-score 1	F1-score 2	F1-score 3	F1-score 4	F1-score 5	Mean	Time
OC-SVM <i>RBF</i> L_2	0.959	0.941	0.943	0.957	0.939	0.947	0.01
OC-SVM <i>ND</i> L_2	0.948	0.937	0.943	0.950	0.932	0.942	0.026
k^{th} -NN L_2	0.943	0.945	0.911	0.943	0.943	0.937	6.11
Mean k -NN L_2	0.952	0.946	0.913	0.943	0.946	0.940	6.11
Features & IForest	0.928	0.913	0.926	0.932	0.924	0.924	8.94
AutoEncoder	0.950	0.930	0.939	0.948	0.932	0.939	0.21

Table 2.4: Results for defect detection in the first part of the tube welding signal.

Model	F1-score 1	F1-score 2	F1-score 3	F1-score 4	F1-score 5	Mean	Time
OC-SVM <i>RBF</i> $lb_improved$	0.935	0.901	0.885	0.862	0.885	0.89	0.11
OC-SVM <i>ND</i> $lb_improved$	0.943	0.980	0.952	0.926	0.971	0.954	0.044
k^{th} -NN $lb_improved$	0.901	0.901	0.901	0.885	0.917	0.90	3.59
Mean k -NN $lb_improved$	0.893	0.909	0.862	0.87	0.87	0.88	3.59
Features & IForest	0.826	0.814	0.766	0.769	0.8	0.795	6.17
AutoEncoder	0.820	0.845	0.787	0.794	0.726	0.794	0.15

Table 2.5: Results for defect detection in the second part of the tube welding signal.

Model	F1-score 1	F1-score 2	F1-score 3	F1-score 4	F1-score 5	Mean	Time
OC-SVM <i>RBF</i> $lb_improved$	0.980	0.971	0.99	0.966	0.995	0.980	0.14
OC-SVM <i>ND</i> $lb_improved$	0.99	0.976	1	0.99	1	0.991	0.10
k^{th} -NN $lb_improved$	0.889	0.881	0.889	0.913	0.893	0.893	3.37
Mean k -NN $lb_improved$	0.901	0.889	0.909	0.913	0.881	0.898	3.37
Features & IForest	0.87	0.851	0.858	0.866	0.844	0.857	6.38
AutoEncoder	0.909	0.926	0.917	0.917	0.901	0.914	0.16

for the first part. For these signals, the feature-based method and the autoencoder have the lowest F1-scores of approximately 0.80. For the former, the reason can be that the extracted features are not optimal for this data and cannot perfectly differentiate between normal and abnormal subsequences. For the autoencoder, it might be because these signals are complex due to the distortions between them. Hence, for the autoencoder to work better, it would require more data. The distance-based methods are more accurate since the dissimilarity used allows better detection. The OC-SVM with the ND distance has the highest average F1-score of 0.954 and the lowest inference time. It required only 2 support subsequences for the prediction in each subset, while the OC-SVM using the RBF kernel needed 17 support subsequences on average.

The results for the second part of the signal are presented in Table 2.5. It reveals that using the OC-SVM with both kernels performs the best once again, achieving mean F1-scores of 0.980 and 0.991 using the RBF and ND kernels respectively. The autoencoder had a mean F1-score of 0.914, which is higher this time than the ones obtained with the k -NN approaches. The IForest technique with the features had the lowest F1-score and the largest inference time.

From Table 2.4 and Table 2.5 we notice that the OC-SVM model with the ND kernel performs better than the one with the RBF model, especially for the first part of the signal. This suggests that the assumption that the hypersurface containing the normal data is perfectly spherical is more accurate for these signals.

Results for the CMT welding process are given in Table 2.6 and Table 2.7 for the connection tube welding and the intersection welding respectively. For both problems, the ranking of the methods in terms of the F1-score is similar to the one obtained for the other welding processes, the OC-SVM models with both types of kernels maintain the highest average F1-scores and lowest inference time compared to all other methods while the k -NN based approaches have higher average score than the autoencoder and the features with IForest for both problems.

The first conclusion to make from the presented results is that all the approaches achieve an F1-score higher than 0.8 in most of the cases. This is in part due to the preprocessing steps and also to the strategies followed where homogeneous signals are treated separately, as well as our attempts to optimize each approach. The findings of this study show that the OC-SVM with distance substitution kernels achieves the highest accuracy and the lowest prediction time for all the

Table 2.6: Results for abnormal subsequence detection in the connection tube welds.

Model	F1-score 1	F1-score 2	F1-score 3	F1-score 4	F1-score 5	Mean	Time
OC-SVM <i>RBF lb_improved</i>	1	1	1	0.995	1	0.999	0.064
OC-SVM <i>ND lb_improved</i>	1	1	1	0.995	1	0.999	0.03
k^{th} -NN <i>lb_improved</i>	0.998	1	0.998	0.998	1	0.998	1.516
Mean k -NN <i>lb_improved</i>	0.983	0.993	0.988	0.99	1	0.990	1.516
Features & IForest	0.971	0.980	0.978	0.988	0.971	0.978	4.454
AutoEncoder	0.995	0.995	0.980	0.980	0.990	0.988	0.501

Table 2.7: Results for abnormal subsequence detection in the intersection welds.

Model	F1-score 1	F1-score 2	F1-score 3	F1-score 4	F1-score 5	Mean	Time
OC-SVM <i>RBF lb_improved</i>	0.998	0.998	1	0.995	1	0.998	0.05
OC-SVM <i>ND lb_improved</i>	0.99	0.995	0.998	0.985	0.988	0.991	0.05
k^{th} -NN <i>lb_improved</i>	0.971	1	0.983	0.983	0.993	0.986	0.754
Mean k -NN <i>lb_improved</i>	0.976	0.998	0.985	0.973	0.988	0.984	0.754
Features & IForest	0.978	0.975	0.950	0.971	0.988	0.972	3.87
AutoEncoder	0.971	0.975	0.972	0.975	0.970	0.973	0.157

considered welding processes. The gain in inference time is clear especially when compared to the other distance-based approaches, suggesting that the OC-SVM with distance substitution kernels is well-suited for detecting abnormal subsequences in time series data, particularly in welding signals, which allows real-time monitoring of the welding operation and to search anomalies in historical data, namely in order to extract knowledge such as trends of the occurrence of defects over time or clustering similar anomalies.

Concerning the non-positive definiteness of the similarity matrix obtained with the lower bound of the DTW and DS kernels, the findings of the presented experimentation show that, despite that DTW and its lower bound *lb_improved* are theoretically non-metric, OC-SVM can still achieve high accuracy. These good results of OC-SVM with this non-metric dissimilarity can be explained by the fact that positive definiteness is weakly violated. In fact, Lemire (2009) demonstrated that for same length time series, the DTW satisfies a weakly triangular constraint and is unlikely to violate the triangular inequality in real-world data. Formally, the weak triangular inequality for three sequences x , y and z of the same length m is defined as following:

$$DTW_p(x, y) + DTW_p(y, z) \geq \frac{DTW_p(x, z)}{\min(2r + 1, m)^{1/p}} \quad (2.22)$$

Where p is the order of the L_p distance used in the DTW and r is the warping constraint.

This weak triangular inequality combined with the fact that the Sequential Minimal Optimization algorithm, used to solve the optimization problem of the SVMs, can still guarantee finding a good local optimum (Bahlmann et al. (2002)) when using indefinite kernels, which explains the good results obtained by the OC-SVM with the *lb_improved* dissimilarity. To further confirm the performance of the approach, we test it in Appendix B for the problem of abnormal whole time series detection.

Fig. 2.25 gives examples of signals from the three welding processes analyzed by the OC-SVM employing the *ND* kernel, along with the produced anomaly scores. We notice that the abnormal subsequences are perfectly identified by the models. This shows the ability of the approach to learn the expected shapes of the normal subsequences and to detect any abnormal shape that is not seen in the training data. For the circular welding signals in Fig. 2.25 (a) the abnormal subsequences are abnormal shapes with high amplitude. Fig. 2.25 (b) and Fig. 2.25 (c) show examples of signals of the orbital and the CMT welding respectively. The anomalies here are abnormal shapes regardless of their amplitude, they can be parts where there is an absence of the oscillations or oscillations with abnormal frequency observed especially in the signals of the CMT process, indicating an abnormal short circuit frequency.

We were interested in our work only in detecting anomalies of voltage signal since it is the variable where there is most of the information about anomalies as the voltage is correlated with the electric arc dynamics. However, it is possible that practitioners will be interested in detecting anomalies in multivariate signals having more variables of the welding operation such as the gas flow or the current in the CMT process, etc. The simplest extension is to treat each variable as a univariate time series. However, one shortcoming of this approach is that we need a model for each variable. A more appropriate extension would be to use a dissimilarity measure that is able to handle multivariate time series in the kernel function. For example, the generalization of the L_2 distance defined for two multivariate time series subsequences s and s' of length m and with dim dimensions as:

$$ED_m = \left(\sum_{k=1}^{dim} \sum_{i=1}^m |s_i^k - s_i'^k|^2 \right)^{\frac{1}{2}} \quad (2.23)$$

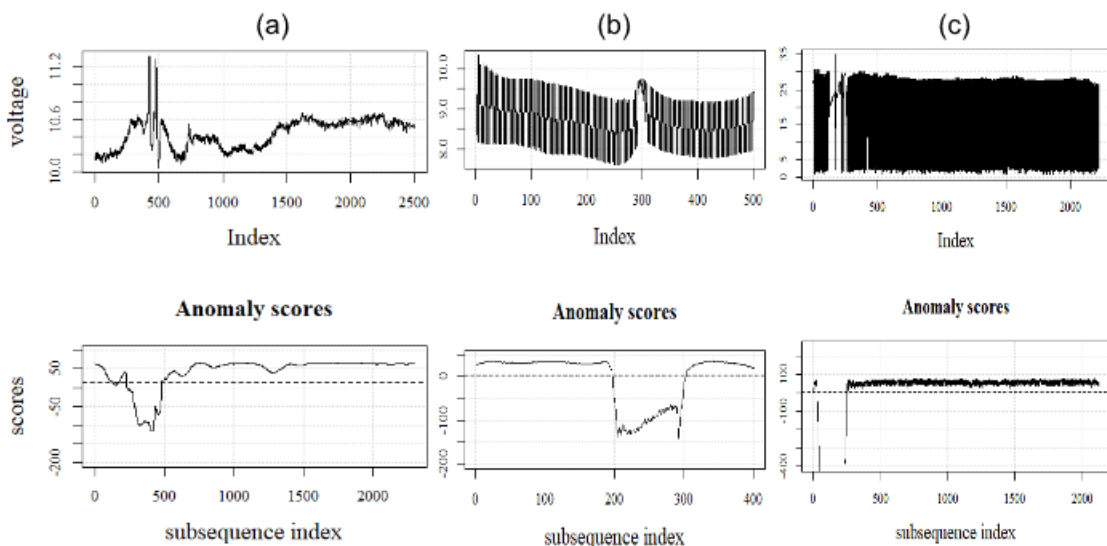


Figure 2.25: Examples of signals and the associated anomaly scores for each subsequence. (a) The circular welding, (b) the orbital welding, and (c) the CMT welding.

To show an example, consider the problem of detecting abnormal subsequence in a multivariate signal composed of voltage and wire feed speed of the circular welding. We fit an OC-SVM model using centered subsequences of length 200 of a normal signal. We employ the *RBF* kernel using the dissimilarity in Eq. 2.23 with the *RBF* parameter $\gamma=0.05$. The results of the prediction of two signals with abnormal subsequences are shown in Fig. 2.26. The right-hand signal has an abnormal subsequence in the voltage signal, while the left signal has abnormal subsequences in the wire speed. We notice from the anomaly scores that these subsequences are perfectly detected, showing that the proposed approach can be used for anomaly detection in multivariate time series. Note that the abnormal subsequences detected in the wire speed signal do not indicate the presence of a welding defect, which is the reason that we only worked with the voltage signals.

Despite the good detection results shown in Fig. 2.26, a shortcoming of using the dissimilarity in Eq 2.23 is that it does not take into account the correlation between the variables in the multivariate signal. As we saw in the Cold Metal Transfer welding, there is a high correlation between voltage and current in a typical normal operation while we observed that in an abnormal weld, there was a decrease in the correlation. A more convenient dissimilarity measure should take into consideration the correlation structure. In future works, it would be interesting to study the use of OC-SVM

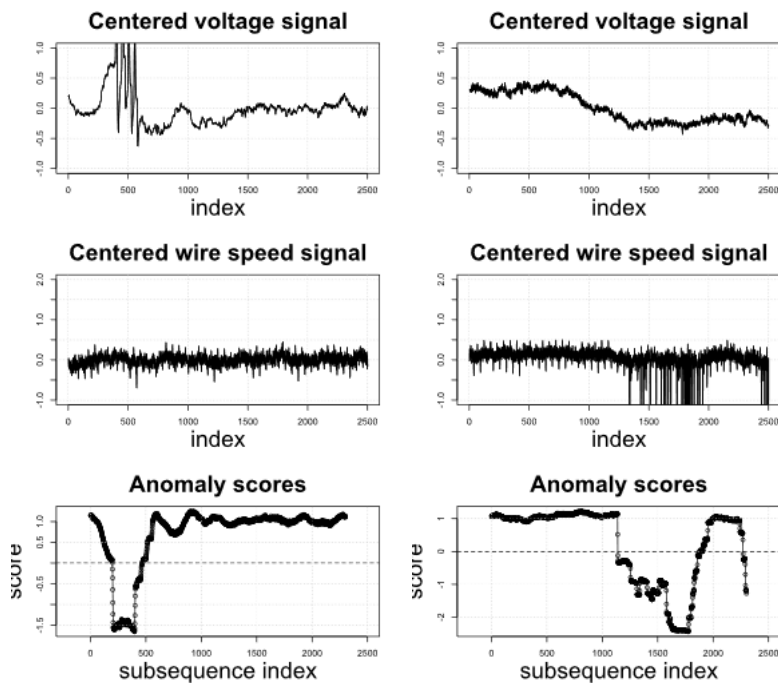


Figure 2.26: Examples of multivariate welding signals along with the produced anomaly scores.

with the Extended Frobenius norm (EROS) proposed by K. Yang et al. (2004), which is a similarity that is based on Principal Component Analysis (PCA) in order to take into account the correlation between variables in a multivariate time series. Another approach to study in future works would be to first perform PCA to transform the multivariate signals into a univariate time series prior to the use of the L_2 distance.

Like any method, the proposed approach for abnormal subsequence detection has some limitations that can be further addressed in future works, which are as follows:

- Despite that the sizes of the moving windows used to extract the subsequences were carefully set for the signals of each welding process, there is still a possibility that some anomalies will be missed because of the large difference in length between the anomalies and the size of the moving window. In Appendix D, we propose two approaches that can be used to detect variable length subsequences using Shape Based Distance (Paparrizos et al. (2015)) and Uniform Scaling (Keogh (2003)).

- Like any dissimilarity-based approach, the proposed approach relies on the choice of an adequate dissimilarity measure.
- The models do not automatically adapt to the change of normality over time.
- The anomaly detector does not offer interpretability of the predictions made.

For the circular welding process, this problem of interpretability is addressed by an automatic defect diagnosis that we present in the next subsection.

2.6 Welding defect diagnosis using Random Convolutional Kernel Transform

Abnormal subsequences in the welding voltage signals can be caused by multiple events such as burn-through, misalignment, etc. We are interested here in automatically classifying the most recurrent abnormal subsequences in the circular welding process. This would help the operator take adequate corrective actions that depend on the type of the detected anomaly. For example, if abnormal oscillations are detected, the operator would change the electrode or check the health state of the welding torch. Moreover, knowing the classes of the detected anomalies could help engineers to better understand the welding process and to optimize the product's design in order to minimize the apparition of faults, for example by analyzing the possible link between the type of observed anomalies and the product's design and its mechanical and the chemical composition.

Employing our approach for anomaly detection, we searched for abnormal subsequences in the available historical data and conducted a study to identify the classes of the most recurrent circular welding defects with the help of domain experts. We identified 6 classes shown in Fig. 2.27 along with their associated welding defect. The 1st class corresponds to a burn-through, the peak here shows that the arc lengthens due to a hole in the weld seam. The 2nd class is characterized by the low peak and indicates a possible weld skip, while the 3rd is a local misalignment between the cap and the ferrule. The 4th class are subsequences with a peak that indicates a hole and which is preceded by a gradual increase in the voltage. This suggests that the cause of the burn-through

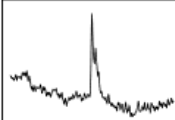

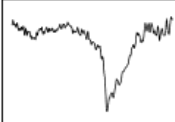

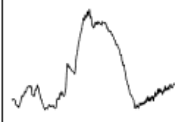



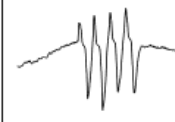

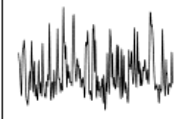

1. Burnthrough		
2. Weld skip		
3. Misalignment		
4. Burnthrough caused by misalignment		
5. Multiple Burnthroughs caused by misalignment		
6. Unusual weld seam shape		

Figure 2.27: The 6 most observed welding defects.

is the misalignment between the cap and the ferrule. The 5th is the same phenomenon but with multiple holes shown by multiple peaks in the abnormal subsequence. The last class shows abnormal oscillations, which can be caused by abnormal movements of the wire or a problem with the welding torch.

A noteworthy observation is that anomalies can be of different lengths despite the use of a fixed-size window to extract subsequences from the signal. This is because when analyzing the subsequences using the anomaly detector, we consider consecutive subsequences that have an anomaly score lower than the threshold to form a single welding defect. To give an example, consider a voltage signal with two defects shown in Fig. 2.28 along with the obtained anomaly scores for each subsequence. We notice that there are two distinct series of subsequences with an anomaly score lower than the threshold. These two series will be then combined to form two longer subsequences with different lengths that will be considered as two distinct welding defects to classify. We will

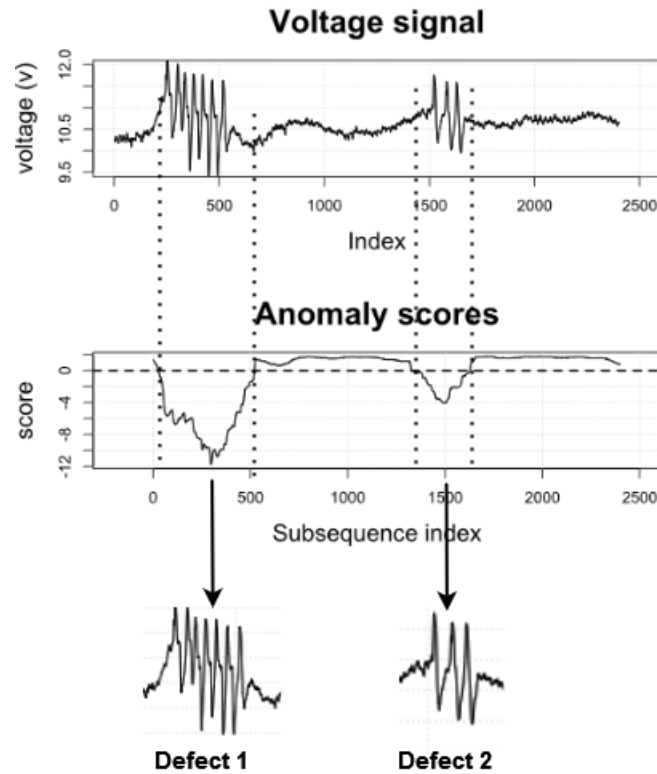


Figure 2.28: Illustration of the anomaly detection output (the anomaly scores) and how it is used to extract welding defects' signatures.

refer to these longer abnormal subsequences that we seek to classify in the remainder of this section as time series since they are non-overlapping.

The subject of time series classification has been highly studied in the literature, and many methods have been proposed. Time series classification methods can be divided into three categories (Xing et al. (2010), Abanda et al. (2019)):

- Features-based: consist in transforming the time series into a feature vector and the use of a classification method to classify the time series using their feature vector.
- Model-based: suppose that the time series in a class are generated by the same statistical model, they then classify a new instance based on the best fit to a model.

- Dissimilarity-based: incorporate a dissimilarity measure between time series into a classifier, very often k -NN classifier (Abanda et al. (2019)) similar to the anomaly detection domain.

A comprehensive review of the literature giving more information on this field is given in Bagnall et al. (2017).

Another important observation about the anomalies shown in Fig. 2.27 is that in some cases, it is a small segment that represents the class of the anomaly. For example, the increasing trend before the burn-through peak that differentiates between class 1 and class 4. This suggests that it is more convenient to use a method that can learn these parts of the subsequences that are representative of the class, rather than classifying the anomalies based on their global shape.

The first method that addresses this type of problem is called the Shapelets method, proposed by Ye et al. (2011). It is a method that classifies time series using some subsequences that are maximally representative of a class, called shapelets. The method uses the distances to these shapelets as a discriminatory feature. The brute force algorithm for automatically learning the shapelets has a complexity of $O(k^2\bar{m}^4)$ where k is the number of the time series in the training set and \bar{m} their average length. The authors proposed a faster shapelet search decision tree-like algorithm that combines early abandoning of the distance calculations and entropy pruning. In this algorithm, the minimum length of a shapelet is set at 3 while the maximum length is the length of the minimum time series in the dataset. Despite these improvements, the algorithm still had the worst-case complexity of $O(\bar{m}^4)$.

This led to further research for speeding up the shapelet search and extending the concept. For instance, Rakthanmanon et al. (2013) proposed the Fast shapelets method that uses a discretization of the time series rather than the raw representation in order to speed up the shapelet search. Hills et al. (2014) introduced the Shapelet Transform that represents a time series as a vector $v \in \mathbb{R}^k$ where each element is the minimum distance between the time series and the shapelet k . The goal was to overcome the shortcoming of the original Shapelet method allowing only the decision tree classifier. With the new representation of the data, any classifier can be used. The authors also suggest a heuristic to automatically estimate the minimum and maximum length of the candidate shapelets. Karlsson et al. (2016) proposed the Generalized Random Shapelet Forest that can

handle multivariate time series, which uses a randomized forest rather than a single decision tree as in the original method. Rather than searching for shapelets, Grabocka et al. (2014) introduced a mathematical formulation to jointly learn the shapelets and a linear hyperplane using a non-convex classification objective function.

Recently, a method called Random Convolution Kernel Transform (ROCKET) was proposed by Dempster et al. (2020), which is based on representing the time series to be classified by features extracted from the convolution of the time series with random convolutional kernels (also known as filters. Not to confuse with kernels used in methods like SVM) and using a linear classifier. The authors showed that there are similarities between ROCKET and shapelets despite the fact that shapelets are usually sampled from the input data while ROCKET uses random shapelets. The method achieved state-of-the-art accuracy while being faster than existing methods.

Since ROCKET meets both criteria of accuracy and fast inference, we use it to classify the welding anomalies in our work. Fig. 2.29 describes the ROCKET algorithm. The feature extraction part is based on the convolution, which is a sliding dot product, between the input time series x_t and the random kernel w . Each dot product is defined as follows:

$$z_i = x_i * w = \left(\sum_{j=0}^{l_{kernel}-1} x_{i+(j \times d)} \times w_j \right) + b \quad (2.24)$$

Where:

- l_{kernel} is the length of the kernel selected randomly from 7, 9, 11 with uniform probability.
- w are the weights of the kernel sampled randomly from a normal distribution $w \sim N(0, 1)$ and are afterward centered i.e. $w = (w - \bar{w})$
- b is the bias sampled from a uniform distribution, $b \sim U(-1, 1)$
- d is the dilation sampled on an exponential scale $d = 2^x$, $x \sim U(0, A)$ where $A = \log_2 \frac{l_{input}-1}{l_{kernel}-1}$. This ensures that the kernel's length including dilation is at most equal to the length of the input time series.
- Padding: for each random kernel, a decision is made at random if the padding will be used, if yes, zeroes are appended at the start and the end of the time series.

- k is the number of kernels. The higher the number, the higher the accuracy of the classification. The authors recommend using $k=10\ 000$.
- Stride is always equal to 1.

Two features are extracted from each convolution:

- ppv : The proportional of positive values defined as $ppv(Z) = \frac{1}{n} \sum_{i=0}^{n-1} [z_i > 0]$, where Z is the output of the convolution and n is the length of Z .
- mv : The maximum value of the convolution, also known as global max pooling in the neural networks' literature defined as $mv = \max(Z)$.

The $2 \times k$ features (two features extracted from each convolution) are then used to train a linear classifier. The authors propose to use logistic regression if the number of time series is higher than

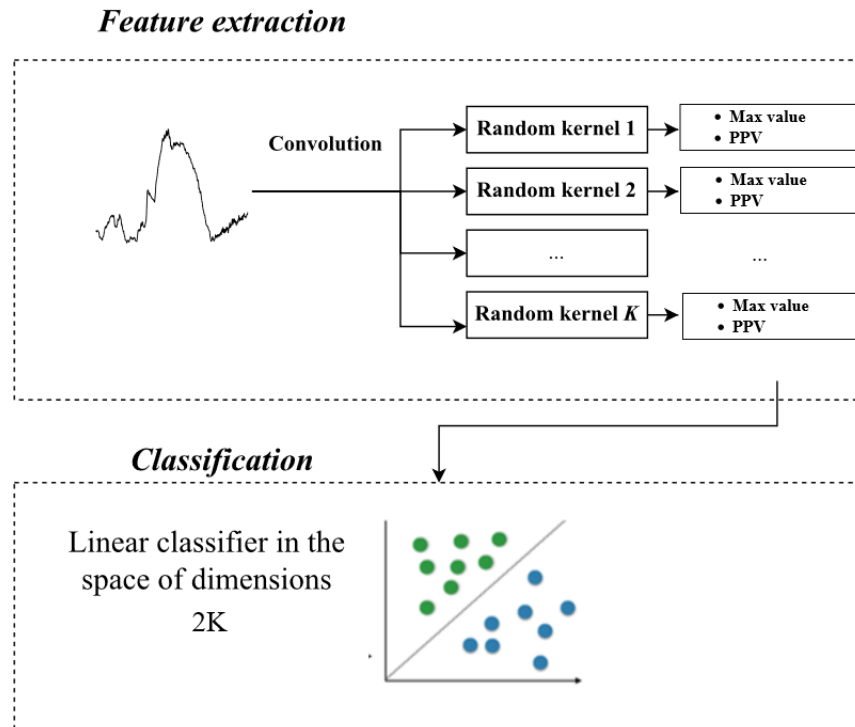


Figure 2.29: An illustration of ROCKET.

the number of features and ridge linear classifier with L_2 regularization otherwise.

To test ROCKET on our problem, we consider a dataset composed of 50 instances of each of the 6 defect classes. Since anomalies can have different lengths, we use zero padding to match the length of the maximum possible anomaly length, which is the length of the whole voltage signal. Despite the recommendation of ROCKET authors to use 10 000 kernels, much fewer kernels can be used for our case study. In order to select the proper number, we vary k from 100 to 5000. For each k , we run ROCKET 10 times and save the mean and the standard deviation of the accuracy produced. Fig. 2.30. shows a box plot of the accuracy obtained for k ranging from 100 to 5000 with a step of 100. We notice that from $k=500$ the accuracy starts to stabilize at 100% for most of the runs. We then select these 500 kernels for our case study. With this number of kernels, we ensure an accurate and fast classification of the anomalies of the circular welding process.

Combining the OC-SVM models and the diagnosis based on ROCKET. We developed software for real-time monitoring of the circular welding process that is used as a part of the process. More information about the developed software is given in Appendix C.

It is important to note that the diagnosis proposed here has some limitations that originate primarily from the assumptions made. First, we assumed that consecutive abnormal subsequences

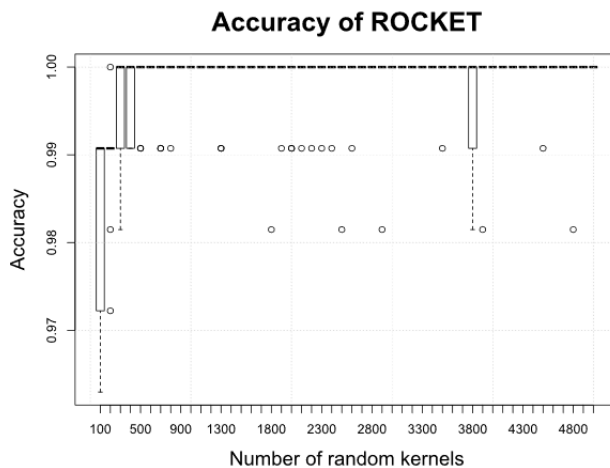


Figure 2.30: Accuracy of ROCKET as a function of the number of random kernels.

form a single welding defect. While this is true for most of the cases, it is not always valid. There can be scenarios where they indicate more than one defect type. Furthermore, we discussed earlier the fact that we classify here only the most observed abnormal subsequences. Therefore, once a new class of anomalies is detected by the anomaly detector, the diagnosis will then necessarily give a false prediction as the new class is unknown by the classifier.

One approach to address the above problems would be to integrate a reject option in the classification. There are two types of rejection: ambiguity rejection and distance-based rejection (Hanczar et al. (2008); Landgrebe et al. (2006)). The first addresses the problem of high uncertainty about which class to assign to an observation. In our case, this can be used to tackle the problem of when there is more than one welding defect in consecutive abnormal subsequences. A simple technique is to use a threshold on the probabilities given by the classifier. If the maximum probability is lower than the threshold, the classification is rejected. The distance-based reject option is similar to outlier detection and can be employed for the second problem in order to reject the classification of a defect that does not seem to belong to any of the known classes.

Rather than rejecting the classification, which might not be very useful in the context of welding diagnosis, another direction to address the ambiguity case is to assign soft labels to the anomalies by employing fuzzy classification. For the appearance of new types of defects, techniques employed in the field of classification with concept evolution can be used in order for the classifier to automatically adapt to the appearance of new classes.

2.7 Conclusion

In this chapter, we proposed a one-class classification approach for the detection of welding faults. Employing dissimilarity in the raw temporal data, we were able to generalize the anomaly detection across multiple arc welding processes. The results showed that the proposed approach with the adequate dissimilarity measure is able to detect anomalies in voltage signals of different natures with higher accuracy and faster inference time than most of the existing approaches. Moreover, the work of this chapter addressed a gap in the literature, which is the problem that OC-SVM cannot be used with the raw time series. We showed in this work that integrating distance substitution kernels

allows the OC-SVM to effectively work with the raw time series and time series subsequences. We studied distance substitution kernels with the Euclidean distance and a lower bound of dynamic time warping, and we gave justification of why such a theoretically non-metric dissimilarity can give high anomaly detection accuracy when used with the OC-SVM that normally requires a positive definite kernel. In future works, evaluating the performance of OC-SVM using other dissimilarity measures would be an interesting research direction, particularly those that are suitable for multivariate time series.

In addition to anomaly detection, we proposed in this work an automatic welding defect diagnosis for the circular welding process in order to predict the class of the anomalies detected. This proposed solution has been integrated into a software and is currently being utilized as part of the welding process. In future works, we plan to extend this automatic diagnosis to other welding processes, along with addressing its limitations that include the assumption that consecutive abnormal subsequences form a unique anomaly and the problem of the appearance of new classes of defects.

The OC-SVM with distance substitution has certain limitations. They include the fact that we employ a fixed-length moving window for analyzing the subsequences of the signals and the inability to automatically adapt to the change of the normality. Moreover, the approach relies on the choice of an adequate dissimilarity measure and does not offer information about the detected defects. These two last limitations are addressed in the next chapter.

Chapter 3

Welding defect detection using random convolutional kernel transform

Contents

3.1	Introduction	100
3.2	Methods	101
3.2.1	Random convolutional kernel transform with OC-SVM	101
3.2.2	Approach 1: Explainable abnormal subsequence detection using ROCKET	104
3.2.3	Approach 2: Dimensionality reduction techniques with ROCKET and OC-SVM	108
3.3	Results and discussion	109
3.3.1	Results of the first approach	111
3.3.2	Results of the second approach	116
3.4	Conclusion	123

3.1 Introduction

In the previous chapter, we noted that the OC-SVM with distance substitution (DS) kernels has the limitations of relying on the choice of the distance and the fact that it does not offer information about the anomalies detected. This chapter addresses these shortcomings by proposing approaches based on the random convolutional kernel transform (ROCKET). As we saw earlier, ROCKET was originally proposed for time series classification, and we used it for classifying the circular welding defects. Nevertheless, this specific transformation has not been employed for detecting abnormal subsequences in time series data. To the best of our knowledge, this is the first work using ROCKET for this purpose. ROCKET is interesting due to its ability to generalize well across various problems, and because the random convolutional kernels can serve as basic shapes that could help explain the abnormal patterns within the detected abnormal subsequences.

Explaining the prediction of machine learning models became an important research topic in recent years. However, little attention is given to explaining models based on temporal data (Tripathy et al. (2022)). Hence, there is a need for research work addressing this subject. Explainability in anomaly detection consists in explaining why an anomaly is considered anomalous, and this is by anomaly description and outlying property detection (Z. Li et al. (2022)). One interpretable technique for time series classification is the shapelet transform that we presented in the previous chapter. Since shapelets are local patterns that are maximally representative of a class, explainability is readily obtained by visualizing the shapelets associated with each class. However, this is only valid for multi-class classification, since the shapelets search is guided by the labels. For one class classification, Yamaguchi et al. (2018) proposed an algorithm that learns the shapelets of the normal class of time series. However, these shapelets are representative of only the normal class and might not be used to explain the abnormal shapes of the anomalous class. On the other hand, the random convolutional kernels offer random shapelets that can be used to explain the abnormal patterns of the anomalous time series subsequences in our case, even if the training is only done using the normal subsequences, as they are random and not characteristic of the normal class. Following this key assumption, we make use of ROCKET to derive a method for explainable time series subsequence detection.

In summary, two main approaches are proposed in this chapter that address the discussed shortcomings of OC-SVM with DS kernels:

- **Explainability:** We propose an explainability approach making use of the random convolutional kernels and the maximum value extracted from their convolutions with the subsequences.
- **Generalization:** We study the use of ROCKET with unsupervised feature selection techniques and OC-SVM in order to investigate the possibility of developing an abnormal subsequence detection approach that generalizes well to different problems while preserving computational efficiency.

The two aspects will be studied using two separate approaches. The chapter is structured as follows: in section 3.2 we present the methods and materials that cover the extension of ROCKET for anomaly detection using OC-SVM, the explainability technique that we will use in the first approach, and the feature selection and reduction techniques that will be used in the second approach. In section 3.3 we present the results of the two approaches we propose, and we finish with conclusions and future works.

3.2 Methods

3.2.1 Random convolutional kernel transform with OC-SVM

We reintroduce here the feature extraction part of the ROCKET method proposed by Dempster et al. (2020) that is based on the convolution, which is a sliding dot product, between the input time series x_t and the random kernel w . Each dot product is defined as follows:

$$z_i = x_i * w = \left(\sum_{j=0}^{l_{kernel}-1} x_{i+(j \times d)} \times w_j \right) + b \quad (3.1)$$

Where:

- l_{kernel} is the length of the kernel selected randomly from $\{7, 9, 11\}$ with uniform probability.
- w are the weights of the kernel sampled randomly from a normal distribution $w \sim N(0, 1)$ and are afterward centered i.e. $w = (w - \bar{w})$
- b is the bias sampled from a uniform distribution, $b \sim U(-1, 1)$
- d is the dilation sampled on an exponential scale $d = 2^x$, $x \sim U(0, A)$ where $A = \log_2 \frac{l_{input}-1}{l_{kernel}-1}$. This ensures that the kernel's length including dilation is at most equal to the length of the input time series.
- Padding: for each random kernel, a decision is made at random if the padding will be used, if yes, zeroes are appended at the start and the end of the time series.
- k The number of kernels.
- Stride is always equal to 1.

Two features are then extracted from each convolution, which are:

- $ppv(Z) = \frac{1}{n} \sum_{i=0}^{n-1} [z_i > 0]$: The proportion of positive values. Where Z is the output of the convolution and n is the length of Z .
- $mv = \max(Z)$: The maximum value of the convolution. It gives the maximum similarity between the random kernel and the shapes in the time series.

The focus of the work of this chapter is to examine the use of features obtained from convolutions with random kernels for the problem of abnormal subsequence detection. We aim to accomplish the two main objectives mentioned earlier, and that will be studied with two distinct approaches. In the first, we intend to develop a method that can identify abnormal subsequences and provide an explanation by making use of the random kernels. In the second, we prioritize achieving high accuracy, computational efficiency, and the ability to generalize the approach across the different welding signals introduced in the preceding chapter.

The two approaches are depicted in Fig. 3.1. In the first approach that addresses explainability, we extract the maximum values mv of the convolutions of the subsequences with a number of

random kernels to form the feature vectors that are used as inputs to an OC-SVM model that learns the hypersurface containing the normal class. Our choice of the OC-SVM is again motivated by the fact that it is fast at inference, as it relies only on the distance to the support vectors, which is an important advantage here as we may require a high number of random convolutional kernels to detect and explain abnormal subsequences and since there are possibly a high number of subsequences in a welding signal. To predict if a new subsequence is normal, first, its features are extracted using the random convolution kernels generated at the training stage that are subsequently passed to the OC-SVM model that returns an anomaly score reflecting its degree of abnormality. If the subsequence is abnormal, we follow the explainability technique that we present shortly to give an explanation about why it is considered abnormal.

In the second approach depicted in Fig. 3.1 (b), we investigate the use of feature vectors that consist of mv only, ppv only, and both mv and ppv , and we study the accuracy obtained for each case in order to select the more accurate models. Prior to modeling the normal class using OC-SVM, the features are first reduced using unsupervised dimensionality reduction techniques in order to reduce

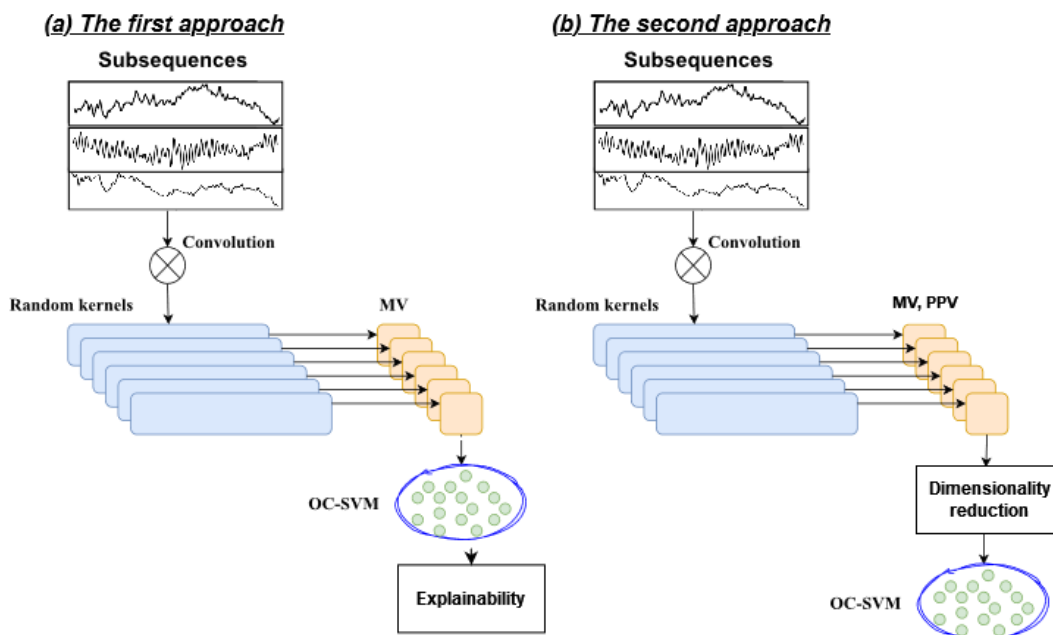


Figure 3.1: An illustration of the two proposed approaches.

the computational complexity while maintaining good detection accuracy. To test the normality of an upcoming subsequence, its features are extracted using ROCKET and reduced before predicting its class by the trained OC-SVM model. The two approaches are detailed in the next subsections.

3.2.2 Approach 1: Explainable abnormal subsequence detection using ROCKET

In this first approach, we would like to make use of the random convolutional kernels in order to derive a method that is able to provide information about the anomalies detected. In recent years, there has been growing interest in explaining machine learning predictions. Nevertheless, there has been little focus on explaining models based on temporal data (Tripathy et al. (2022)). There is a need for research work addressing this gap. Explainability in anomaly detection consists in explaining why an anomaly is considered anomalous, and this is by anomaly description and outlying property detection (Z. Li et al. (2022)). There are multiple types of explainability strategies that can be used to achieve this. According to Tripathy et al. (2022), they can be classified into, explainability by example, feature importance, and causality mechanism. In our case, we adopt the feature importance strategy, where a value is attributed to each of the random kernels that describes its importance in the obtained prediction. There are two types of feature attribution methods, model-agnostic and model-specific (Angelov et al. (2021)). Model-agnostic approaches, such as Local Interpretable Model-agnostic Explanations (LIME, Ribeiro et al. (2016)) and SHapley Additive exPlanations (SHAP, Lundberg et al. (2017a)) are designed to explain any model while model-specific approaches take into account the model structure to derive explainability, and they have the advantage of providing more reliable explanation (Z. Li et al. (2022)). Explainability methods can further be classified into global explainability and local explainability. The former is intended to explain the overall model behavior, while the latter explains individual predictions.

In order to achieve explainability with the random kernel transform, we first make adjustments to the feature extraction procedure in the following way:

- l_{kernel} is selected randomly from $\{3, 5, 7, 9, 11\}$ with uniform probability. The added lengths are intended to capture and explain abnormal trends of the subsequences, such as atypical

upward or downward trends.

- We only extract the maximum value of the convolution mv as a feature. This is because, unlike ppv , this feature is straightforward to interpret. To show this, consider the convolution between a subsequence and a convolutional kernel shown in Fig. 3.2. We notice that when the convolutional kernel matches a pattern in the subsequence, which is here a level shift, the convolution output is maximal at this location. Therefore, the mv reflects the maximum similarity between a random filter and the patterns in the subsequence, similar to the shapelet transform. Hence, our assumption is that when detecting an abnormal subsequence, we are able to trace the similarities with the random kernels that made the detector predict the subsequence as abnormal. These random kernels will then be used to explain the abnormal patterns in the subsequence. The technique will be detailed shortly.
- We do not use padding when performing the convolution. This is because we want the maximum value (mv) to reflect the similarity of the random kernel with a pattern that is fully contained in the subsequence, in order to achieve a more accurate explainability.

With these adjustments being made, we propose in this work a simple model-specific local explanation approach that makes use of the random kernels. First, the approach involves estimating the importance of each random kernel in the obtained prediction. For this, we define the impor-

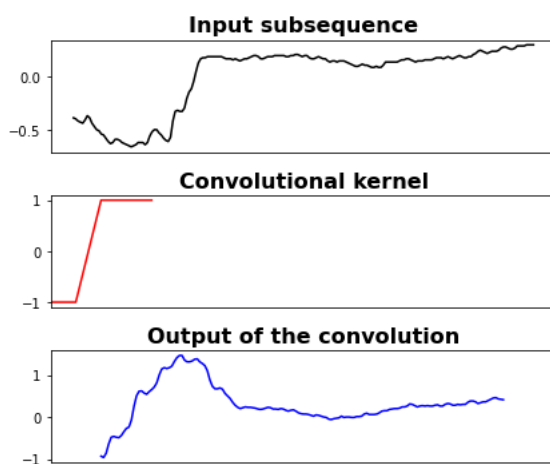


Figure 3.2: An illustration of the convolution between a subsequence and a convolutional kernel.

tance of the features as a constrained point-wise difference between the abnormal observation x' and its nearest neighbor s from the normal training data, as Fig 3.3 shows. Formally, the features' importance (FI) is estimated as follows:

$$FI_i(x) = (x'_i - s_i)_+ = \begin{cases} x'_i - s_i & \text{if } (x'_i - s_i) > 0 \\ 0 & \text{Otherwise} \end{cases} \quad (3.2)$$

where x' is the abnormal observation and s the nearest neighbor of x' in the training data. To understand the assumptions behind Eq. 3.2, first, recall that the maximum value of the convolution that we use as a feature gives the maximum similarity between the random kernel and the shapes contained in the subsequence. Suppose that we use 5 random kernels and that the abnormal subsequence has a feature vector $x' = [0, 0, 2, 8, 9]$, which indicates that it has a relatively high similarity with the 4th and the 5th random kernels. Suppose now that the nearest neighbor of x' from the training data is given by $s = [5, 5, 2, 1, 1]$, indicating that a typical normal subsequence that x' deviates the least from is characterized by similarities with the first two random kernels while having low similarities with the last two. In order to give an informative characterization

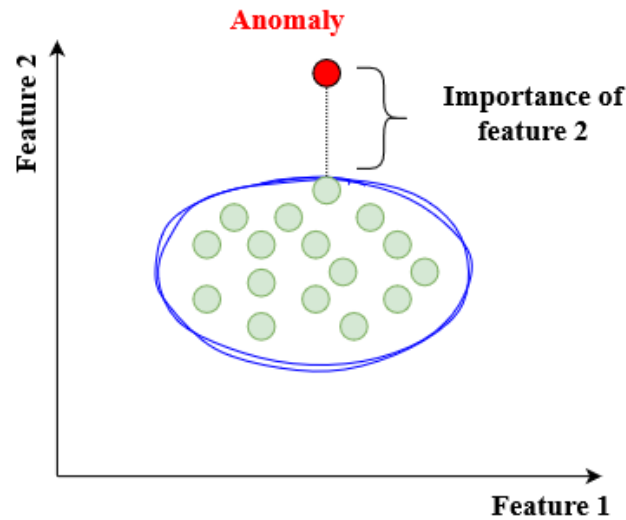


Figure 3.3: An illustration of the feature importance estimation.

and explanation of why x' is anomalous, we should answer the following question: *which shapes are present in the subsequences that made it abnormal?* which we attempt to answer by using Eq. 3.2, that gives the following feature importance vector $FI = [0, 0, 0, 7, 8]$, highlighting that the abnormal subsequence has high similarities with the 4th and 5th random kernels and that it made it abnormal while ignoring the information that the dissimilarity with the first two kernels possibly also made the subsequence abnormal as this might not be informative for the users as they might not be aware of all the normal shapes of the subsequences.

After estimating the contribution of a random kernel to the prediction based on the defined approach, we need to find where in the subsequence the similarities with the most important random kernels are the highest, which is the second part of the explanation that we call the localization L , which indicates the localization of the pattern that makes the subsequence abnormal. For this purpose, we need to find the argument of the maximum value of the convolution $L_i = \text{argmax}(Z_i(x'))$. The final explanation for the abnormal subsequence x' is then a tuple $\{FI_i(x'), L_i(x')\}$ with $i = [1, 2, \dots, k]$ (where k is the number of random kernels), arranged by $FI_i(x')$ in a decreasing order. Appendix E gives the pseudocode of the approach.

It should be kept in mind that this approach has some limitations. It treats every feature individually and does not take into account the possible interaction between features. Moreover, if a large number of random kernels are used in ROCKET, this method may not work effectively. Despite these limitations, the approach gives good results, as we shall see later.

We compare this technique with SHapley Additive exPlanations (SHAP), which is a feature importance, model-agnostic approach for explaining black-box machine learning algorithms based on a game theory approach named Shapley values. To get the contribution ϕ_j of a feature j to the output of an algorithm, it uses the following formula:

$$\phi_j = \sum_{S \subseteq F \setminus j} \frac{|S|!(|F| - |S| - 1)}{|F|!} [f_{S \cup j}(X_{S \cup j}) - f_S(X_S)] \quad (3.3)$$

Where F is the set of all the features, S is a subset of F , X are the input values of the features, and f is the machine learning model. $f_S(X_S)$ indicates that the model f is trained using the subset S of the features F . Eq. 3.3 can be explained as follows: the contribution of the feature j is the

mean of the differences between the predictions of the model using all possible subsets S of F with the presence of the feature j and the predictions of the model trained with the same S without j . The complexity of the brute force calculation of the exact value of ϕ_j increases exponentially with respect to the number of features F . For tree models, Lundberg et al. (2017b) proposed the Tree SHAP algorithm that takes into account the structure of these models in order to compute the Shapley values in polynomial time complexity. We use this algorithm along with the Isolation Forest in our comparative study of explainability.

3.2.3 Approach 2: Dimensionality reduction techniques with ROCKET and OC-SVM

In this second approach, we aim to address the shortcoming of the OC-SVM with distance substitution kernels that is relying on the choice of the dissimilarity measure. We prioritize here accuracy, generalization, and computational efficiency, and we assume that explainability is not needed. For this, we investigate the use of ROCKET along with feature selection and reduction techniques that we present here. Feature selection refers to selecting a subset of the original features that are the most relevant to the problem at hand, while feature reduction consists in transforming the original features by mapping them to a lower dimensional space.

Correlation-based

The correlation-based feature selection that we use in this work consists in discarding highly correlated features and subsequently, the random kernels that generated these features. The assumption is that correlated features hold similar information, whereas we are more interested in features that capture different patterns that would help us detect anomalies more accurately. Formally, the technique involves calculating the Pearson correlation coefficient between each pair of features in the dataset. If the correlation coefficient is higher than a specified threshold, one of the features is removed. The process is repeated until all highly correlated features are removed. We set the correlation threshold at 0.7 in this study.

Principal Component Analysis

Principal Component Analysis is a feature reduction tool that can be used as a pre-processing for supervised and unsupervised problems such as classification and clustering. The feature reduction is performed by keeping only the components that have important eigenvalues. In this work, we keep the components that account for 98% of the total variation.

Lian (2012) argued that for one-class classification, the components with low eigenvalues are the most interesting. The author explained this by the fact that, unlike clustering or classification, in one-class classification, we are not attempting to discriminate between the samples. Instead, we are trying to group them. Hence, the components with low eigenvalues are the ones that exhibit the patterns that are shared by the normal class. We also study in this chapter this form of dimensionality reduction by removing the first components that account for 70% of the total variation, and we call this technique *PCA_OC*.

Inter-Quartile Range

For one-class classification, Lorena et al. (2015) suggested using the Inter Quartile Range (IQR) as a feature selection method. The idea behind this method is that the features with a small IQR are the characteristics of the normal class, similar to the *PCA_OC*, and any deviations from these features can be used to identify anomalies. In our experiments, we retain the features that have an IQR lower or equal to the 0.2 quantile of the IQRs of all the features.

3.3 Results and discussion

In this section, the results of the two approaches are presented. We will begin by presenting the results of the first approach that extracts only the maximum value of the convolution and that is able to provide an explanation of the anomalies while in the second study, we are only interested in the generalizability of the ROCKET to all the welding signal considered in this thesis. For this, we investigate the use of *mv* only, *ppv* only, and both *ppv* and *mv* as features and employ the

dimensionality reduction techniques presented above.

We first detail the experimental methodology followed in this study. At training, k random kernels are generated along with their attributes discussed earlier i.e. length, weights, and dilation. After feature extraction, an OC-SVM model is fitted to the training data represented by the extracted features. The OC-SVM parameter ν is fixed at 10^{-5} as we are only training from normal data.

In the test stage, we first transform the upcoming subsequences using the generated convolutional kernels in the training stage. We then predict if they are normal or abnormal by feeding the extracted features from the convolutions (or a subset of them in the second approach) into the trained OC-SVM model. If the anomaly score is lower than a threshold τ , the subsequence is declared abnormal. The threshold is estimated as in the previous chapter using Eq. 3.4:

$$\tau = \bar{F}(x^{train}) - 3 * \sigma_{F(x^{train})} \quad (3.4)$$

Where $\bar{F}(x^{train})$ is the mean of the anomaly scores obtained from the training data and $\sigma_{F(x^{train})}$ is the standard deviation of these anomaly scores. In the first approach, when a subsequence is abnormal, we follow the explainability approach presented earlier in order to give indications of why it is predicted abnormal. We retain the three most important kernels for the explanation.

In order for the results to be comparable with the ones from the previous chapter, we consider here the same data and the same evaluation procedure, we retain the use of the k -fold technique with $k = 5$. Recall that in this process, the normal subsequences are divided into 5 subsets, and for each iteration, the model is trained using 4 subsets of the normal subsequences, while the 5th subset is combined with the abnormal subsequences to form the test data. We repeat the training and testing 10 times for each of the five subsets, and we report here the F1-score averaged over the 10 runs and the 5 test subsets, along with the average standard deviation in order to quantify the variability of the detection accuracy that is due to the randomness of ROCKET. We consider here the use of 500 random kernels to transform the subsequences unless stated otherwise.

To accurately compare approaches as well as the feature selection and reduction techniques in terms of accuracy in the second approach, we vary the smoothing parameter γ of the RBF kernel

from 10^{-5} to 10^{-2} with a step of 10^{-1} in an attempt to separate the impact of this parameter from the effects of choosing different features and reducing the dimensionality.

3.3.1 Results of the first approach

We present in this section the results of the first approach in terms of detection accuracy and explainability. Table 3.1 gives the F1-scores for all the signals obtained with the OC-SVM using different values for the parameter of the RBF kernel. We can notice from the table that the approach has good accuracy for the considered signals, notably the model with $\gamma = 0.001$ that gives good results across all the signals and outperforms the methods presented in the previous chapters for most of the signals. These first results indicate that ROCKET may be promising as a generic abnormal subsequence detection method. However, we can notice from Table 3.1 that for the subsequences of the orbital signal (orbital 1 and orbital 2 in the table), the standard deviations of the F1-score are high compared to the ones observed for the other signals. This can be explained by the fact that these signals are the most complex, as a consequence, the representation obtained with ROCKET can be complex and highly variable between runs. From the standard deviation of the F1-scores in Table 3.1, we notice that this is notably valid for the second part which is composed of two frequencies, hence the most complex, and for which the variability is the highest. This suggests that despite the good F1-scores obtained, ROCKET for anomaly detection can still benefit from further optimizations in order to reduce the variability of the detection accuracy and improve performance. This can include the extraction of other features from the convolutions and feature selection and reduction that we study in the second approach.

We are interested at this stage in explaining the detected anomalies using the 500 random kernels generated at training. Employing our approach for explainability, we identified the three most

Table 3.1: F1-score for all the signals obtained by the first approach.

Kernel	Circular welding	Orbital 1	Orbital 2	CMT connection	CMT intersection
10^{-5}	$0.807_{\pm 0.0116}$	$0.932_{\pm 0.0166}$	$0.72_{\pm 0.1034}$	$0.99_{\pm 0.0026}$	$0.873_{\pm 0.0162}$
0.0001	$0.901_{\pm 0.0094}$	$0.962_{\pm 0.0142}$	$0.864_{\pm 0.064}$	$0.984_{\pm 0.004}$	$0.92_{\pm 0.0052}$
0.001	$0.952_{\pm 0.01}$	$0.929_{\pm 0.0176}$	$0.913_{\pm 0.0238}$	$0.989_{\pm 0.004}$	$0.924_{\pm 0.0056}$
0.01	$0.0_{\pm 0.0}$	$0.0_{\pm 0.0}$	$0.0_{\pm 0.0}$	$0.0_{\pm 0.0}$	$0.0_{\pm 0.0}$

important random kernels for each abnormal subsequence. To give an illustrative explanation, we plot the abnormal subsequences along with the most important random kernels at their associated localization. Since the convolutions are performed with dilations, the weights of a random kernel are spaced by the amount of the dilation used in the convolution, for example, if the weights of a kernel are $[0,1,1]$ and the convolution is performed using dilation of 5, then the weights will have the timestamps $t_1=L$, $t_2=t_1+5$, $t_3=t_2+5$, where L is the argument of the maximum value in the convolution. Fig. 3.4 shows 4 abnormal subsequences of the circular welding signal, along with the 3 most important kernels for each one shown in blue. We can notice that the random kernels give an accurate indication of the abnormal shapes in the subsequences at their exact location. We notice that when the abnormal shapes are complex, such as in the subsequence in Fig. 3.4 (a), the three convolutional kernels are relatively different, and together they explain the complex abnormal shape whereas in simpler abnormal shapes such as the level shift in 3.4 (c) and 3.4 (d), the three most important kernels are relatively similar as these anomalies can be fully explained by a basic shape.

To further investigate the explainability, we test the approach with the signals of the orbital welding. Fig. 3.5 shows 4 abnormal subsequences of these signals, along with the three most important random kernels. We notice again that the random kernels perfectly capture and explain the abnormal shapes of these subsequences. Moreover, for the subsequences in Fig. 3.5.(b) and Fig. 3.5 (d), we notice that the kernels of length 3, that we added to the possible lengths, perfectly explain that the unusual downward trends that made these subsequences abnormal.

We are interested in exploring the variability of explainability resulting from the random generation of the convolutional kernels. For this purpose, we generate 500 random kernels four times, and for each run, we extract the 3 most important kernels for an abnormal subsequence of the signals of the orbital welding process. Fig. 3.6 shows the three most important kernels obtained from each run. We notice that most of the time, they have a length of three and exhibit significant similarities across runs. Furthermore, even when the kernels are more complex, as is the case with the first two kernels in Fig. 3.6 (d), they still indicate the same part of the subsequence and highlight an anomalous downward trend. These findings suggest that, despite the randomness of the convolutional kernels, reliable explainability can be achieved each time.

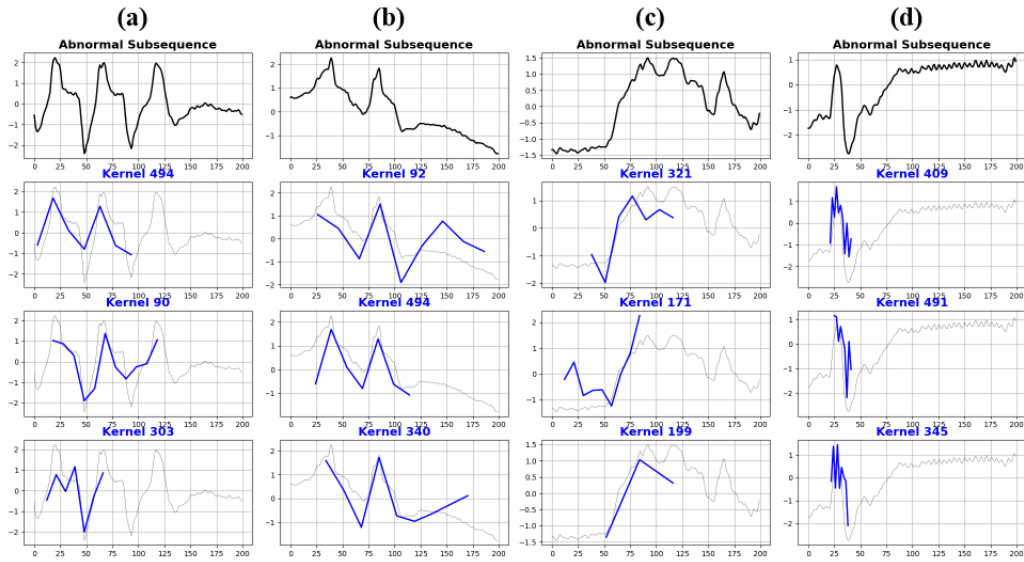


Figure 3.4: Examples of abnormal subsequences of the circular welding signals along with the three most important kernels.

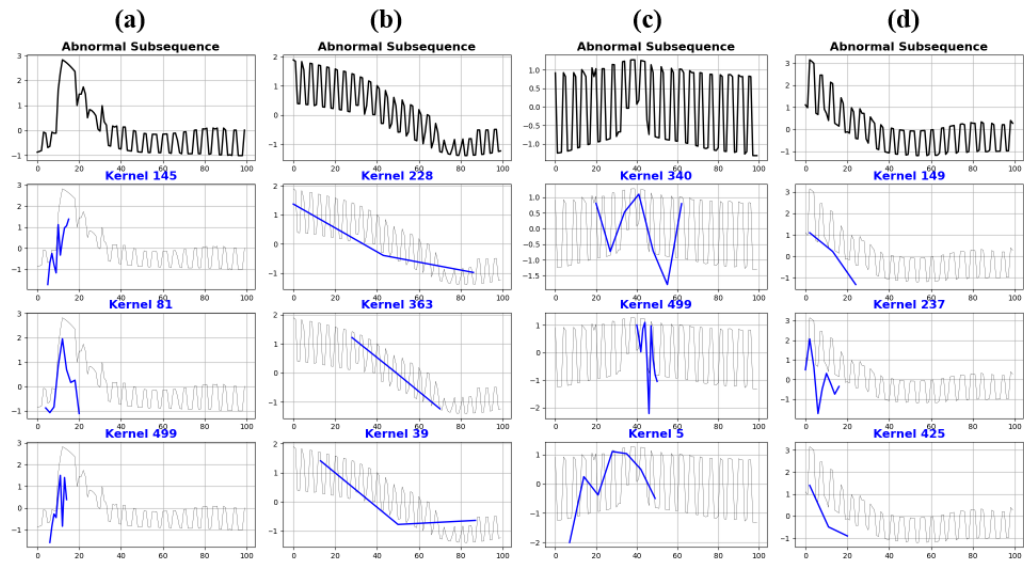


Figure 3.5: Examples of abnormal subsequences of the orbital welding signals along with the three most important kernels.

We would like now to compare our explainability technique with SHAP that we introduced earlier. For this purpose, we trained an IForest model and employed the TreeSHAP algorithm to

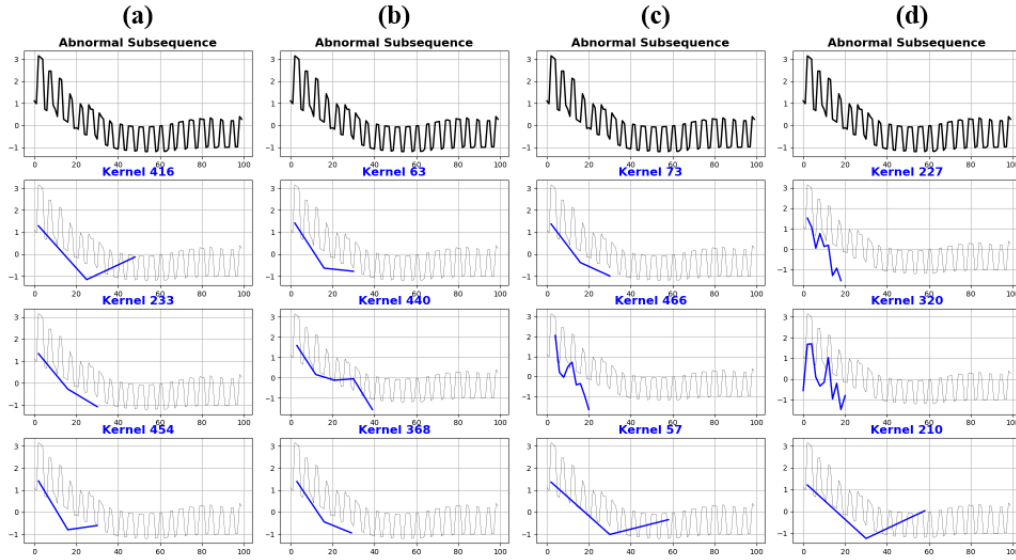


Figure 3.6: The three most important random kernels obtained from 4 different runs.

estimate the features' importance. Fig. 3.7 shows the three most important kernels extracted by our technique and by the TreeSHAP from the same set of random kernels generated at training. We notice again that our technique gives an accurate explanation while the TreeSHAP assigns importance to shapes that do not appear in the subsequence, such as the second most important kernels in the two subsequences. This shows that despite SHAP being theoretically optimal, it might not be very useful in this particular problem of explaining abnormal subsequences using random convolutional kernels, while our simple technique reveals the patterns that characterize the anomalies.

After examining the explanations for various abnormal subsequences, we can deduce that our proposed explainability approach is suitable for explaining anomalous shapelets and anomalous trends. However, although ROCKET and OC-SVM may detect any type of abnormal subsequence, not all of them can be explained by the presented approach. To give an example, we are aware of one specific type of anomaly that cannot be effectively explained by random convolutional kernels, which is observed in the signals of CMT welding and shown in Fig. 3.8 where the oscillations have varying amplitudes over time, which is complex to explain with the basic shapes obtained with the random convolutional kernels.

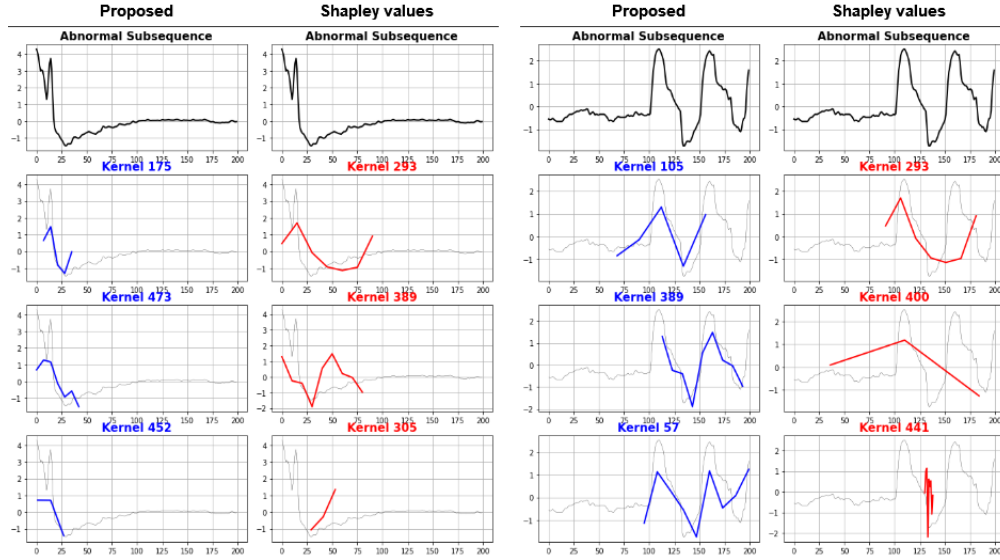


Figure 3.7: The three most important random kernels obtained using our approach (in blue) and those obtained with TreeSHAP (in red).

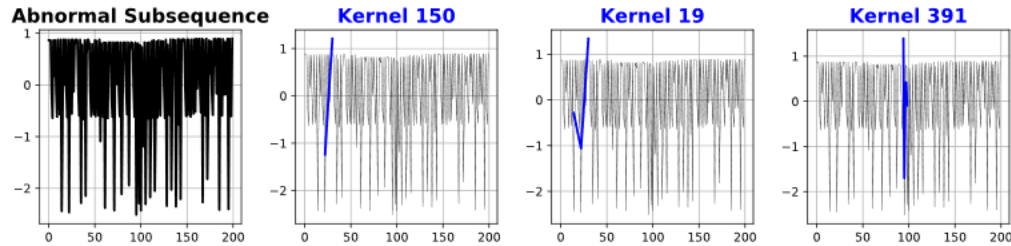


Figure 3.8: An example of an abnormal subsequence from the CMT welding signals that cannot be effectively explained.

In order to study the impact of using a high number of kernels, we generated 5000 kernels at the training stage. Fig. 3.9 shows the important kernels. We notice that the explainability did not deteriorate and is even more accurate here than when using only 500 kernels since there are more shapes to explain the abnormal patterns. This shows that even with this high number of kernels, the proposed technique for characterizing the anomalies can still work effectively. However, with a high number of kernels, finding the nearest neighbor for the features' importance by Eq. 3.2 can become time-consuming. A possible solution for this problem is to compute the feature importance by replacing s in Eq 3.2 with the nearest support vector of the OC-SVM model. We tested this

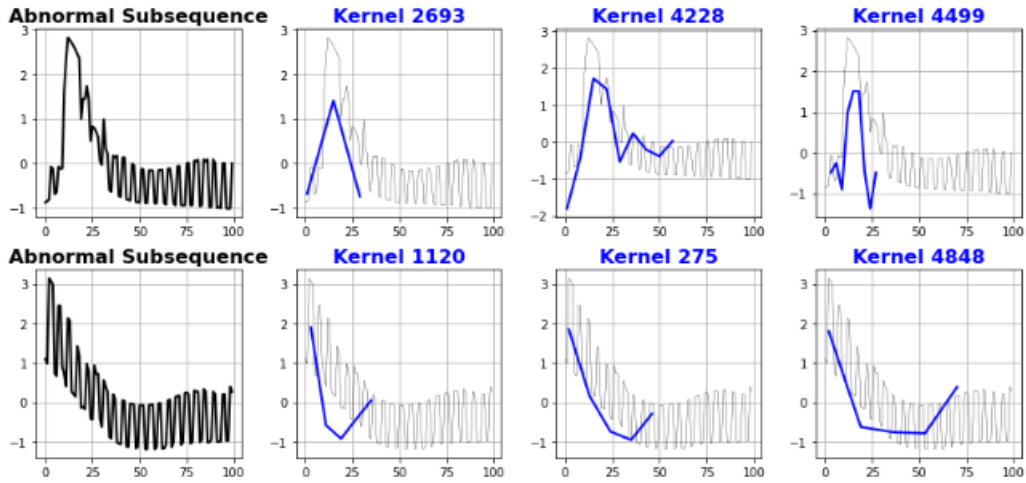


Figure 3.9: The three most important random kernels obtained with a model using 5000 random kernels.

for some abnormal subsequences, and we found that the explainability results are identical to the one obtained by the nearest neighbor in the training set, suggesting that it is possible to use the support vectors for faster estimation of the features' importance.

Another problem that can arise when using a high number of random convolutional kernels is the risk that an important proportion of them will be highly similar, which can increase the computational complexity without adding much information. For this case, the explainability approach can possibly benefit from the feature selection techniques that we study in the next subsection.

3.3.2 Results of the second approach

In this section, we present the results of the second approach that combines the features extracted from the convolutions with random kernels and the use of feature selection and reduction techniques to reduce the dimensionality of the feature vector. The objective of these experiments is to evaluate the feasibility of developing a robust abnormal subsequence model that generalizes well across different signals and that is computationally efficient.

We begin by studying the models combining the mv of the convolutions and the dimensionality

CHAPTER 3. WELDING DEFECT DETECTION USING RANDOM CONVOLUTIONAL KERNEL TRANSFORM

reduction techniques. Table 3.2 gives the F1-scores for the signals of the three welding machines, along with the median value of the number of the retained features for each of the dimensionality reduction methods. We first notice that working with the original features does not always result in the best models. For instance, for the second part of the orbital welding signals (denoted by "orbital 2" in the table), performing any of the dimensionality reduction techniques results in an increase in the F1-score. This is because using these dimensionality reductions simplifies the original representation obtained by ROCKET, which can be very complex for these signals, as discussed earlier.

Regarding feature selection techniques, we notice that the correlation-based technique improves the accuracy for the circular welding signals and for those of the second part of the orbital signals and only retains a low number of dimensions for these signals. However, it has a negative impact on the accuracy for the first part of orbital signals, and it also decreases the accuracy for CMT signals, but to a lesser extent. The IQR technique decreases the accuracy for most of the signals, but it highly increases the accuracy for the "orbital 2" subsequences. Furthermore, both techniques increase the

Table 3.2: The results of the models using only mv in the feature vector.

Feat. selection	γ	Circular	Orbital 1	Orbital 2	CMT connection	CMT intersection
Without feature selection	10^{-5}	0.807 \pm 0.0116	0.932 \pm 0.0166	0.72 \pm 0.1034	0.99 \pm 0.0026	0.873 \pm 0.0162
	0.0001	0.901 \pm 0.0094	0.962 \pm 0.0142	0.864 \pm 0.064	0.984 \pm 0.004	0.92 \pm 0.0052
	0.001	0.952 \pm 0.01	0.929 \pm 0.0176	0.913 \pm 0.0238	0.989 \pm 0.004	0.924 \pm 0.0056
	0.01	0.0 \pm 0.0	0.0 \pm 0.0	0.0 \pm 0.0	0.0 \pm 0.0	0.0 \pm 0.0
Correlation	10^{-5}	0.923 \pm 0.0114	0.871 \pm 0.0204	0.928 \pm 0.044	0.986 \pm 0.0038	0.834 \pm 0.0158
	0.0001	0.912 \pm 0.027	0.877 \pm 0.0252	0.833 \pm 0.0916	0.979 \pm 0.008	0.911 \pm 0.01
	0.001	0.938 \pm 0.021	0.891 \pm 0.0226	0.888 \pm 0.0346	0.986 \pm 0.004	0.914 \pm 0.0086
	0.01	0.96 \pm 0.0138	0.114 \pm 0.2568	0.924 \pm 0.026	0.0 \pm 0.0	0.0 \pm 0.0
Retained		11.0	154.0	18.0	275.0	274.5
IQR	10^{-5}	0.709 \pm 0.0134	0.724 \pm 0.038	0.805 \pm 0.0868	0.981 \pm 0.0032	0.911 \pm 0.0034
	0.0001	0.798 \pm 0.0172	0.867 \pm 0.0234	0.809 \pm 0.078	0.973 \pm 0.0106	0.91 \pm 0.007
	0.001	0.906 \pm 0.0194	0.921 \pm 0.027	0.98 \pm 0.0104	0.983 \pm 0.0044	0.91 \pm 0.0048
	0.01	0.921 \pm 0.0114	0.87 \pm 0.0298	0.909 \pm 0.023	0.982 \pm 0.0078	0.808 \pm 0.1618
Retained		100.0	100.0	100.0	100.0	100.0
PCA	10^{-5}	0.803 \pm 0.012	0.928 \pm 0.0174	0.726 \pm 0.107	0.991 \pm 0.0022	0.868 \pm 0.0158
	0.0001	0.898 \pm 0.01	0.963 \pm 0.0136	0.87 \pm 0.0598	0.987 \pm 0.0034	0.921 \pm 0.0046
	0.001	0.96 \pm 0.009	0.937 \pm 0.017	0.954 \pm 0.0186	0.991 \pm 0.0028	0.924 \pm 0.0062
	0.01	0.0 \pm 0.0	0.0 \pm 0.0	0.0 \pm 0.0	0.0 \pm 0.0	0.0 \pm 0.0
Retained		159.0	256.0	67.0	313.0	318.0
PCA_{OC}	10^{-5}	0.859 \pm 0.0136	0.818 \pm 0.0196	0.836 \pm 0.0512	0.959 \pm 0.0054	0.863 \pm 0.01
	0.0001	0.879 \pm 0.0042	0.805 \pm 0.0258	0.886 \pm 0.037	0.959 \pm 0.0058	0.866 \pm 0.0088
	0.001	0.883 \pm 0.004	0.828 \pm 0.0204	0.992 \pm 0.004	0.967 \pm 0.0074	0.87 \pm 0.0086
	0.01	0.0 \pm 0.0	0.0 \pm 0.0	0.0 \pm 0.0	0.0 \pm 0.0	0.0 \pm 0.0
Retained		498.0	485.0	499.0	476.0	475.5

CHAPTER 3. WELDING DEFECT DETECTION USING RANDOM CONVOLUTIONAL KERNEL TRANSFORM

standard deviation of the F1-scores for most of the signals. Overall, the IQR technique seems to better maintain a good accuracy across all the signals than the approach based on correlation.

We notice that among the considered dimensionality reduction techniques, performing PCA results in the best models in terms of accuracy, and this is for all the signals. Notably, the model using PCA with the RBF parameter of OC-SVM $\gamma = 0.001$ generalizes the best. The *PCA_OC* technique does not offer better accuracy than the classical use of PCA, except for the case of the subsequences "orbital 2". This might be explained by the fact that the features shared between the normal subsequence are possibly also shared with the abnormal subsequences. The technique works well for the subsequences "orbital 2" because, as discussed earlier, these signals are composed of two frequencies, which makes the representation obtained by ROCKET complex. Hence, by dropping the first PCA components with the highest eigenvalues, the representation becomes simpler, and we are able to better model the normal class. Overall, we conclude from Table 3.2 that performing PCA results in the highest F1-scores.

We will now examine models that exclusively use the *ppv* in the feature vector. Table 3.3 gives the

Table 3.3: The results of the models using only *ppv* in the feature vector.

Feature selection	Kernel	Circular welding	Orbital 1	Orbital 2	CMT connection	CMT intersection
Without feature selection	10^{-5}	0.978 ± 0.0066	0.901 ± 0.041	0.933 ± 0.0642	0.952 ± 0.0282	0.765 ± 0.029
	0.0001	0.976 ± 0.0044	0.915 ± 0.0192	0.988 ± 0.0092	0.962 ± 0.0168	0.857 ± 0.0234
	0.001	0.876 ± 0.0056	0.896 ± 0.0222	0.946 ± 0.0372	0.984 ± 0.0058	0.902 ± 0.0204
	0.01	0.0 ± 0.0	0.0 ± 0.0	0.0 ± 0.0	0.0 ± 0.0	0.0 ± 0.0
Correlation	10^{-5}	0.975 ± 0.0062	0.919 ± 0.0266	0.891 ± 0.0224	0.984 ± 0.0074	0.812 ± 0.0364
	0.0001	0.972 ± 0.0048	0.887 ± 0.0338	0.871 ± 0.017	0.967 ± 0.0168	0.876 ± 0.0272
	0.001	0.927 ± 0.0076	0.893 ± 0.0264	0.843 ± 0.0126	0.981 ± 0.007	0.903 ± 0.0206
	0.01	0.477 ± 0.4282	0.0 ± 0.0	0.0 ± 0.0	0.0 ± 0.0	0.0 ± 0.0
Retained		221.5	299.5	131.5	278.0	314.5
IQR	10^{-5}	0.978 ± 0.0068	0.769 ± 0.0718	0.867 ± 0.1028	0.988 ± 0.004	0.893 ± 0.0298
	0.0001	0.974 ± 0.0044	0.754 ± 0.0632	0.961 ± 0.0382	0.973 ± 0.0172	0.885 ± 0.0312
	0.001	0.87 ± 0.0048	0.782 ± 0.0452	0.954 ± 0.0224	0.981 ± 0.0054	0.927 ± 0.0192
	0.01	0.0 ± 0.0	0.866 ± 0.0426	0.0 ± 0.0	0.993 ± 0.0034	0.938 ± 0.0132
Retained		375.0	104.0	329.5	100.0	102.0
PCA	10^{-5}	0.967 ± 0.01	0.895 ± 0.0426	0.894 ± 0.1138	0.94 ± 0.0344	0.752 ± 0.0336
	0.0001	0.98 ± 0.0046	0.919 ± 0.0182	0.961 ± 0.0364	0.953 ± 0.0226	0.843 ± 0.027
	0.001	0.883 ± 0.0066	0.908 ± 0.0214	0.971 ± 0.0204	0.98 ± 0.0072	0.887 ± 0.0204
	0.01	0.0 ± 0.0	0.0 ± 0.0	0.0 ± 0.0	0.0 ± 0.0	0.0 ± 0.0
Retained		190.0	237.5	133.5	253.0	300.0
<i>PCA_OC</i>	10^{-5}	0.951 ± 0.0056	0.89 ± 0.0244	0.839 ± 0.0108	0.985 ± 0.0054	0.928 ± 0.0144
	0.0001	0.945 ± 0.0052	0.899 ± 0.0226	0.833 ± 0.0106	0.982 ± 0.0058	0.927 ± 0.0128
	0.001	0.902 ± 0.0046	0.919 ± 0.021	0.814 ± 0.0092	0.988 ± 0.0046	0.948 ± 0.0078
	0.01	0.0 ± 0.0	0.0 ± 0.0	0.0 ± 0.0	0.0 ± 0.0	0.0 ± 0.0
Retained		487.0	488.0	497.0	488.0	479.0

F1-scores and the number of the retained dimensions of each dimensionality reduction technique. We notice that without feature selection, using *ppv* only results in higher accuracy for the circular welding signals and those of the "orbital 2" than when using the *mv* but lower F1-scores are observed for the remaining signals. The correlation-based dimensionality reduction preserves the accuracy obtained with the whole set of features except for "orbital 2" subsequences, while the IQR improves the accuracy for the CMT signals but decreases it for the orbital signals. We note that IQR retains more than 100 dimensions most of the time, this is because there can be a high number of dimensions where the PPV has zero variance and which are included in the retained features. Similarly, The *PCA_OC* also enhances the accuracy for the CMT signals but retains a large number of features. Regarding PCA, we notice that it preserves the same accuracy obtained with the original features. In summary, using only the *ppv* does not offer better accuracy for all the signals compared to when using *mv*.

Table 3.4 presents the results of the models that extract both *mv* and *ppv* from convolutions with 500 convolutional kernels. It is observed that the accuracy is higher when both features are used in comparison to using each feature separately. One noteworthy result is that the model without feature selection using the *rbf* parameter $\gamma = 0.0001$ generated F1-scores that are comparable to the ones obtained using OC-SVM with distance substitution kernels. Furthermore, it outperforms the techniques employed in the comparative study in the previous chapter for most of the signals. This indicates that the ROCKET with OC-SVM could serve as a general method for identifying abnormal subsequences when extracting both *mv* and *ppv*. As for the models that use dimensionality reduction, the best accuracy is obtained using PCA. Its F1-scores are very comparable to the ones produced with the original features, with significantly fewer dimensions. This finding confirms the superiority of PCA over other dimensionality reduction methods that were considered in this study.

In summary, based on these findings, it can be concluded that using ROCKET is promising as a generic method for abnormal subsequence detection. To further investigate the generalizability of the approach, we test it on an electrocardiogram signal (Keogh, Taposh, et al. (2021)) and a signal acquired from Mars curiosity rover (Hundman et al. (2018)) in Appendix F. Moreover, we conclude that extracting both *mv* and *ppv* leads to the highest accuracy compared to when using only *mv* or only *ppv*. Additionally, the results suggest that PCA is the most effective as it results in the highest F1-scores compared to the other dimensionality reduction techniques. However, the use of

CHAPTER 3. WELDING DEFECT DETECTION USING RANDOM CONVOLUTIONAL KERNEL TRANSFORM

Table 3.4: The results of the models using both mv and ppv in the feature vector.

Feature selection	Kernel	Circular welding	Orbital 1	Orbital 2	CMT connection	CMT intersection
Without feature selection	10^{-5}	$0.957_{\pm 0.0114}$	$0.967_{\pm 0.0252}$	$0.945_{\pm 0.0352}$	$0.994_{\pm 0.003}$	$0.91_{\pm 0.0318}$
	0.0001	$0.976_{\pm 0.0038}$	$0.953_{\pm 0.013}$	$0.994_{\pm 0.0052}$	$0.987_{\pm 0.0034}$	$0.942_{\pm 0.0062}$
	0.001	$0.0_{\pm 0.0}$	$0.919_{\pm 0.0138}$	$0.892_{\pm 0.0268}$	$0.993_{\pm 0.003}$	$0.946_{\pm 0.0094}$
	0.01	$0.0_{\pm 0.0}$	$0.0_{\pm 0.0}$	$0.0_{\pm 0.0}$	$0.0_{\pm 0.0}$	$0.0_{\pm 0.0}$
Correlation	10^{-5}	$0.975_{\pm 0.006}$	$0.915_{\pm 0.0234}$	$0.882_{\pm 0.02}$	$0.989_{\pm 0.0028}$	$0.84_{\pm 0.0168}$
	0.0001	$0.971_{\pm 0.0058}$	$0.889_{\pm 0.0272}$	$0.867_{\pm 0.0142}$	$0.983_{\pm 0.0048}$	$0.934_{\pm 0.0114}$
	0.001	$0.926_{\pm 0.0074}$	$0.904_{\pm 0.0204}$	$0.84_{\pm 0.011}$	$0.989_{\pm 0.0034}$	$0.945_{\pm 0.0072}$
	0.01	$0.283_{\pm 0.3852}$	$0.0_{\pm 0.0}$	$0.0_{\pm 0.0}$	$0.0_{\pm 0.0}$	$0.0_{\pm 0.0}$
Retained		224.5	441.0	143.0	537.0	573.0
IQR	10^{-5}	$0.944_{\pm 0.0162}$	$0.888_{\pm 0.0272}$	$0.834_{\pm 0.1338}$	$0.993_{\pm 0.0036}$	$0.821_{\pm 0.0316}$
	0.0001	$0.971_{\pm 0.0058}$	$0.883_{\pm 0.0418}$	$0.969_{\pm 0.0388}$	$0.974_{\pm 0.0136}$	$0.912_{\pm 0.0184}$
	0.001	$0.913_{\pm 0.0096}$	$0.889_{\pm 0.031}$	$0.955_{\pm 0.0184}$	$0.989_{\pm 0.0038}$	$0.928_{\pm 0.016}$
	0.01	$0.0_{\pm 0.0}$	$0.018_{\pm 0.054}$	$0.0_{\pm 0.0}$	$0.0_{\pm 0.0}$	$0.0_{\pm 0.0}$
Retained		473.5	206.0	430.0	200.0	202.0
PCA	10^{-5}	$0.945_{\pm 0.0132}$	$0.966_{\pm 0.0256}$	$0.931_{\pm 0.0462}$	$0.995_{\pm 0.0036}$	$0.9_{\pm 0.0374}$
	0.0001	$0.978_{\pm 0.004}$	$0.961_{\pm 0.0122}$	$0.994_{\pm 0.0056}$	$0.988_{\pm 0.0028}$	$0.935_{\pm 0.007}$
	0.001	$0.0_{\pm 0.0}$	$0.933_{\pm 0.0124}$	$0.938_{\pm 0.0184}$	$0.994_{\pm 0.0026}$	$0.927_{\pm 0.0098}$
	0.01	$0.0_{\pm 0.0}$	$0.0_{\pm 0.0}$	$0.0_{\pm 0.0}$	$0.0_{\pm 0.0}$	$0.0_{\pm 0.0}$
Retained		305.0	436.5	162.0	466.0	526.0
PCA_{OC}	10^{-5}	$0.952_{\pm 0.0052}$	$0.903_{\pm 0.0172}$	$0.868_{\pm 0.0144}$	$0.985_{\pm 0.004}$	$0.917_{\pm 0.0104}$
	0.0001	$0.94_{\pm 0.0048}$	$0.909_{\pm 0.0168}$	$0.863_{\pm 0.0104}$	$0.988_{\pm 0.005}$	$0.93_{\pm 0.0084}$
	0.001	$0.886_{\pm 0.0046}$	$0.955_{\pm 0.012}$	$0.893_{\pm 0.0104}$	$0.991_{\pm 0.0028}$	$0.931_{\pm 0.0084}$
	0.01	$0.0_{\pm 0.0}$	$0.0_{\pm 0.0}$	$0.0_{\pm 0.0}$	$0.0_{\pm 0.0}$	$0.0_{\pm 0.0}$
Retained		994.0	983.0	998.0	978.0	970.0

PCA does not significantly reduce the computation time since the whole set of kernels is needed to perform the convolutions. For 500 kernels, the approach has a runtime that is comparable to the one of the autoencoder from the previous chapter.

We would like now to study how accuracy changes with respect to the number of random kernels used. To achieve this, we use 50, 200, 500, and 700 kernels and extract both ppv and mv . We evaluate the accuracy of the models using the original features as well as the models that use PCA since we have observed that it leads to the highest level of accuracy. Table 3.5 gives the results of these models. We first notice that with only 50 kernels, we obtain models that outperform the approaches considered in the comparative study of the previous chapter for most of the signals. We also notice that increasing the number of kernels results in an increase in the F1-scores and a decrease in the standard deviations for most of the signals. We remark that the orbital welding signals are the ones that benefit the most from using more kernels. For the other signals, we do not notice a significant improvement in the accuracy above 200 kernels. As in the classical use of ROCKET for time series classification, we can conclude that generally, using more kernels results in better accuracy for the problem of abnormal subsequence detection.

CHAPTER 3. WELDING DEFECT DETECTION USING RANDOM CONVOLUTIONAL
KERNEL TRANSFORM

Table 3.5: The results of the models as a function of the number of random kernels used to transform the subsequences.

N kernels	Features	γ	Circular welding	Orbital 1	Orbital 2	CMT connection	CMT intersection
50	Original	10^{-5}	0.912 ± 0.0282	0.877 ± 0.03	0.704 ± 0.1738	0.991 ± 0.0062	0.823 ± 0.0302
		0.0001	0.915 ± 0.0254	0.931 ± 0.036	0.842 ± 0.1176	0.988 ± 0.0084	0.867 ± 0.05
		0.001	0.963 ± 0.0124	0.931 ± 0.028	0.938 ± 0.0738	0.987 ± 0.0042	0.925 ± 0.0184
		0.01	0.64 ± 0.327	0.926 ± 0.02	0.893 ± 0.0362	0.993 ± 0.0038	0.926 ± 0.0168
	PCA	10^{-5}	0.91 ± 0.0288	0.874 ± 0.0312	0.637 ± 0.1912	0.99 ± 0.0066	0.819 ± 0.0316
		0.0001	0.912 ± 0.0266	0.931 ± 0.0358	0.795 ± 0.1458	0.988 ± 0.009	0.864 ± 0.0516
		0.001	0.964 ± 0.0124	0.93 ± 0.0292	0.904 ± 0.1046	0.986 ± 0.005	0.922 ± 0.0174
		0.01	0.696 ± 0.2944	0.929 ± 0.0226	0.911 ± 0.0378	0.993 ± 0.004	0.92 ± 0.0188
Retained		58.5	73.0	37.0	77.0	80.0	
200	Original	10^{-5}	0.938 ± 0.0152	0.907 ± 0.0254	0.862 ± 0.106	0.995 ± 0.0024	0.828 ± 0.0176
		0.0001	0.972 ± 0.0094	0.95 ± 0.0184	0.978 ± 0.0246	0.985 ± 0.0034	0.929 ± 0.0128
		0.001	0.921 ± 0.0094	0.935 ± 0.0186	0.958 ± 0.0186	0.99 ± 0.0034	0.942 ± 0.0104
		0.01	0.0 ± 0.0	0.0 ± 0.0	0.0 ± 0.0	0.0 ± 0.0	0.0 ± 0.0
	PCA	10^{-5}	0.93 ± 0.0164	0.907 ± 0.0254	0.782 ± 0.1572	0.995 ± 0.0024	0.821 ± 0.019
		0.0001	0.97 ± 0.01	0.954 ± 0.0188	0.945 ± 0.0644	0.986 ± 0.0036	0.925 ± 0.0148
		0.001	0.927 ± 0.0084	0.944 ± 0.0178	0.978 ± 0.0118	0.992 ± 0.0034	0.935 ± 0.0084
		0.01	0.0 ± 0.0	0.0 ± 0.0	0.0 ± 0.0	0.0 ± 0.0	0.0 ± 0.0
Retained		174.5	225.0	97.0	249.0	272.0	
500	Original	10^{-5}	0.957 ± 0.0114	0.967 ± 0.0252	0.945 ± 0.0352	0.994 ± 0.003	0.91 ± 0.0318
		0.0001	0.976 ± 0.0038	0.953 ± 0.013	0.994 ± 0.0052	0.987 ± 0.0034	0.942 ± 0.0062
		0.001	0.0 ± 0.0	0.919 ± 0.0138	0.892 ± 0.0268	0.993 ± 0.003	0.946 ± 0.0094
		0.01	0.0 ± 0.0	0.0 ± 0.0	0.0 ± 0.0	0.0 ± 0.0	0.0 ± 0.0
	PCA	10^{-5}	0.945 ± 0.0132	0.966 ± 0.0256	0.931 ± 0.0462	0.995 ± 0.0036	0.9 ± 0.0374
		0.0001	0.978 ± 0.004	0.961 ± 0.0122	0.994 ± 0.0056	0.988 ± 0.0028	0.935 ± 0.007
		0.001	0.0 ± 0.0	0.933 ± 0.0124	0.938 ± 0.0184	0.994 ± 0.0026	0.927 ± 0.0098
		0.01	0.0 ± 0.0	0.0 ± 0.0	0.0 ± 0.0	0.0 ± 0.0	0.0 ± 0.0
Retained		305.0	436.5	162.0	466.0	526.0	
700	Original	10^{-5}	0.964 ± 0.0112	0.956 ± 0.0258	0.968 ± 0.0286	0.974 ± 0.0062	0.93 ± 0.0036
		0.0001	0.973 ± 0.005	0.947 ± 0.0184	0.991 ± 0.0074	0.988 ± 0.0028	0.944 ± 0.0066
		0.001	0.0 ± 0.0	0.933 ± 0.014	0.883 ± 0.0262	0.995 ± 0.0024	0.895 ± 0.0154
		0.01	0.0 ± 0.0	0.0 ± 0.0	0.0 ± 0.0	0.0 ± 0.0	0.0 ± 0.0
	PCA	10^{-5}	0.949 ± 0.011	0.961 ± 0.0252	0.953 ± 0.0312	0.977 ± 0.0066	0.927 ± 0.004
		0.0001	0.978 ± 0.0044	0.959 ± 0.0166	0.996 ± 0.0046	0.99 ± 0.0034	0.938 ± 0.0054
		0.001	0.0 ± 0.0	0.943 ± 0.013	0.958 ± 0.0154	0.992 ± 0.004	0.872 ± 0.0152
		0.01	0.0 ± 0.0	0.0 ± 0.0	0.0 ± 0.0	0.0 ± 0.0	0.0 ± 0.0
Retained		357.0	540.0	188.0	553.0	634.0	

In the problem of abnormal subsequence detection, it is assumed that the moving window used to extract subsequences has approximately the same length as the anomalies. This means that the subsequences should be categorized based on their global shape, which suggests that using ROCKET for this problem may work better if the convolutions are performed with high dilation values in order to detect abnormal subsequences based on their overall shape. To test this, we modified the sampling distribution of the dilations $d=2^x$ from $x \sim U(0, A)$, where $A = \log_2 \frac{l_{input}-1}{l_{kernel}-1}$, to $x \sim U(\frac{1}{2} \times A, A)$ and we used only 50 random kernels in the transform in order to investigate if there is a significant improvement in the accuracy. Table 3.6 gives the obtained results. We can

CHAPTER 3. WELDING DEFECT DETECTION USING RANDOM CONVOLUTIONAL KERNEL TRANSFORM

Table 3.6: Results of the models using 50 random kernels with only high dilation values.

Feature selection	Kernel	Circular welding	Orbital 1	Orbital 2	CMT connection	CMT intersection
Without feature selection	1e-05	0.902 $_{+/-0.0214}$	0.898 $_{+/-0.0284}$	0.839 $_{+/-0.1214}$	0.142 $_{+/-0.1028}$	0.651 $_{+/-0.0264}$
	0.0001	0.937 $_{+/-0.0206}$	0.926 $_{+/-0.0332}$	0.918 $_{+/-0.0644}$	0.866 $_{+/-0.1138}$	0.806 $_{+/-0.0252}$
	0.001	0.975 $_{+/-0.006}$	0.93 $_{+/-0.022}$	0.988 $_{+/-0.0136}$	0.916 $_{+/-0.0558}$	0.868 $_{+/-0.0206}$
	0.01	0.813 $_{+/-0.3144}$	0.921 $_{+/-0.0212}$	0.915 $_{+/-0.0292}$	0.919 $_{+/-0.0582}$	0.878 $_{+/-0.0186}$
PCA	1e-05	0.897 $_{+/-0.0248}$	0.897 $_{+/-0.0284}$	0.785 $_{+/-0.1392}$	0.135 $_{+/-0.1026}$	0.645 $_{+/-0.0268}$
	0.0001	0.932 $_{+/-0.0208}$	0.929 $_{+/-0.0352}$	0.884 $_{+/-0.0854}$	0.858 $_{+/-0.1194}$	0.802 $_{+/-0.0256}$
	0.001	0.976 $_{+/-0.0062}$	0.928 $_{+/-0.0224}$	0.979 $_{+/-0.0254}$	0.9 $_{+/-0.0684}$	0.864 $_{+/-0.0214}$
	0.01	0.852 $_{+/-0.2492}$	0.923 $_{+/-0.018}$	0.936 $_{+/-0.029}$	0.901 $_{+/-0.0554}$	0.873 $_{+/-0.02}$
Retained		58.0	67.0	33.0	64.5	68.0

notice that improvements are obtained for the signals of the circular welding and the "orbital 2" compared to the models using 50 kernels from Table 3.5. However, we notice that the performance of the models for the CMT welding signals is worse here. After investigation, we found that using high values of dilations results in decreasing the detection accuracy for two main reasons: when the anomaly has a shorter length than the length of the subsequence, and when there are anomalies that cannot be detected by their global shape. An example of this latter is the abnormal subsequence in Fig. 3.8 that may not be effectively detected using random kernels with high dilation values. In conclusion, if abnormal subsequences can be detected from their overall shape, using high dilation values may lead to increased accuracy and may eliminate the need for a large number of random kernels. Another interesting conclusion that we make from this study is that ROCKET allows the detection of anomalies having variable length since there are variable kernel lengths and dilations and the features extracted from them will have the same weight in the final prediction. More formally, with a sufficient number of random kernels, we expect the approach to detect anomalies whose lengths range from the minimum possible length of the random kernels (3 in our case) to the length of the subsequence. This makes the approach less sensitive to the selection of the size of the moving window used to extract the subsequences from the time series, which is an important advantage as it can be a difficult task to select the optimal value of this parameter. This is further shown in Appendix F.

The study conducted in this chapter shows that ROCKET can be effective for the problem of abnormal subsequence detection in different types of signals. In summary, the findings of all the above results are as follows:

- Extracting both mv and ppv results in better accuracy than when using each of the two

features separately.

- The best dimensionality reduction technique in terms of preserving accuracy across different signals is the PCA.
- Generally, the higher the number of kernels used in the transform, the higher the accuracy.
- If the abnormal subsequences can be detected based on their global shape, discarding low values of dilations can result in an increase in the accuracy and may eliminate the need for a high number of random convolutional kernels.
- ROCKET allows detecting abnormal patterns of different lengths in the subsequence.

In addition to the study presented here, we also investigated in Appendix G the use of ROCKET for unsupervised welding defect diagnosis, with the aim of developing a framework based on ROCKET for both defect detection and unsupervised diagnosis.

3.4 Conclusion

The current chapter addressed the limitations of OC-SVM with distance substitution kernels, specifically the need to select an appropriate dissimilarity measure and the inability to provide information on the anomalies detected. To overcome these limitations, we proposed in this chapter two approaches based on the random convolutional kernel transform.

The first approach aims to integrate explainability in anomaly detection. It involves extracting the maximum values of the convolutions and using them as input vectors for an OC-SVM model. When an abnormal subsequence is detected, an importance value is assigned to each random kernel to reveal the anomalous patterns. The most important kernels can then be used to explain the abnormal patterns in the subsequence. The approach has proven effective in explaining welding defects that appear as abnormal shapelets and trends in the voltage signal. Additionally, it has been found that the explainability approach works well even when a large number of convolutional kernels are employed. Furthermore, despite the randomness of ROCKET, the results showed that the explanations provided remain consistent across different runs.

In the second approach, we studied the combination of ROCKET with dimensionality reduction techniques with the aim of investigating the use of this combination as a generic and efficient method for abnormal time series subsequence detection. The results showed that extracting both the ppv and mv from the convolutions with random kernels is promising as a generic representation of the subsequences. Moreover, it was found that the best dimensionality reduction technique in terms of preserving accuracy is the PCA. Experiments also revealed that when the abnormal subsequences should be detected based on their global shape, discarding low dilation values can result in increasing the accuracy while avoiding the need for a large number of random convolutional kernels. For both approaches, we also found that ROCKET allows the detection of anomalies of different lengths in the subsequences, which is an important advantage compared to most of the approaches that are sensitive to the length of the subsequence.

Both approaches have some limitations. As seen from the results, the first approach cannot be used to explain any type of abnormal subsequences, there exist anomalies that cannot be explained by basic shapes. Moreover, a relatively large number of random kernels are needed to obtain good explainability, which could result in relatively high computational complexity. As for the second approach, performing PCA does not enhance the computational efficiency, since the convolutions with the whole set of random kernels generated at training will be still needed.

In terms of future research, there are several possible directions that could be pursued. One interesting subject would be to explore alternative feature selection techniques and anomaly detectors to further improve the accuracy and decrease the computational complexity of the second approach. Another promising area for investigation would involve the study of ensemble methods in order to improve the accuracy and possibly minimize the number of random kernels needed to perform the transform. Finally, it would be interesting to study the extension of the proposed approaches to multivariate signals.

This chapter marks the end of our research work on welding defect detection through welding electrical signals. In the next Chapter, we address the problem of identifying defects from weld images using computer vision techniques.

Chapter 4

Computer vision-based welding defect detection

Contents

4.1	Introduction	126
4.2	Literature review on computer vision-based defect detection	128
4.2.1	Supervised defect detection	128
4.2.2	Unsupervised defect detection	131
4.3	Methods and materials	132
4.3.1	You Only Look Once v3 network	133
4.3.2	Evaluation metric	137
4.3.3	Image acquisition system	138
4.4	Results and discussion	139
4.5	Conclusion	144

4.1 Introduction

This chapter addresses the subject of detecting welding defects from weld images. The necessity for a computer vision system for welding defect detection arises because there are welding machines that are not equipped with signal acquisition systems. Installing the appropriate sensors and studying the signals that they capture can be a time-consuming task. On the other hand, working with weld images may be more straightforward for the problem of post-welding defect detection. Hence, our objective here is to develop a computer vision system able to recognize defects in an orbital GTAW process similar to the one studied in the previous chapters, which consists in joining two connection parts to a stainless steel tube that we call here the higher and the lower connection parts. There are multiple types of tubes, characterized by their diameter and the distance between the locations of the two connection parts. We are interested in the orbital welding of tubes because the defects in this process can have a very small size. As a consequence, human visual inspection has a high rate of missed detection, which results in defective tubes being used to produce non-conforming hot water tanks.

The most critical anomalies in this process are burn-through and incomplete welding. We define two types of burn-through, characterized by their size, as shown in Fig. 4.1. The small ones are mostly found on the higher connection part weld, while the large ones occur mostly on the welds of the lower connection part. In addition to the size, what differentiates the two types of burn-through is that the first is shallow and appears only on the welding seam, while the second breaks through the tube. The burn-through can be caused by geometrical imperfections of the parts, while incomplete welding is due to errors in the welding machine. If these defects are not detected at this stage, the anomalous tubes will be used in the next processes, producing a non-conforming final product that will be discarded, which causes a very high scrap cost.

The field of computer vision has undergone significant advancements in recent years, which can be mostly attributed to the emergence of sophisticated deep learning architectures. This has led to the development of more advanced algorithms that have greatly improved performance for various vision tasks, namely image classification, object detection, and segmentation. This has given rise to applications in various fields, such as in autonomous driving, medical imaging, and robotics.

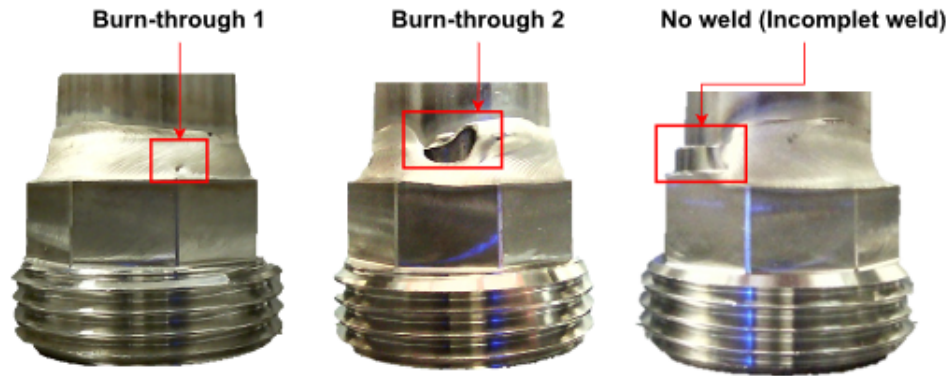


Figure 4.1: Types of the orbital welding defects.

However, accurate welding defect detection from weld images is still a challenging task due to the intricate nature of weld defects (Z. Zhang, Wen, et al. (2019)) as well as their small size. Additionally, it can be difficult to distinguish between an image of a defect-free weld and an image of a non-conforming weld due to the subtle differences between the two. The objective of this chapter is to study the applicability of computer vision for the problem of welding defect detection, with the aim of developing a system that can accurately and efficiently detect defects in weld images. We study the feasibility of developing such a system that is intended to be used as a part of tube welding production and must then satisfy the following requirements:

- The system must detect welding defects with high accuracy and fast inference in order to ensure that the production process is not disrupted.
- The system must localize the defect in the weld.
- The system must require minimal effort to operate.

The chapter is organized as follows: in section 4.2, we review research works that deal with defect detection based on computer vision. In section 4.3 we present the methods and materials. Section 4.4 presents and discusses the results of the developed model for defect detection from weld images, and we finish the chapter with conclusions and future works.

4.2 Literature review on computer vision-based defect detection

The recent advances in computer vision and sensor technology have given rise to applications across various fields ranging from autonomous vehicles, to medical diagnosis and industrial monitoring. We review here research works using computer vision for defect detection, with an emphasis on the welding domain. We review works from the most used concepts for supervised defect detection from images, which we can group into four major concepts: Classical image processing, classification, object detection, and segmentation using deep neural networks. Additionally, we review the recent works addressing the problem of unsupervised anomaly segmentation, where only defect-free images are available at the training.

4.2.1 Supervised defect detection

Classical image processing

In classical image processing methods for defect detection, meaningful features are extracted from the images, based on which defects are detected and classified. Shumin et al. (2011) proposed a method for fabric defect detection using Histogram of Oriented Gradients to extract features from images. SVM classifier with Adaboost are trained on the retrieved features and tested to identify defects in image blocks obtained by a non-overlapping window. Valavanis et al. (2010) extracted multiple geometric and texture features from X-ray images of welds and compared SVM, ANN, and k -NN for the classification of images into 7 classes: defect-free, wormhole, linear slag, porosity, gas pores, lack of fusion and crack. Sun et al. (2019) proposed a method for welding defect detection based on background subtraction. The background is considered to be the good weld seam, whereas the defects are treated as the foreground. To that end, they used a Gaussian Mixture Model with two components. To detect the type of the defect in the foreground, they extracted features such as brightness and gray values and used thresholding to categorize the defects into weld fusion, weld perforation, and cold solder joint. Malarvel et al. (2021) extracted 8 geometrical and 2 texture

features and employed a two-level classification procedure. In the first level, a binary SVM model predicts if the defect is circular or rectangular, then the defect is classified by a multi-class SVM into one of the 3 classes defined for each defect shape. Before the classification, preprocessing including denoising and segmentation is performed on the x-ray images.

Deep neural networks for image classification

Convolutional neural networks (CNN) are a very efficient type of neural networks in image-related tasks such as image classification and object detection due to their ability to automatically learn the most representative features. They have been effectively used for welding defect detection in several works. For instance, Khumaidi et al. (2017) proposed a Convolutional Neural Network composed of 2 convolutional layers to classify weld seam images into good, over-spatter, porosity, and undercut. Xia et al. (2020) trained a model based on the ResNet18 architecture to classify molten pool images during welding in order to detect undercut, incomplete penetration, burn-through, and misalignment. Kumaresan et al. (2021) employed transfer learning to classify weld x-ray images into 14 classes. Features extracted from pre-trained VGG16 and ResNet50 architectures are used to experiment with SVM, logistic regression, and random forest models. The SVM with features obtained from ResNet50 was found to be the most accurate.

To detect misalignment between the pieces at the pre-welding stage, Cruz et al. (2021) developed an ensemble of 5 CNNs and used an evolutionary algorithm to optimize the architecture of the networks and their hyperparameters that include the number and the size of convolutional filters, the size of the pooling and the dropout rate. Perri et al. (2023) proposed a new CNN architecture named WeldNet inspired by the famous Squeezenet (Iandola et al. (2016)) from which they borrowed the fire modules. The CNN was used to classify weld grayscale X-ray images to identify lack of penetration, cracks, and porosity. El Hachem et al. (2021) employed the MobileNet model, known for its lightweight and low latency, to detect defective weld seams in the automotive industry. Z. Zhang, Wen, et al. (2019) developed a CNN composed of 4 convolutional layers to detect burn-through and lack of penetration.

Deep neural networks for object detection

For some subjects where the location of faults in the image is needed, a simple classification of images might not be suitable. Therefore, other works employ the object detection concept for defect detection and localization. The neural networks in this case produce two predictions, a bounding box and the class of the object inside the bounding box. There are two types of this kind of neural network, region-based and regression-based. The difference between them is the method of the bounding box prediction. The first type is two-stage detectors, the purpose of the first stage is to extract the region with a high probability of containing an object from the target classes while the second classifies the extracted object. The regression-based networks treat the problem of bounding box prediction as a regression problem, where the goal is to predict the coordinates of the box. Because of the high number of layers of object detectors, they are almost always trained with techniques like transfer learning and data augmentation.

Wen-ming et al. (2019) use Faster R-CNN, a region-based object detector, to detect 7 welding defects from x-ray images. The authors adapted the feature extractor to be able to operate with grayscale images and obtained an accuracy of 58.6%. K. Zhang et al. (2021) Also developed a Faster R-CNN where the feature extractor is replaced by the ResNet-101 architecture in order to improve the detection of connectors weld in electronic products. The model had a final accuracy of 94%. Changhong Chen et al. (2022) also proposed multiple improvements to Faster R-CNN, such as combining ResNet-50 with Feature Pyramid Networks as a feature extractor and the use of K-Means to propose new anchor boxes. The model was tested on 450 images with 5 weld classes and a global accuracy of 93.72% was reported.

Regression-based were also used in the problem of welding defect detection. Zuo et al. (2021) trained a regression-based model named You Only Look Once v3 (YOLO v3) to detect 4 types of robotic welding defects. The authors reported an accuracy of 75.5%. However, they noted that the accuracy decreased in real conditions to 71% because of the complex lightening conditions, as argued by the authors. M. Liu et al. (2021) proposed a modification of the YOLO network for weld defect detection in X-ray images by introducing modules with parameter-free units in order to reduce the number of learnable parameters in the network.

Deep neural networks for segmentation

Some works are interested not only in the localization of the defects with bounding boxes but also to obtain a mask of every pixel in the image that forms the defect. This can be seen as object detection at the pixel level. The segmentation can serve for further analysis of the defects, particularly for measurement. Kim et al. (2022) developed a Mask-RCNN model for the segmentation of cracks from thermal weld images and used medial axis transform to measure the length and the width of the cracks. Under the keyhole TIG (K-TIG) welding, which is a variant of TIG welding that works by allowing the electric arc to penetrate in the lower surface of the piece, Y. Chen et al. (2021) Trained a Mask-RCNN model to segment the keyhole entrance after which they post-process the mask to obtain its center. The deviation between the keyhole center and the weld center line is measured in order to detect welding deviation, which is the aim of their study.

4.2.2 Unsupervised defect detection

Recently, there has been a growing interest in the unsupervised defect detection in images, especially after the publishing of an open access dataset named MVTEC by Bergmann, Fauser, et al. (2019) that regroup real-world images of industrial pieces for which the goal is to develop models for anomaly segmentation where only defect-free images are available at training. There are two main categories of approaches that address this problem: reconstruction-based and dissimilarity-based. Similar to anomaly detection in time series, models based on reconstruction are trained to reconstruct the normal data from a latent space and define the anomaly score as the reconstruction error, whereas dissimilarity-based models assign an anomaly score based on a distance measure.

Reconstruction-based approaches employ an autoencoder that learns to reconstruct the images from the latent space. The anomalies are then detected and localized in pixel-wise fashion by thresholding the anomaly map which is defined as the difference between the original image and the reconstructed images. The assumption is that the autoencoder will fail to reconstruct abnormal images. The challenge in this class of methods is the design of the autoencoder architecture and the loss function used for the training. Collin et al. (2021) proposed the use of an autoencoder with skip connections, where the loss function to minimize is the L_2 distance between the original and

the reconstructed images. In order to prevent the autoencoder from learning the identity mapping and consequently having a low reconstruction error for abnormal images, the authors proposed to corrupt the training images with stain-shaped noise. Bergmann, Löwe, et al. (2018) argued that the use L_2 loss has the shortcoming of assuming that neighboring pixels are independent and that autoencoders using this loss function fail to detect structural differences between the original and the reconstructed image. To overcome these shortcomings, they propose to use the Structural Similarity Metric (SSIM, Zhou Wang et al. (2004)) in the loss function.

In dissimilarity-based approaches, the initial step involves dividing the image into multiple parts, known in the community as image patches, since the goal is to detect and localize the anomalies (this is similar to dividing a time series into subsequences). The most important task in these methods is to learn a representation of the image patches. Once done, the dissimilarity measure in this new feature space provides the anomaly score of the patches of an upcoming image. Multiple strategies were proposed for representation learning and anomaly segmentation. For instance, Yi et al. (2020) suggested the use of self-supervised concept for representation learning, where a CNN is trained for a so-called pretext task, such as predicting the relative location of the patches. After training, the classifier in the CNN is discarded and the output of the last layer of the CNN is used as a feature vector. For anomaly detection in the patch-wise problem, the authors proposed an extension of the deep support vector data description (Deep SVDD) to learn the normal hypersphere of the normal class. Defard et al. (2021) proposed an approach named Patch Distribution Modeling that uses pre-trained CNN models to extract a feature vector of the image patches. To detect anomalies, the feature vectors of the normal patches are modelled as multivariate Gaussian distribution and the Mahalanobis distance is used to test the normality of the patches of upcoming images.

4.3 Methods and materials

Images of the defects that we are interested in detecting can be relatively easy to obtain because of the high number of tubes that are welded and the relatively high proportion of defective welds in this process. This suggests that a supervised model can be adequate for our problem since high detection accuracy is required and, since, supervised models are generally more accurate than

unsupervised models (Aggarwal et al. (2017)). Additionally, another requirement discussed earlier that must be met is the ability to localize the defect in the image. This can be achieved either by employing the concept of object detection or segmentation. The latter provides more precise localization as it operates at the pixel level, but it generally has higher computational complexity and is more laborious in image preprocessing and labeling. For our specific application, precise localization at the pixel level is not required, since we are not interested in further analysis of the defects at this stage. The localization in our case is needed in order to assist the operator with the weld quality inspection.

From the above discussion and the literature review, we can conclude that an object detection model is the most suitable for our problem. Specifically, Yolov3 architecture is known to give a good balance between accuracy and detection speed (C. Li et al. (2020), Nepal et al. (2022)). Therefore, we investigate the use of Yolov3 in our case study.

4.3.1 You Only Look Once v3 network

Yolov3 is a fully convolutional network developed by Redmon and Farhadi (2018) that detects objects at three stages, as shown in Fig. 4.2. It is an improvement of YOLOv2 (Redmon and Farhadi (2017)) and YOLO (Redmon, Divvala, et al. (2016)). The network is a single-stage architecture, which means that it accomplishes the problems of bounding box regression and the classification of the object inside the box in a single shot. This is what makes YOLOv3 fast at inference, which is an important criterion in our case as discussed before.

In YOLOv3, the input image is divided into $S \times S$ grid where each cell is responsible for predicting one object and produces B bounding boxes for that object. In addition to a score of the object presence, which is the probability that the cell is the center of the object, the total predictions produce a tensor of $(S \times S) \times (B \times 5 + C)$ where B is the number of bounding boxes and C the number of classes. In the default setting B is equal to 3. YOLOv3 uses a feature extractor named Darknet-53 and detects the target objects at 3 different scales (Fig. 4.2) to be able to detect objects of various sizes. At each one, a prediction tensor of size $(S \times S) \times (B \times 5 + C)$ is produced. $(S \times S)$ are equal to (13×13) , (26×26) and (52×52) for each scale, respectively.

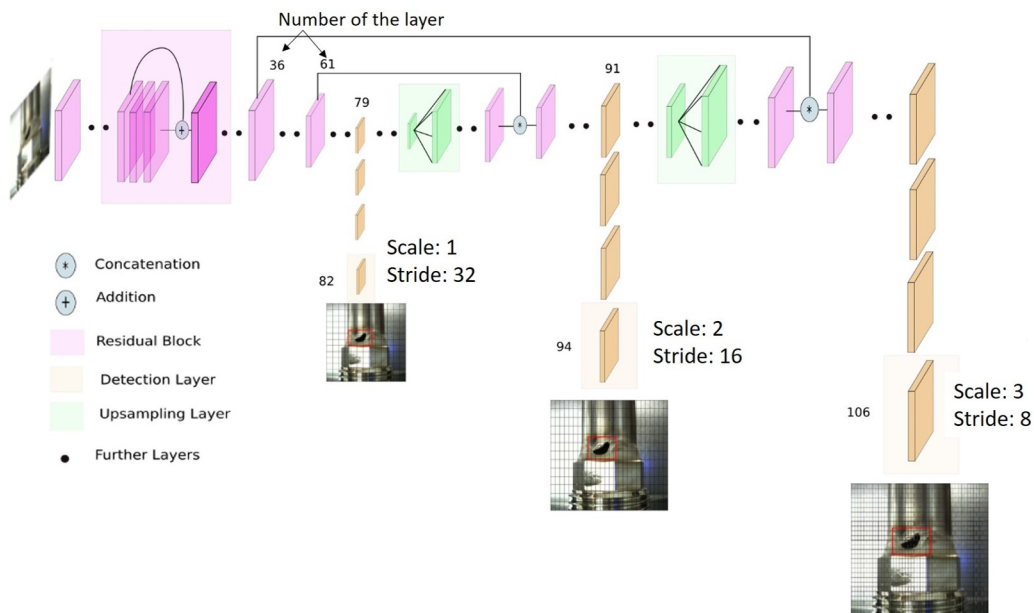


Figure 4.2: illustration of the YOLOv3 architecture.

The loss function of YOLOv3 is multi-objective and defined as follows:

$$\begin{aligned}
 \lambda_{coord} \sum_{i=0}^{S^2} \sum_{j=0}^B \mathbb{1}_{ij}^{obj} [(x_i - \hat{x}_j) + (y_i - \hat{y}_j)] + \lambda_{coord} \sum_{i=0}^{S^2} \sum_{j=0}^B \mathbb{1}_{ij}^{obj} [(w_i - \hat{w}_j) + (h_i - \hat{h}_j)] \\
 + \sum_{i=0}^{S^2} \sum_{j=0}^B \mathbb{1}_{ij}^{obj} (os_i - \hat{os}_i)^2 + \lambda_{noobj} \sum_{i=0}^{S^2} \sum_{j=0}^B \mathbb{1}_{ij}^{noobj} (os_i - \hat{os}_i)^2 \\
 + \sum_{i=0}^{S^2} \mathbb{1}_i^{obj} \sum_{c \in classes} (p_i(c) - \hat{p}_i(c))^2
 \end{aligned} \tag{4.1}$$

Where:

- \hat{x}_i, \hat{y}_i are the predicted coordinates of the top left point of the bounding box
- \hat{w}_i, \hat{h}_i are the predicted width and height of the bounding box
- $\mathbb{1}_i^{obj}$ indicates that the object appears in the cell i
- $\mathbb{1}_{ij}^{obj}$ indicates that the j^{th} bounding box in the cell i is responsible for the prediction.

- λ_{coord} is a weight to give less importance to the loss of predicted coordinates than the class predictions in order to achieve better accuracy of the object detection.
- \hat{os} is the predicted object score.
- λ_{noobj} is a parameter used to ensure that the score is not zero for cells that do not contain an object. This is added in order to prevent instabilities during training.
- $\hat{p}_i(c)$ is the probability of the class of the object.

The first line in Eq. 4.1 is the loss for the problem of the bounding box regression, whereas the second and the third line treat respectively the problem of the object presence and its classification.

The output of prediction for the bounding boxes does not give directly the absolute coordinates, it uses a transformation to give coordinates relative to the location of the grid cell. Moreover, the height and width are given as offsets to B predefined anchor boxes, which are obtained by clustering

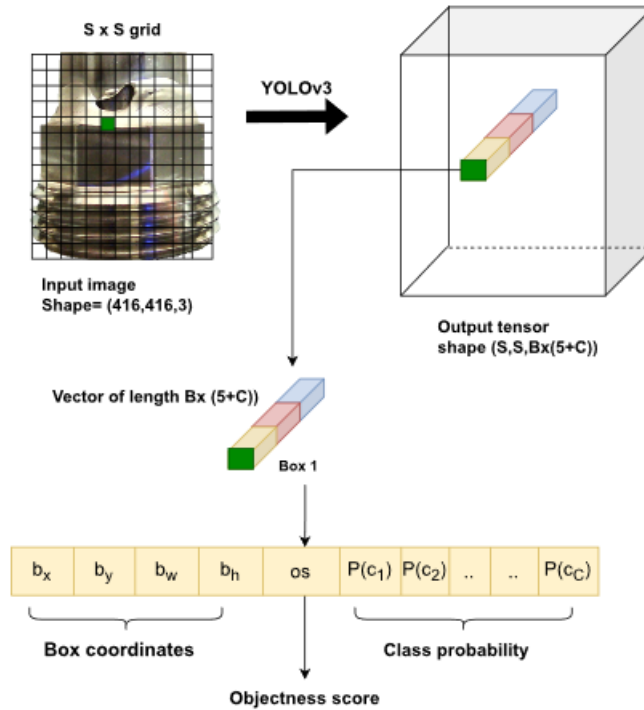


Figure 4.3: The output of YOLO at each prediction level.

ground truth bounding boxes of the COCO dataset. Since YOLOv3 produces a high number of bounding boxes, the Non-Maximum Suppression algorithm is used to make sure that one bounding box per object is returned. This is done by iteratively removing overlapping boxes.

In our experiments, we also use YOLOv3 tiny, which is a variant of the original architecture with fewer layers proposed by the same authors. It uses the Darknet-13 feature extractor composed of 13 layers and produces predictions at two scales as shown by Fig. 4.4. Due to its lightweight, it is much faster to train and faster at inference than YOLOv3.

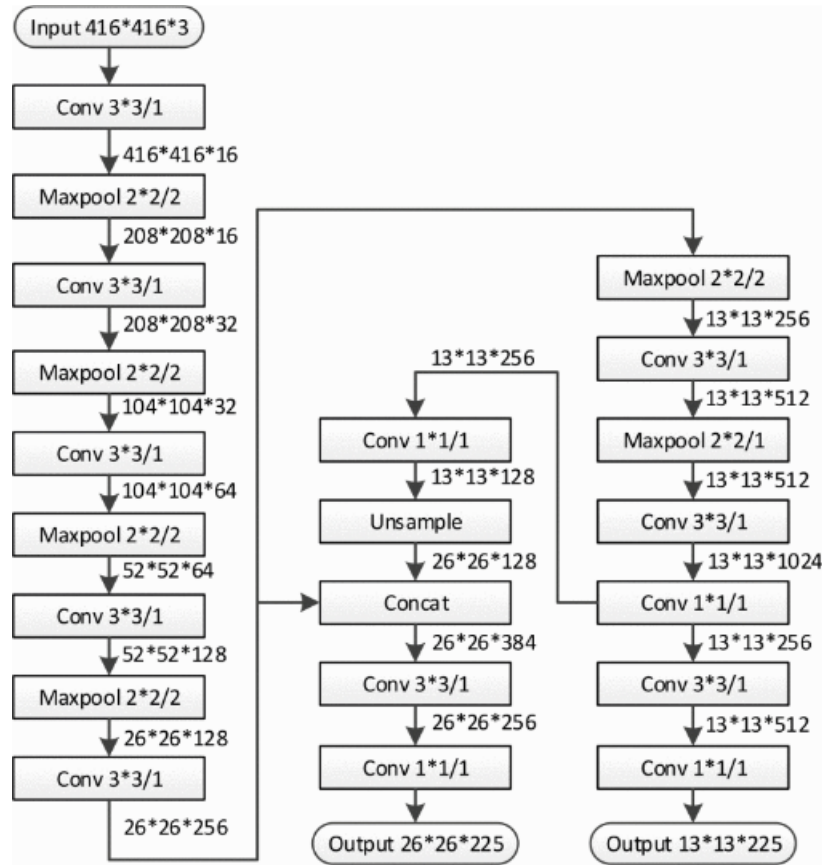


Figure 4.4: The architecture of YOLOv3 Tiny (Ding et al. (2019)).

4.3.2 Evaluation metric

Object detectors are evaluated using Average Precision (AP). AP is an interpolation to approximate the area under the precision-recall curve obtained by the following equations:

$$Precision = \frac{TP}{TP + FP} \quad (4.2)$$

$$Recall = \frac{TP}{TP + FN} \quad (4.3)$$

$$AP = \sum_{n=0}^{N-1} (r_{n+1} - r_n) \max_{\tilde{r}: \tilde{r} \geq r_{n+1}} \rho(\tilde{r}) \quad (4.4)$$

Where :

- TP, FP, FN are respectively the true positives, false positives, and false negatives.
- r is the recall.
- N is the number of images.
- $\rho(\tilde{r})$ the precision at recall \tilde{r} .

In order to declare if a prediction is true positive, two thresholds must be provided, the first for the class probability (CP) below which the predictions are ignored using the Non-Maximum Suppression procedure, and the second for the Intersection Over Union (IOU). The IOU measures how well the model can localize the defects in the images according to the ground truth localization by computing the area of intersection over the area of union between the predicted bounding boxes and ground truth, as shown in Fig. 4.5.

To compare the models, we use the mean Average Precision metric, which is defined as follows:

$$mAP = \frac{\sum_{n=1}^{N_c} (AP_n)}{N_C} \quad (4.5)$$

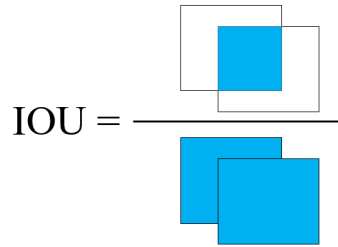


Figure 4.5: Illustration of the IOU.

Where :

- N_c is the number of classes,
- AP_n is the AP for the class n

4.3.3 Image acquisition system

The image acquisition system must be able to obtain images of the whole circular weld for both connection parts simultaneously. Furthermore, the system must require minimal manipulations by the operator in order to minimize the control duration. To satisfy these criteria, we proposed the conception shown in Fig. 4.6. We found that 3 cameras are needed for each of the two welds to capture the entire circular weld seam. The closed shape of the system minimizes the changes of the brightness and also helps in preventing background errors that could be generated by the detector. The rod in the middle is used for placing the tube and fixing its position.

Since the cameras' locations are close to the tube, we do not need a high-resolution camera, we use simple 2 Megapixel USB camera modules shown in Fig. 4.7. Each 3 cameras are connected to the computer via a USB hub. This allows to open two cameras at a time, which accelerates the control.

The system is easy to use, requiring the operator to simply place the tube inside the box supported by the rod and click the button on the developed graphical user interface to initiate the image acquisition and the control. This meets the defined requirements for ease of use and the

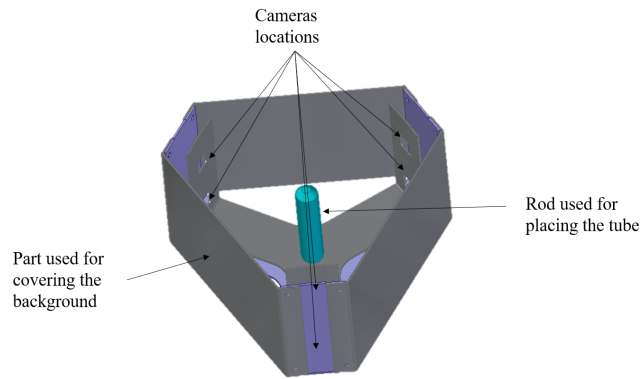


Figure 4.6: The proposed image acquisition system.



Figure 4.7: The USB camera module used for image acquisition.

reproducibility of the control conditions. In the next section, we show how the system is used for the control of welds, along with the results of the developed YOLOv3 model.

4.4 Results and discussion

The image acquisition system was first used to obtain images of tubes with defective welds. The images were captured directly in the workshop in order to acquire training and test images that reflect the real conditions in which the model will be used. Moreover, the anomalies do not always appear in the center of the weld. Thus, it is important that they appear at different locations in the weld for training the detection model. We do this by capturing images of the anomalous welds while rotating the tube placed in the image acquisition system.

We noticed that some impurities that the electrode can leave on the weld seam, which are not

faults, and which appear as black circles could make the detector have a high false positive rate as it may detect them as burn-through 1. This was also noted in the study by Sun et al. (2019) where they proposed to treat them as "pseudo-defects". We follow this idea in order to prevent false detection by adding these impurities as a fourth object to be detected. The 3 defects and the pseudo-defect that we seek to detect are shown in Fig. 4.8.

Table 4.1 gives the number of objects in the images used for training and testing the model. Since deep learning models require a high number of images. We augment the dataset by employing random flips, translations, and crops for all the training images. We also use fine-tuning of the weights of the YOLOv3 model trained on the COCO dataset in order to accelerate the convergence and overcome the problem of the relatively small dataset used in the study.

We train four models; two YOLOv3 and two YOLOv3 Tiny, with a batch size of 8 and 16 for each architecture for 100 epochs using the TensorFlow framework. the input images are always resized to 416×416 . We study two cases where CP is fixed at 0.3 and then 0.5 while keeping the

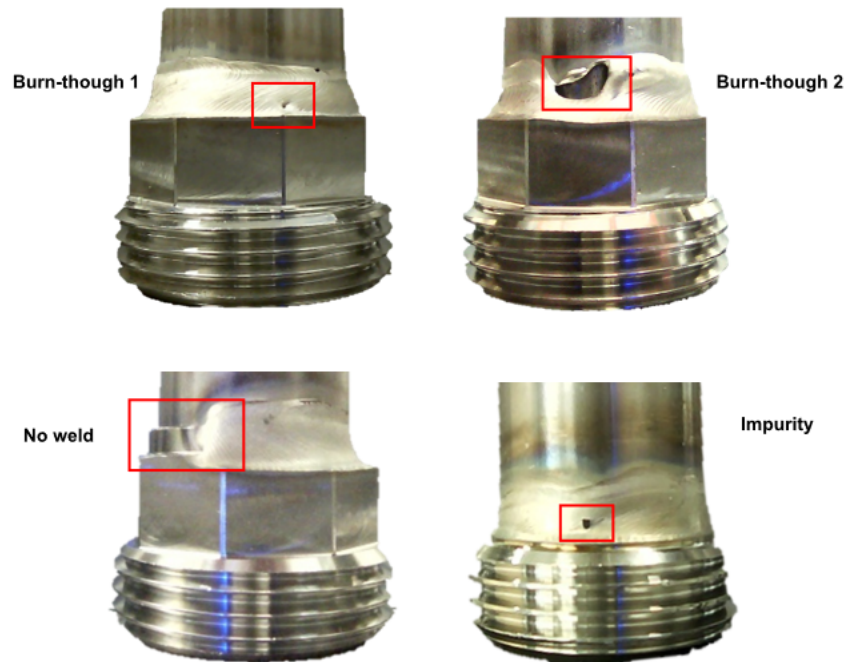


Figure 4.8: The four objects to be detected: three defects and one pseudo defect (impurity).

Table 4.1: The number of images used in the study.

	Category			
	<i>burn-through 1</i>	<i>burn-through 2</i>	<i>No weld</i>	<i>Impurity</i>
Train	1169	379	210	186
Test	480	153	93	79

IOU threshold at 50%.

The results for each model are given in Table 4.2. For all models, the APs for burn-through 1 (BT 1) and Impurity (Imp) are lower than those of burn-through 2 (BT 2) and no weld (NW) defects. This is explained by the fact that these objects are smaller. For YOLOv3 models, increasing batch size to 16 increases the AP for burn through 1 and Impurity and the mAP. The mAP of the models based on YOLOv3 tiny is reduced when the batch size is increased from 8 to 16. From mAP in Table 4.2, we conclude that the model YOLOv3 trained with a batch size of 16 with CP=0.3 is the most accurate and achieves a mAP of 93.91%, which can be seen as good results. We also note that if we remove the AP of the Impurity class, which is only added in order to reduce false detection and is not a real defect, the mAP increases to 96.63%.

The images used in the test are all of defective welds. To get an estimation of false positives of the model when there are no anomalies, we test it on 230 images of good welds using the confidence threshold of the selected model. Seven (7) false anomalies were detected, which represents 3% of the number of images. This shows that the model generates only a few false positives and is ready to be deployed. Fig. 4.9 shows the components of the proposed inspection system. We developed a software using Python based on the YOLOv3 model shown in Fig. 4.10 that begins by acquiring the images using the OpenCV library. After the 6 images are fed to the model, the predicted bounding boxes are shown along with a pop-up that informs the operator if the model has found any defect in any of the 6 images or if no defect is detected. Two buttons are created in the pop-up that allows the operator to confirm if the control is correct. If not, the images are automatically stored. This can help track the performance of the model over time and re-train the model with these new instances in the future in order to improve the accuracy of the model. Furthermore, all the images for which the model predicts the presence of defects are automatically saved, which can help experts in further analysis of the welding defects and also enrich the database.

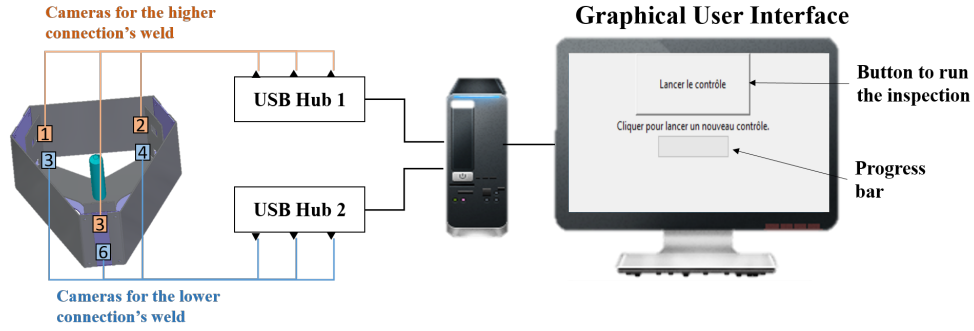


Figure 4.9: The proposed system for the welding inspection.

The inference time of the YOLOv3 model is 0.45 seconds per image on average, while the whole control from image acquisition to the prediction output takes around 30 seconds. With this meeting the constraint on the control duration, the system is now in use as a part of the tube welding process as shown in Fig. 4.11.

Despite the good detection results, the proposed methodology has some limitations, First, if we

Table 4.2: The AP of each class with the mAP of each model.

(BT 1= Burn-through 1, BT 2= Burn-through 2, NW= No Weld, Imp=Impurity).

Model	Defect	AP50 (CP=0.3)	mAP	AP50 (CP=0.5)	mAP
Yolov3 (batch=8)	BT 1	91.686%	91.63%	90.927%	90.25%
	BT 2	99.329%		98.684%	
	NW	98.481%		97.429%	
	Imp	77.063%		73.988%	
Yolov3 (batch=16)	BT 1	93.956%	93.91%	93.383%	92.81%
	BT 2	98.646%		98.005%	
	NW	97.288%		97.288%	
	Imp	85.783%		82.595%	
Yolov3 Tiny (batch=8)	BT 1	85.857%	85.99%	81.789%	82.13%
	BT 2	97.608%		96.976%	
	NW	92.948%		89.842%	
	Imp	64.584%		59.929%	
Yolov3 Tiny (batch=16)	BT 1	79.452%	83.95%	73.045%	78.22%
	BT 2	95.805%		93.977%	
	NW	94.808%		88.582%	
	Imp	65.761%		57.296%	

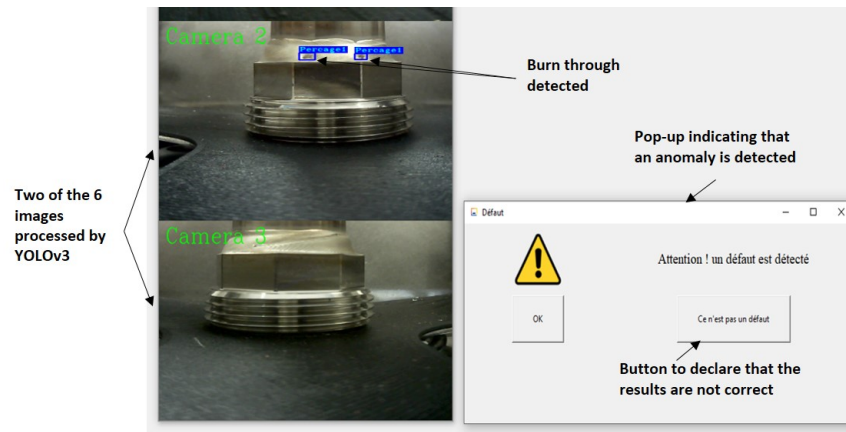


Figure 4.10: A screenshot of the developed GUI.



Figure 4.11: The quality control station based on the proposed system.

discard the AP of the pseudo-defect, we see that the AP of burn-through 1 is the lowest because of the small size of this defect. In future works, improving the detection of this class of anomaly should be investigated. Moreover, as the model is trained on images captured in fixed conditions, its performance might degrade when illumination conditions change or when changing the type of cameras used for image acquisition. Furthermore, since YOLO3 is a supervised model, it is not able to detect the emergence of new classes of defects. A possible solution to this problem is to employ



Figure 4.12: A defect detected by the model on an image of a different welding process.

unsupervised learning for anomaly segmentation, we explore this in Appendix H.

On the other hand, an advantage of the computer vision-based detection model is that it might be used directly for detecting defects in the other welding processes or to fine-tune new models based on the developed one. We tested this using an image of a defective CMT weld at the intersection between the cylinder and the cap. As shown in Fig. 4.12 the model was able to detect the burn-through in this weld.

4.5 Conclusion

In this chapter, we proposed a complete computer vision-based control system for post-welding defect detection for the hot water tank connection tubes to overcome the problem of the unavailability of signal acquisition systems. We designed and developed an easy-to-use image acquisition system and software, and we compared models based on YOLOv3 and Yolov3 tiny with different hyperparameters and selected the one with the highest accuracy for the industrial application. The model has a mAP of 93.91% with the pseudo-defect and 96.63% without, which can be seen as a high accuracy.

In future works, it would be interesting to compare YOLOv3 with other object detection networks such as Fast R-CNN using more images and other welding defects. Furthermore, investigating and statistically evaluating the direct use of the computer vision model in other welding processes in the manufacturing of hot water tanks would be an interesting research direction. Another important

improvement to be studied in future works is the detection of defects with a small size, especially since they are the most critical as they are the hardest to detect by human visual inspection.

Collecting and annotating defective weld images can be expensive and time-consuming. Even if efforts are put into defective weld image acquisition, it is unlikely that this would cover all types of welding defects. Hence, investigating unsupervised welding anomaly detection from images would be a highly relevant research direction in future works.

General conclusion

Summary of the work

In this thesis, we proposed statistical and machine learning approaches for the problem of welding defect detection and diagnosis in the context of the manufacturing of hot water tanks. In the first chapter, we studied the feasibility of welding defect detection from welding signals, and we proposed a supervised machine learning approach to detect and localize burn-through in the voltage signal. Moreover, we conducted a study that showed the possibility of predicting the root cause of the burn-through from the voltage signals. Furthermore, by studying the localization and the signature of the defect in the signal, we proposed solutions to reduce the occurrence of burn-through in the circular welding process.

In the second chapter, we proposed an approach based on One-Class SVM and distance substitution kernels. This approach requires only data of defect-free welds in the training stage, which overcomes the problem of the lack of labels, as it can detect any anomaly of the voltage signal. Moreover, unlike most of the approaches proposed for welding defect detection, the proposed approach does not rely on designing adequate features for each welding process and instead works with the raw signals and detects anomalies depending on their distance to the normal data, which makes it easier to generalize across signals of different types captured from different welding processes. Furthermore, unlike most distance-based techniques, One-Class SVM with distance substitution kernels requires only the distances to the support vectors, which has the advantage of fast inference. Results of the experiments showed that the proposed approach is more accurate and faster

than known techniques from the literature. Furthermore, we showed that the approach can be extended to multivariate welding signals by using dissimilarities defined for multivariate time series.

In addition to anomaly detection, we also proposed a diagnosis approach based on classifying the anomalous subsequences of the signals using random convolutional kernel transform. This method classifies the abnormal subsequences based on both the global and local patterns, which is more convenient since there can be local patterns that differentiate between defects classes. Furthermore, the approach is faster than shapelet-based techniques, which makes it more adequate for our problem where fast inference is needed. Software based on both anomaly detection and diagnosis we proposed in this work was developed and is in use for real-time monitoring of the circular welding.

An additional method is proposed in Chapter 3 where we extended the random convolutional kernel transform to the problem of anomaly detection. Two approaches were proposed. The first approach aims to integrate explainability in anomaly detection. This is achieved by extracting the maximum values of the convolutions and using them as input vectors for an OC-SVM model. When an abnormal subsequence is detected, an importance value is assigned to each random kernel to reveal the anomalous patterns. The most important kernels can then be used to explain the abnormal patterns in the subsequence. The approach has proven effective in explaining welding defects that appear as abnormal shapelets and trends in the voltage signal. Additionally, results show that the explainability approach works well even when a large number of convolutional kernels are employed. Furthermore, despite the randomness incorporated in the approach, the results showed that the explanations provided remain consistent across different runs.

In the second approach, we studied the combination of random convolutional kernel transform with dimensionality reduction techniques with the aim of developing a generic and efficient method for abnormal time series subsequence detection. The results showed that extracting both the proportion of positive values and the maximum value from the convolutions with random kernels is promising as a generic representation of the subsequences. Moreover, results revealed that the best dimensionality reduction technique in terms of preserving accuracy is the Principal Component Analysis. Experiments also showed that when the abnormal subsequences should be detected based on their global shape, discarding low dilation values can result in increasing the accuracy

while avoiding the need for a large number of random convolutional kernels. For both approaches, we also found that the transform allows the detection of anomalies of different lengths in the subsequences, which is an important advantage compared to most known approaches, which are sensitive to the length of the window used to extract the subsequences from the time series.

Besides detecting welding defects from welding signals, we addressed in Chapter 4 the problem of computer vision-based defect detection and we proposed a complete system that detects defects from weld images. We designed and implemented an image acquisition system and we trained a neural network able to localize and classify welding defects. We fine-tuned and compared pre-trained models based on YOLOv3 and Yolov3 tiny with different hyperparameters and selected the one with the highest accuracy for the industrial application. The model had a mean average precision of 93.91% with the pseudo-defect and 96.63% without, which can be seen as high accuracy. Software based on the trained neural network was developed and is in use in the production line for automatic welding defect detection.

Perspectives for future works

There are multiple interesting directions for future works on the subject treated in this thesis. We can classify the perspectives into three categories: defect detection, defect diagnosis, and prognosis.

Defect Detection

- We tested the One-Class SVM with distance substitution kernels using the Euclidean distance and the lower bound of the Dynamic Time Warping. It would be interesting in future works to study the use of other time series distances.
- We showed in Chapter 2 that One-Class SVM with distance substitution kernels can be used for multivariate time series. It would be interesting to evaluate the approach using distances that are able to take into consideration the correlation structure of the time series.
- Like most of the approaches intended for abnormal subsequence detection, OC-SVM with dis-

tance substitution kernels can be sensitive to the length of the moving window used to extract the subsequences. An interesting direction to overcome this shortcoming is to further explore the two proposed approaches we proposed in the appendix, which are based on segmentation to detect abnormal subsequences with variable lengths. This would allow avoiding the problem of tuning the length of the moving window and can be used to estimate the measures of the defect based on the length of the corresponding abnormal subsequence in the signal.

- We assumed in the work of the thesis that the normality does not change over time. However, this can occur. Hence, in future works, it would be interesting to extend the approaches in order for the anomaly detector to automatically adapt to such changes, known in the literature as concept drifts.
- We studied in Chapter 3 the combination of the random convolutional kernel transform with dimensionality reduction techniques for the problem of anomaly detection. It would be relevant to study in future works further dimensionality reduction techniques. Moreover, instead of using One-Class SVM as the anomaly detector, it would be interesting to investigate the use of other anomaly detection techniques with the random convolutional kernel transform.
- We proposed in this thesis distance-based and feature-based approaches for anomaly detection. An interesting extension of the work would be to explore ensembling strategies to combine both concepts.
- Concerning computer vision-based defect detection, a possible future work would be to further study the approach we proposed in the appendix for the unsupervised defect detection from weld images.

Defect Diagnosis

Concerning the diagnosis, we proposed in Chapter 2 a classification-based method for diagnosing welding defects. In Chapter 3 we introduced explainability, and in the appendix the clustering of abnormal subsequences based on the random convolutional kernel transform, which can be used as unsupervised diagnosis methods.

- As discussed throughout this thesis, a wide range of welding defects can occur. It would be time-consuming and difficult to gather labels for all the possible defects in each welding process. Hence, an interesting future work would be to extend the classification or the clustering method to detect and adapt to the appearance of new classes of defects.
- For computer vision-based defect detection, a possible extension would be to use supervised or unsupervised anomaly segmentation and the use of information, such as the measure of the defect and its localization in the weld seam, for an automatic diagnosis.

Prognosis

Concerning prognosis, we propose the following subjects for future works:

- Exploring methods from the field of remaining useful life (RUL) estimation and early classification of time series for the early prediction of burn-through. This would allow stopping the welding before the occurrence of the defect, which would result in reducing the scrap and rework costs.
- In order to obtain a weld with high quality, it is important that the parts of the welding machine are in a good health state. To ensure this, RUL estimation can be used to predict the health state of the components and for scheduling maintenance actions. This could be done by designing and studying the evolution over time of features extracted from the welding signals that indicate the health state of the components, which are known as health indexes in the literature of RUL estimation.
- We have seen that misalignment and burn-through are caused by distortions and non-conformities in the parts to be assembled. Therefore, ensuring the quality of the parts to be assembled is also an important factor in obtaining a defect-free weld. This can be done with the help of machine learning. For example, computer vision systems can be developed to detect distortions in the pieces before launching the welding. In addition, it would be interesting to study the causalities between successive welding processes in order to develop approaches that predict, at the output of process i , the likelihood of obtaining a fault in process $i + 1$. An

example would be the longitudinal welding, which impacts the quality of the circular welding, as we saw in Chapter 1.

Bibliography

- Abanda, Amaia et al. (2019). “A review on distance based time series classification”. In: *Data Mining and Knowledge Discovery* 33.2, pp. 378–412.
- Aggarwal, Charu C et al. (2017). *An introduction to outlier analysis*. Springer.
- Angelov, Plamen P et al. (2021). “Explainable artificial intelligence: an analytical review”. In: *Wiley Interdisciplinary Reviews: Data Mining and Knowledge Discovery* 11.5, e1424.
- Antonini, JM (2014). “Health effects associated with welding”. In.
- Arabaci, Hayri et al. (2019). “Weld Defect Categorization from Welding Current using Principle Component Analysis”. In: *International Journal of Advanced Computer Science and Applications* 10.6.
- Ariannik, Mohamadreza et al. (2020). “Processing magnetometer signals for accurate wide-area geomagnetic disturbance monitoring and resilience analysis”. In: *IEEE Transactions on Power Delivery* 36.4, pp. 2550–2558.
- Bagnall, Anthony et al. (2017). “The great time series classification bake off: a review and experimental evaluation of recent algorithmic advances”. In: *Data mining and knowledge discovery* 31, pp. 606–660.
- Bahlmann, Claus et al. (2002). “Online handwriting recognition with support vector machines—a kernel approach”. In: *Proceedings eighth international workshop on frontiers in handwriting recognition*. IEEE, pp. 49–54.
- Beggel, Laura et al. (2019). “Time series anomaly detection based on shapelet learning”. In: *Computational Statistics* 34, pp. 945–976.

- Bereziński, Przemysław et al. (2015). “An entropy-based network anomaly detection method”. In: *Entropy* 17.4, pp. 2367–2408.
- Bergmann, Paul, Michael Fauser, et al. (2019). “MVTec AD—A comprehensive real-world dataset for unsupervised anomaly detection”. In: *Proceedings of the IEEE/CVF conference on computer vision and pattern recognition*, pp. 9592–9600.
- Bergmann, Paul, Sindy Löwe, et al. (2018). “Improving unsupervised defect segmentation by applying structural similarity to autoencoders”. In: *arXiv preprint arXiv:1807.02011*.
- Bigdeli, Elnaz et al. (2017). “A fast and noise resilient cluster-based anomaly detection”. In: *Pattern Analysis and Applications* 20, pp. 183–199.
- Bingul, Zafer et al. (2000). “Application of fuzzy logic to spatial thermal control in fusion welding”. In: *IEEE Transactions on Industry Applications* 36.6, pp. 1523–1530.
- Blazquez-Garcia, Ane et al. (2021). “A review on outlier/anomaly detection in time series data”. In: *ACM Computing Surveys (CSUR)* 54.3, pp. 1–33.
- Boniol, Paul et al. (2020). “SAD: an unsupervised system for subsequence anomaly detection”. In: *2020 IEEE 36th International Conference on Data Engineering (ICDE)*. IEEE, pp. 1778–1781.
- Braei, Mohammad et al. (2020). “Anomaly detection in univariate time-series: A survey on the state-of-the-art”. In: *arXiv preprint arXiv:2004.00433*.
- Brock, Fred V (1986). “A nonlinear filter to remove impulse noise from meteorological data”. In: *Journal of Atmospheric and Oceanic Technology* 3.1, pp. 51–58.
- Bu, Yingyi et al. (2007). “Wat: Finding top-k discords in time series database”. In: *Proceedings of the 2007 SIAM International Conference on Data Mining*. SIAM, pp. 449–454.
- Chandola, Varun, Arindam Banerjee, et al. (2009). “Anomaly detection: A survey”. In: *ACM computing surveys (CSUR)* 41.3, pp. 1–58.
- Chandola, Varun, Deepthi Cheboli, et al. (2009). “Detecting anomalies in a time series database”. In: .
- Chauhan, Sucheta et al. (2015). “Anomaly detection in ECG time signals via deep long short-term memory networks”. In: *2015 IEEE international conference on data science and advanced analytics (DSAA)*. IEEE, pp. 1–7.
- Chen, Changhong et al. (2022). “An improved faster RCNN-based weld ultrasonic atlas defect detection method”. In: *Measurement and Control*, p. 00202940221092030.

- Chen, Chao et al. (2011). “Energy outlier detection in smart environments”. In: *Workshops at the Twenty-Fifth AAAI Conference on Artificial Intelligence*.
- Chen, Junsheng et al. (2020). “Anomaly detection for wind turbines based on the reconstruction of condition parameters using stacked denoising autoencoders”. In: *Renewable Energy* 147, pp. 1469–1480.
- Chen, Kai et al. (2019). “Prediction of weld bead geometry of MAG welding based on XGBoost algorithm”. In: *The International Journal of Advanced Manufacturing Technology* 101, pp. 2283–2295.
- Chen, Tingting et al. (2020). “Unsupervised anomaly detection of industrial robots using sliding-window convolutional variational autoencoder”. In: *IEEE Access* 8, pp. 47072–47081.
- Chen, Yunke et al. (2021). “Narrow gap deviation detection in Keyhole TIG welding using image processing method based on Mask-RCNN model”. In: *The International Journal of Advanced Manufacturing Technology* 112, pp. 2015–2025.
- Choi, Taesung et al. (2022). “Multivariate time-series anomaly detection using SeqVAE-CNN hybrid model”. In: *2022 International Conference on Information Networking (ICOIN)*. IEEE, pp. 250–253.
- Cocota Jr, José Alberto Naves et al. (2017). “Discontinuity detection in the shield metal arc welding process”. In: *Sensors* 17.5, p. 1082.
- Collin, Anne-Sophie et al. (2021). “Improved anomaly detection by training an autoencoder with skip connections on images corrupted with stain-shaped noise”. In: *2020 25th International Conference on Pattern Recognition (ICPR)*. IEEE, pp. 7915–7922.
- Costabel, Stephan et al. (2014). “Despiking of magnetic resonance signals in time and wavelet domains”. In: *Near Surface Geophysics* 12.2, pp. 185–198.
- Cruz, Yarens J et al. (2021). “Ensemble of convolutional neural networks based on an evolutionary algorithm applied to an industrial welding process”. In: *Computers in Industry* 133, p. 103530.
- Cui, Yanxin et al. (2020). “Welding penetration recognition based on arc sound and electrical signals in K-TIG welding”. In: *Measurement* 163, p. 107966.
- Defard, Thomas et al. (2021). “Padim: a patch distribution modeling framework for anomaly detection and localization”. In: *Pattern Recognition. ICPR International Workshops and Challenges: Virtual Event, January 10–15, 2021, Proceedings, Part IV*. Springer, pp. 475–489.

- Dempster, Angus et al. (2020). “ROCKET: exceptionally fast and accurate time series classification using random convolutional kernels”. In: *Data Mining and Knowledge Discovery* 34.5, pp. 1454–1495.
- Ding, Sha et al. (2019). “A novel YOLOv3-tiny network for unmanned airship obstacle detection”. In: *2019 IEEE 8th Data Driven Control and Learning Systems Conference (DDCLS)*. IEEE, pp. 277–281.
- Dragomiretskiy, Konstantin et al. (2013). “Variational mode decomposition”. In: *IEEE transactions on signal processing* 62.3, pp. 531–544.
- El Hachem, Charbel et al. (2021). “Welding seam classification in the automotive industry using deep learning algorithms”. In: *2021 IEEE International Conference on Industry 4.0, Artificial Intelligence, and Communications Technology (IAICT)*. IEEE, pp. 235–240.
- Ferraty, Frédéric et al. (2003). “Curves discrimination: a nonparametric functional approach”. In: *Computational Statistics & Data Analysis* 44.1-2, pp. 161–173.
- Grabocka, Josif et al. (2014). “Learning time-series shapelets”. In: *Proceedings of the 20th ACM SIGKDD international conference on Knowledge discovery and data mining*, pp. 392–401.
- Guo, Weihong et al. (2016). “Online process monitoring with near-zero misdetection for ultrasonic welding of lithium-ion batteries: An integration of univariate and multivariate methods”. In: *Journal of Manufacturing Systems* 38, pp. 141–150.
- Hall, Peter et al. (2001). “A functional data—analytic approach to signal discrimination”. In: *Technometrics* 43.1, pp. 1–9.
- Hanczar, Blaise et al. (2008). “Classification with reject option in gene expression data”. In: *Bioinformatics* 24.17, pp. 1889–1895.
- He, Kuanfang et al. (2019). “Time–frequency feature extraction of acoustic emission signals in aluminum alloy MIG welding process based on SST and PCA”. In: *IEEE Access* 7, pp. 113988–113998.
- Hills, Jon et al. (2014). “Classification of time series by shapelet transformation”. In: *Data mining and knowledge discovery* 28, pp. 851–881.
- Hu, Min et al. (2018). “Detecting anomalies in time series data via a meta-feature based approach”. In: *Ieee Access* 6, pp. 27760–27776.
- Huang, Nantian et al. (2015). “Mechanical fault diagnosis of high voltage circuit breakers based on wavelet time-frequency entropy and one-class support vector machine”. In: *Entropy* 18.1, p. 7.

- Huang, Yong, Xiaowei Wang, et al. (2021). “A weld quality classification approach based on local mean decomposition and deep belief network”. In: *Journal of Materials Engineering and Performance* 30, pp. 2229–2237.
- Huang, Yong, Dongqing Yang, et al. (2020). “Stability analysis of GMAW based on multi-scale entropy and genetic optimized support vector machine”. In: *Measurement* 151, p. 107282.
- Hundman, Kyle et al. (2018). “Detecting spacecraft anomalies using lstms and nonparametric dynamic thresholding”. In: *Proceedings of the 24th ACM SIGKDD international conference on knowledge discovery & data mining*, pp. 387–395.
- Iandola, Forrest N et al. (2016). “SqueezeNet: AlexNet-level accuracy with 50x fewer parameters and < 0.5 MB model size”. In: *arXiv preprint arXiv:1602.07360*.
- Ishimtsev, Vladislav et al. (2017). “Conformal k -NN Anomaly Detector for Univariate Data Streams”. In: *Conformal and Probabilistic Prediction and Applications*. PMLR, pp. 213–227.
- Janssens, Olivier et al. (2016). “Convolutional neural network based fault detection for rotating machinery”. In: *Journal of Sound and Vibration* 377, pp. 331–345.
- Jin, Chengnan and Sehun Rhee (2021). “Real-Time Weld Gap Monitoring and Quality Control Algorithm during Weaving Flux-Cored Arc Welding Using Deep Learning”. In: *Metals* 11.7, p. 1135.
- Jin, Chengnan, Seungmin Shin, et al. (2020). “Prediction model for back-bead monitoring during gas metal arc welding using supervised deep learning”. In: *IEEE Access* 8, pp. 224044–224058.
- Kamalov, Firuz (2020). “Kernel density estimation based sampling for imbalanced class distribution”. In: *Information Sciences* 512, pp. 1192–1201.
- Karlsson, Isak et al. (2016). “Generalized random shapelet forests”. In: *Data mining and knowledge discovery* 30, pp. 1053–1085.
- Keogh, Eamonn (2003). “Efficiently finding arbitrarily scaled patterns in massive time series databases”. In: *Knowledge Discovery in Databases: PKDD 2003: 7th European Conference on Principles and Practice of Knowledge Discovery in Databases, Cavtat-Dubrovnik, Croatia, September 22-26, 2003. Proceedings 7*. Springer, pp. 253–265.
- Keogh, Eamonn and Jessica Lin (2005). “Clustering of time-series subsequences is meaningless: implications for previous and future research”. In: *Knowledge and information systems* 8, pp. 154–177.

- Keogh, Eamonn, Jessica Lin, and Ada Fu (2004). “HOT SAX: Finding the most unusual time series subsequence: Algorithms and applications”. In: *proceedings of the Proc. of the 5th IEEE Int. Conf. On data mining*, pp. 440–449.
- Keogh, Eamonn and Chotirat Ann Ratanamahatana (2005). “Exact indexing of dynamic time warping”. In: *Knowledge and information systems 7*, pp. 358–386.
- Keogh, Eamonn, Dutta Roy Taposh, et al. (2021). “Multi-dataset time-series anomaly detection competition”. In: *ACM SIGKDD International Conference on Knowledge Discovery and Data Mining*. <https://compete.hexagonml.com/practice/competition/39>.
- Kha, Nguyen Huy et al. (2015). “From cluster-based outlier detection to time series discord discovery”. In: *Trends and Applications in Knowledge Discovery and Data Mining: PAKDD 2015 Workshops: BigPMA, VLSP, QIMIE, DAEBH, Ho Chi Minh City, Vietnam, May 19-21, 2015. Revised Selected Papers*. Springer, pp. 16–28.
- Khumaidi, Agus et al. (2017). “Welding defect classification based on convolution neural network (CNN) and Gaussian kernel”. In: *2017 international seminar on intelligent technology and its applications (ISITIA)*. IEEE, pp. 261–265.
- Kim, Chisung et al. (2022). “Weld crack detection and quantification using laser thermography, mask R-CNN, and CycleGAN”. In: *Automation in Construction 143*, p. 104568.
- Kromanis, Rolands et al. (2013). “Support vector regression for anomaly detection from measurement histories”. In: *Advanced Engineering Informatics 27.4*, pp. 486–495.
- Kromkowski, Peter et al. (2019). “Evaluating statistical models for network traffic anomaly detection”. In: *2019 systems and information engineering design symposium (SIEDS)*. IEEE, pp. 1–6.
- Kumaresan, Samuel et al. (2021). “Transfer learning with CNN for classification of weld defect”. In: *IEEE Access 9*, pp. 95097–95108.
- Landgrebe, Thomas CW et al. (2006). “The interaction between classification and reject performance for distance-based reject-option classifiers”. In: *Pattern Recognition Letters 27.8*, pp. 908–917.
- Lei, Lei et al. (2023). “A dynamic anomaly detection method of building energy consumption based on data mining technology”. In: *Energy 263*, p. 125575.
- Lei, Zhen et al. (2020). “Anomaly detection of bridge health monitoring data based on KNN algorithm”. In: *Journal of Intelligent & Fuzzy Systems 39.4*, pp. 5243–5252.

- Lemire, Daniel (2009). “Faster retrieval with a two-pass dynamic-time-warping lower bound”. In: *Pattern recognition* 42.9, pp. 2169–2180.
- Li, Chong et al. (2020). “Face detection based on YOLOv3”. In: *Recent Trends in Intelligent Computing, Communication and Devices: Proceedings of ICCD 2018*. Springer, pp. 277–284.
- Li, Yuxing et al. (2022). “A defect detection system for wire arc additive manufacturing using incremental learning”. In: *Journal of Industrial Information Integration* 27, p. 100291.
- Li, Zhong et al. (2022). “A Survey on Explainable Anomaly Detection”. In: *arXiv preprint arXiv:2210.06959*.
- Lian, Heng (2012). “On feature selection with principal component analysis for one-class SVM”. In: *Pattern Recognition Letters* 33.9, pp. 1027–1031.
- Liu, Chenyu et al. (2021). “A Deep Support Vector Data Description Method for Anomaly Detection in Helicopters”. In: *PHM Society European Conference*. Vol. 6. 1, pp. 9–9.
- Liu, Moyun et al. (2021). “LF-YOLO: A lighter and faster yolo for weld defect detection of X-ray image”. In: *arXiv preprint arXiv:2110.15045*.
- Lorena, Luiz HN et al. (2015). “Filter feature selection for one-class classification”. In: *Journal of Intelligent & Robotic Systems* 80, pp. 227–243.
- Lu, Hui et al. (2018). “An outlier detection algorithm based on cross-correlation analysis for time series dataset”. In: *Ieee Access* 6, pp. 53593–53610.
- Lundberg, Scott M et al. (2017a). “A unified approach to interpreting model predictions”. In: *Advances in neural information processing systems* 30.
- (2017b). “Consistent feature attribution for tree ensembles”. In: *arXiv preprint arXiv:1706.06060*.
- Ma, Junshui et al. (2003). “Time-series novelty detection using one-class support vector machines”. In: *Proceedings of the International Joint Conference on Neural Networks, 2003*. Vol. 3. IEEE, pp. 1741–1745.
- Ma, Liang et al. (2018). “Root cause diagnosis of quality-related faults in industrial multimode processes using robust Gaussian mixture model and transfer entropy”. In: *Neurocomputing* 285, pp. 60–73.
- Malarvel, Muthukumaran et al. (2021). “An autonomous technique for weld defects detection and classification using multi-class support vector machine in X-radiography image”. In: *Optik* 231, p. 166342.
- Malhotra, Pankaj et al. (2015). “Long Short Term Memory Networks for Anomaly Detection in Time Series.” In: *ESANN*. Vol. 2015, p. 89.

- Mirapeix, J et al. (2007). “Real-time arc-welding defect detection and classification with principal component analysis and artificial neural networks”. In: *NDT & e International* 40.4, pp. 315–323.
- Moayedi, H Zare et al. (2008). “Arima model for network traffic prediction and anomaly detection”. In: *2008 international symposium on information technology*. Vol. 4. IEEE, pp. 1–6.
- Moinuddin, Syed Quadir et al. (2021). “A study on weld defects classification in gas metal arc welding process using machine learning techniques”. In: *Materials Today: Proceedings* 43, pp. 623–628.
- Munir, Mohsin et al. (2018). “DeepAnT: A deep learning approach for unsupervised anomaly detection in time series”. In: *Ieee Access* 7, pp. 1991–2005.
- Narwadkar, Aniket et al. (2016). “Optimization of MIG welding parameters to control the angular distortion in Fe410WA steel”. In: *Materials and Manufacturing Processes* 31.16, pp. 2158–2164.
- Nepal, Upesh et al. (2022). “Comparing YOLOv3, YOLOv4 and YOLOv5 for autonomous landing spot detection in faulty UAVs”. In: *Sensors* 22.2, p. 464.
- Ord, Keith (1996). “Outliers in statistical data: V. barnett and t. lewis, 1994, (john wiley & sons, chichester), 584 pp.,[UK pound] 55.00, ISBN 0-471-93094-6”. In: *International Journal of Forecasting* 12.1, pp. 175–176.
- Pal, Sukhomay et al. (2008). “Neurowavelet packet analysis based on current signature for weld joint strength prediction in pulsed metal inert gas welding process”. In: *Science and Technology of Welding and Joining* 13.7, pp. 638–645.
- Paparrizos, John et al. (2015). “k-shape: Efficient and accurate clustering of time series”. In: *Proceedings of the 2015 ACM SIGMOD international conference on management of data*, pp. 1855–1870.
- Parzen, Emanuel (1962). “On estimation of a probability density function and mode”. In: *The annals of mathematical statistics* 33.3, pp. 1065–1076.
- Pernambuco, Bryan Stefan Galani et al. (2019). “Online sound based Arc-welding defect detection using artificial neural networks”. In: *2019 Latin American robotics symposium (LARS), 2019 Brazilian symposium on robotics (SBR) and 2019 workshop on robotics in education (WRE)*. IEEE, pp. 263–268.
- Perri, Stefania et al. (2023). “Welding defects classification through a Convolutional Neural Network”. In: *Manufacturing Letters* 35, pp. 29–32.

- Pincombe, Brandon (2005). “Anomaly detection in time series of graphs using arma processes”. In: *Asor Bulletin* 24.4, p. 2.
- Rakthanmanon, Thanawin et al. (2013). “Fast shapelets: A scalable algorithm for discovering time series shapelets”. In: *proceedings of the 2013 SIAM International Conference on Data Mining*. SIAM, pp. 668–676.
- Redmon, Joseph, Santosh Divvala, et al. (2016). “You only look once: Unified, real-time object detection”. In: *Proceedings of the IEEE conference on computer vision and pattern recognition*, pp. 779–788.
- Redmon, Joseph and Ali Farhadi (2017). “YOLO9000: better, faster, stronger”. In: *Proceedings of the IEEE conference on computer vision and pattern recognition*, pp. 7263–7271.
- (2018). “Yolov3: An incremental improvement”. In: *arXiv preprint arXiv:1804.02767*.
- Ren, Huorong et al. (2018). “Anomaly detection using piecewise aggregate approximation in the amplitude domain”. In: *Applied Intelligence* 48, pp. 1097–1110.
- Ren, Wenjing et al. (2020). “A Novel Convolutional Neural Network Based on Time–Frequency Spectrogram of Arc Sound and Its Application on GTAW Penetration Classification”. In: *IEEE Transactions on Industrial Informatics* 17.2, pp. 809–819.
- Ribeiro, Marco Tulio et al. (2016). “" Why should i trust you?" Explaining the predictions of any classifier”. In: *Proceedings of the 22nd ACM SIGKDD international conference on knowledge discovery and data mining*, pp. 1135–1144.
- Schmidl, Sebastian et al. (2022). “Anomaly detection in time series: a comprehensive evaluation”. In: *Proceedings of the VLDB Endowment* 15.9, pp. 1779–1797.
- Scholkopf, Bernhard et al. (2000). “Support vector method for novelty detection”. In: *Advances in neural information processing systems* 12.3, pp. 582–588.
- Schölkopf, Bernhard (2000). “The kernel trick for distances”. In: *Advances in neural information processing systems* 13.
- Selvi, Selcuk et al. (2018). “Cold metal transfer (CMT) technology-An overview”. In: *Defence technology* 14.1, pp. 28–44.
- Senin, Pavel (2008). “Dynamic time warping algorithm review”. In: *Information and Computer Science Department University of Hawaii at Manoa Honolulu, USA* 855.1-23, p. 40.

- Shaukat, Kamran et al. (2021). “A review of time-series anomaly detection techniques: A step to future perspectives”. In: *Advances in Information and Communication: Proceedings of the 2021 Future of Information and Communication Conference (FICC), Volume 1*. Springer, pp. 865–877.
- Shin, Seungmin et al. (2020). “Real-time detection of weld defects for automated welding process base on deep neural network”. In: *Metals* 10.3, p. 389.
- Shumin, Ding et al. (2011). “AdaBoost learning for fabric defect detection based on HOG and SVM”. In: *2011 International conference on multimedia technology*. IEEE, pp. 2903–2906.
- Soni, Shashank et al. (2013). “Reduction of welding defects using Six Sigma techniques”. In: *International Journal of Mechanical Engineering and Robotics Research* 2.3, pp. 404–412.
- Srinivasan, D et al. (2022). “A review on Cold Metal Transfer (CMT) technology of welding”. In: *Materials Today: Proceedings*.
- Stone, David C (1995). “Application of median filtering to noisy data”. In: *Canadian Journal of chemistry* 73.10, pp. 1573–1581.
- Su, Jing et al. (2015). “Anomaly detection of single sensors using OCSVM_KNN”. In: *Big Data Computing and Communications: First International Conference, BigCom 2015, Taiyuan, China, August 1-3, 2015, Proceedings 1*. Springer, pp. 217–230.
- Sumesh, A, Binoy B Nair, et al. (2018). “Decision tree based weld defect classification using current and voltage signatures in GMAW process”. In: *Materials Today: Proceedings* 5.2, pp. 8354–8363.
- Sumesh, A, K Rameshkumar, et al. (2015). “Use of machine learning algorithms for weld quality monitoring using acoustic signature”. In: *Procedia Computer Science* 50, pp. 316–322.
- Sun, Jun et al. (2019). “An effective method of weld defect detection and classification based on machine vision”. In: *IEEE Transactions on Industrial Informatics* 15.12, pp. 6322–6333.
- Surovi, Nowrin Akter et al. (2022). “A Study of Machine Learning Framework for Enabling Early Defect Detection in Wire Arc Additive Manufacturing Processes”. In: *International Design Engineering Technical Conferences and Computers and Information in Engineering Conference*. Vol. 86229. American Society of Mechanical Engineers, V03AT03A002.
- Teng, Mingyan (2010). “Anomaly detection on time series”. In: *2010 IEEE International Conference on Progress in Informatics and Computing*. Vol. 1. IEEE, pp. 603–608.
- Thekkuden, Dinu Thomas et al. (2018). “Instant detection of porosity in gas metal arc welding by using probability density distribution and control chart”. In: *The International Journal of Advanced Manufacturing Technology* 95, pp. 4583–4606.

- Theumer, Philipp et al. (2021). “Anomaly detection on industrial time series for retaining energy efficiency”. In: *Procedia CIRP* 99, pp. 33–38.
- Tripathy, Sarthak Manas et al. (2022). “Explaining Anomalies in Industrial Multivariate Time-series Data with the help of eXplainable AI”. In: *2022 IEEE International Conference on Big Data and Smart Computing (BigComp)*. IEEE, pp. 226–233.
- Valavanis, Ioannis et al. (2010). “Multiclass defect detection and classification in weld radiographic images using geometric and texture features”. In: *Expert Systems with Applications* 37.12, pp. 7606–7614.
- Wang, Haiming et al. (2022). “Anomaly Data Detection of Rolling Element Bearings Vibration Signal Based on Parameter Optimization Isolation Forest”. In: *Machines* 10.6, p. 459.
- Wang, Zhou et al. (2004). “Image quality assessment: from error visibility to structural similarity”. In: *IEEE transactions on image processing* 13.4, pp. 600–612.
- Wang, Zilong et al. (2021). “Unsupervised deep learning approach using a deep auto-encoder with a one-class support vector machine to detect damage”. In: *Structural Health Monitoring* 20.1, pp. 406–425.
- Węglarczyk, Stanisław (2018). “Kernel density estimation and its application”. In: *ITM Web of Conferences*. Vol. 23. EDP Sciences, p. 00037.
- Wen-ming, GUO et al. (2019). “Welding defect detection of x-ray images based on faster r-cnn model”. In: *Journal of Beijing University of Posts and Telecommunications* 42.6, p. 20.
- Wu, Renjie et al. (2021). “Current time series anomaly detection benchmarks are flawed and are creating the illusion of progress”. In: *IEEE Transactions on Knowledge and Data Engineering*.
- Xia, Chunyang et al. (2020). “Vision based defects detection for Keyhole TIG welding using deep learning with visual explanation”. In: *Journal of Manufacturing Processes* 56, pp. 845–855.
- Xing, Zhengzheng et al. (2010). “A brief survey on sequence classification”. In: *ACM Sigkdd Explorations Newsletter* 12.1, pp. 40–48.
- Xu, Haoyan et al. (2019). “A vibration signal anomaly detection method based on frequency component clustering and isolated forest algorithm”. In: *2019 IEEE 2nd International Conference on Automation, Electronics and Electrical Engineering (AUTEEE)*. IEEE, pp. 49–53.
- Yamaguchi, Akihiro et al. (2018). “One-class learning time-series shapelets”. In: *2018 IEEE International Conference on Big Data (Big Data)*. IEEE, pp. 2365–2372.

- Yang, Jiong et al. (2004). “Mining surprising periodic patterns”. In: *Data Mining and Knowledge Discovery* 9, pp. 189–216.
- Yang, Kiyong et al. (2004). “A PCA-based similarity measure for multivariate time series”. In: *Proceedings of the 2nd ACM international workshop on Multimedia databases*, pp. 65–74.
- Yang, Yanjun et al. (2021). “Fault early warning of wind turbine gearbox based on multi-input support vector regression and improved ant lion optimization”. In: *Wind Energy* 24.8, pp. 812–832.
- Ye, Lexiang et al. (2011). “Time series shapelets: a novel technique that allows accurate, interpretable and fast classification”. In: *Data mining and knowledge discovery* 22, pp. 149–182.
- Yi, Jihun et al. (2020). “Patch svdd: Patch-level svdd for anomaly detection and segmentation”. In: *Proceedings of the Asian Conference on Computer Vision*.
- Zhang, Dongyu et al. (2010). “Time series classification using support vector machine with Gaussian elastic metric kernel”. In: *2010 20th International Conference on Pattern Recognition*. IEEE, pp. 29–32.
- Zhang, Kaihua et al. (2021). “Solder joint defect detection in the connectors using improved faster-rnn algorithm”. In: *Applied Sciences* 11.2, p. 576.
- Zhang, Zhifen and Shanben Chen (2017). “Real-time seam penetration identification in arc welding based on fusion of sound, voltage and spectrum signals”. In: *Journal of Intelligent Manufacturing* 28, pp. 207–218.
- Zhang, Zhifen, Xizhang Chen, et al. (2014). “Online welding quality monitoring based on feature extraction of arc voltage signal”. In: *The International Journal of Advanced Manufacturing Technology* 70, pp. 1661–1671.
- Zhang, Zhifen, Guangrui Wen, et al. (2019). “Weld image deep learning-based on-line defects detection using convolutional neural networks for Al alloy in robotic arc welding”. In: *Journal of Manufacturing Processes* 45, pp. 208–216.
- Zhu, Bonnie et al. (2011). “Revisit dynamic arima based anomaly detection”. In: *2011 IEEE Third International Conference on Privacy, Security, Risk and Trust and 2011 IEEE Third International Conference on Social Computing*. IEEE, pp. 1263–1268.
- Zuo, Yinlong et al. (2021). “Application of YOLO Object Detection Network In Weld Surface Defect Detection”. In: *2021 IEEE 11th Annual International Conference on CYBER Technology in Automation, Control, and Intelligent Systems (CYBER)*. IEEE, pp. 704–710.

Appendix

A Causality between welding signals

We noticed that in some cases, there is the signature of the burn-through both in the wire speed signal and the voltage signal, as shown in Fig. 13. We were interested in investigating if, in this case, the burn-through is caused by abnormal movements of the wire. To this end, we were interested in studying the causalities between the signals. A time series Y is said to be causing another time series X , if knowing Y reduced the error of predicting X . This is called Granger causality. To study causality, the time series must be stationary. We employed Variational mode decomposition in order to remove the trend component of the voltage signals. We then employed Transfer Entropy (TE), which is a non-parametric causality measure from the information theory field. It detects linear and non-linear causalities between time series. For the calculation of TE, the time series

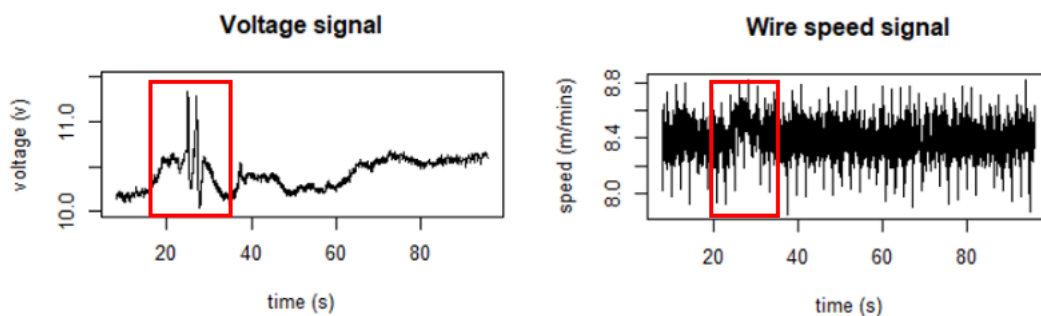


Figure 13: An example of voltage and wire speed signals, where the burn-through is noticed in both.

Table 3: Results of Transfer Entropy estimated for the defective weld signals

Direction	TE
<i>Wire</i> \rightarrow <i>Voltage</i>	0.0831
<i>Voltage</i> \rightarrow <i>Wire</i>	0.2562

are considered stationary Markov processes. The TE from a time series Y to X (the amount of information transferred from Y to X) is given by:

$$TE_{Y \rightarrow X} = \sum p(X_{n+1}, X_n^k, X_n^l) \log \frac{p(X_{n+1} | X_n^k, Y_n^l)}{p(X_{n+1} | X_n^k)} \quad (6)$$

where:

- X_n, Y_n are the processes X and Y at time n .
- k, l are the order of the Markov processes X and Y respectively. Chosen to be 1 in our work.

If Y does not cause X, the conditional probability $p(X_{n+1} | X_n^k, Y_n^l)$ is equal to $p(X_{n+1} | X_n^k)$, the TE is then null, which indicates no information flow from Y to X. Table 3 in the two directions, we obtain a TE value of 0.0831 in the direction of *Wire* \rightarrow *Voltage* and 0.2562 in the other direction. These values suggest that there is more information transferred from the voltage to the wire speed signal, indicating that burn-through initially appears in the voltage signal, which is then transferred to the wire speed signal. This observation is consistent with the physics of TIG welding, as abnormal wire speed or the absence of wire in welding is unlikely to cause burn-through.

B Whole time series anomaly detection

We are interested here in investigating the performance of the OC-SVM with distance substitution kernels for the detection of abnormal whole time series. This can be formalized as: given a time series x_t of real values ordered in time with $t \in [1, 2, ..n]$ where n is the length of the time series, we seek to predict if the whole x_t is normal or abnormal by analyzing them using a model trained to recognize normal whole time series. The problem of abnormal whole time series is only artificially different from the problem of abnormal subsequence detection. The goal here is to study the comparison of the proposed approach with the other approaches when working with sequences with higher lengths than those of the subsequences considered before.

To that end, we consider voltage signals from the circular welding and the orbital welding processes. We consider a dataset composed of 2000 normal signals and 30 abnormal signals for the former and 1500 normal signals and 50 abnormal signals for the latter. We follow the same experimental protocol defined in Chapter 2 as well as the same distances for each process.

Results for the circular welding signals are given in Table 4. The OC-SVM with both kernels and the autoencoder achieve an F-score of 1. The model with the *RBF* kernel is the fastest, as it

Table 4: Results for abnormal full-series detection in the circular welding process.

Model	F-score 1	F-score 2	F-score 3	F-score 4	F-score 5	Mean	Time
OC-SVM <i>RBF</i> L^2	1	1	1	1	1	1	0.06
OC-SVM <i>ND</i> L^2	1	1	1	1	1	1	0.93
k^{th} NN L^2	0.938	0.968	0.938	0.984	0.938	0.953	19.59
Mean k -NN L^2	0.938	0.984	0.923	0.952	0.923	0.944	19.59
Features & IForest	0.87	0.811	0.896	0.857	0.923	0.871	4.29
AutoEncoder	1	1	1	1	1	1	0.476

Table 5: Results for abnormal full-series detection in the orbital welding process.

Model	F-score 1	F-score 2	F-score 3	F-score 4	F-score 5	Mean	Time
OC-SVM <i>RBF</i> $lb_improved$	0.99	0.99	1	1	0.98	0.992	0.318
OC-SVM <i>ND</i> $lb_improved$	0.990	0.990	1	0.990	0.980	0.990	0.216
k^{th} -NN $lb_improved$	1	0.971	1	0.98	0.943	0.979	3.64
Mean k -NN $lb_improved$	0.99	0.971	1	0.99	0.926	0.975	3.64
Features & IForest	0.935	0.917	0.951	0.935	0.891	0.926	2.35
AutoEncoder	0.947	0.929	0.959	0.935	0.906	0.940	0.104

required only 1 support vector for the prediction, while the one with the ND kernel required 16 support on average. The feature-based approach has the lowest F-score while the k -NN approaches are the slowest as the signals have a relatively high length here.

For the signals of the orbital welding, roughly the same results are obtained, as Table 5 shows. The ranking of the methods in terms of F1-scores remains the same. In terms of the inference time, the autoencoder is slightly faster here than the OC-SVM models but has a lower average F1-score. The results obtained here further show the advantages of the proposed approach for fast and accurate anomaly detection.

C The software for real-time anomaly detection and diagnosis in the circular welding process

The pipeline of the software is given in Fig. 14. The signal is first analyzed by the anomaly detector. Abnormal subsequence is extracted from the signal if any and classified using the ROCKET model. Fig. 15 shows the developed software that is in a dashboard format. It shows the two voltage signals and gives the localization of the anomaly if any. The tables *diagnosis* at the right hand give the diagnosis, which consists of the probability of anomalies obtained by transforming the anomaly scores into probabilities using the logistic function and the class of the anomalies along with the probability of the classification.

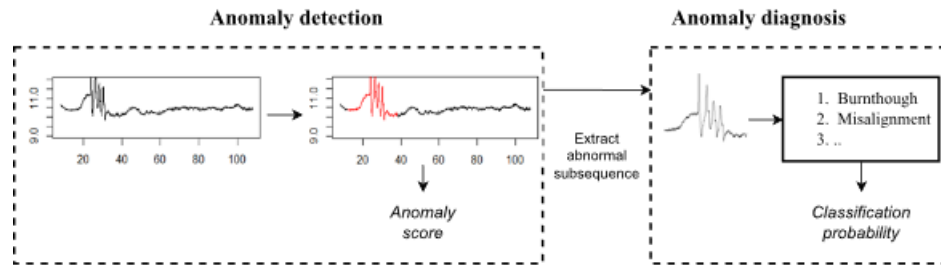


Figure 14: The pipeline of the circular welding monitoring.

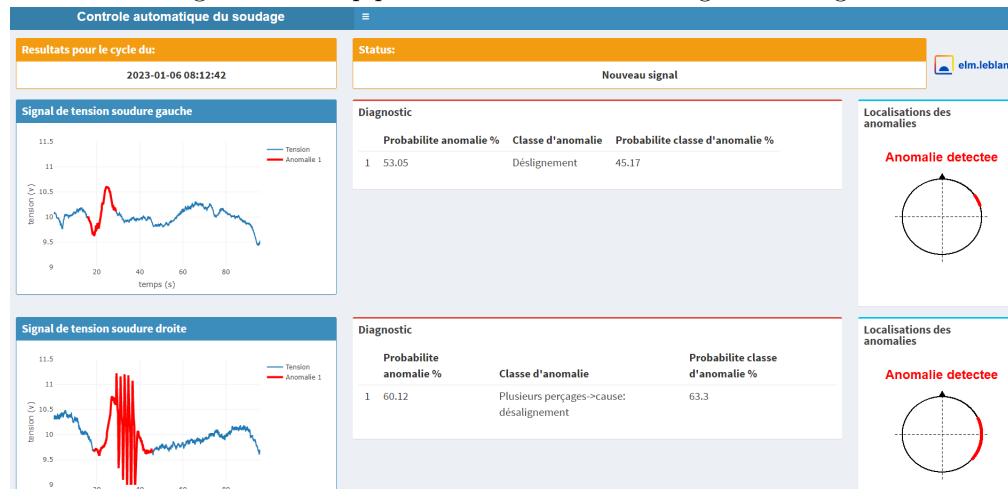


Figure 15: A screenshot of the developed software.

D Detecting abnormal subsequences of variable lengths

We propose here two approaches that can be used to detect variable length anomalies in time series. The first component of the two approaches is change point detection. Given a time series $x = (x_1, \dots, x_n)$, change point detection consists in determining the times $\tau_1 : m$, where $m \ll n$, at which a change occurs in the probability density distribution of the time series. Here, we consider inferring $\tau_1 : m$ based on the change in the mean using the R package *changepoint* which uses the likelihood ratio and the PELT algorithm to find multiple change points in a time series.

After segmenting the time series into homogeneous segments of variable lengths, we can use one of the proposed approaches shown in Fig. 16 to be able to learn the normality and to detect anomalies in variable length subsequences. The first approach that we propose consists in using an elastic dissimilarity with OCSVM that handles variable length subsequences such as the Shape Based Distance (SBD), which is a non-metric dissimilarity. In the process of calculating $\text{SBD}(x,y)$, where $x = (x_1, x_2, \dots, x_m)$ and $y = (y_1, y_2, \dots, y_n)$, y is kept static while x is slid over y , at each shift $s \in [-n, n]$, the inner product is computed to determine the similarity. The shift of a sequence x is

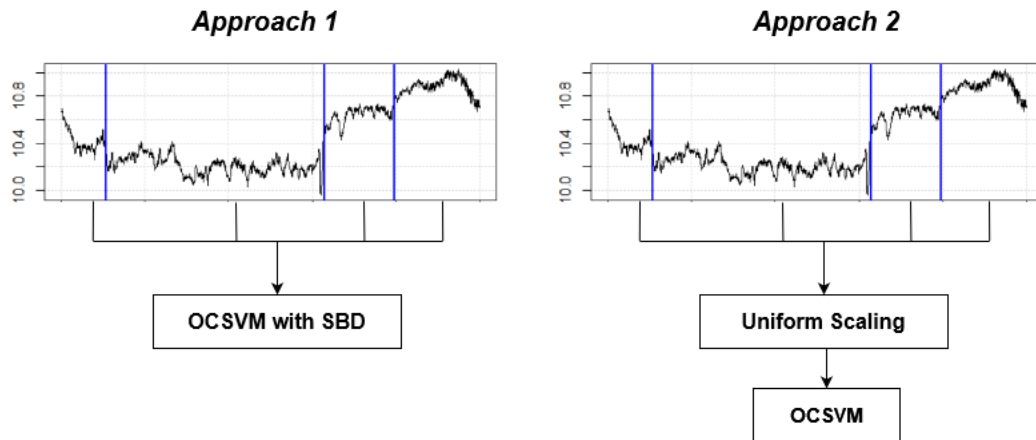


Figure 16: The two proposed approaches for detecting abnormal variable length subsequences.

defined as follows:

$$x_s = \begin{cases} \overbrace{(0, \dots, 0, x_1, \dots, x_{n-s})}^s & \text{if } s \geq 0 \\ \overbrace{(x_{1-s}, \dots, x_n, 0, \dots, 0)}^s & \text{if } s < 0 \end{cases} \quad (7)$$

The cross-correlation vector $CC_w = R_{w-m}$ of length $2n - 1$ where $w \in [1, \dots, 2n + 1]$ is given by:

$$R_k(x, y) = \begin{cases} \sum_{l=1}^{m-k} x_{l+k} \cdot y_l & k \geq 0 \\ R_{-k}(x, y) & < 0 \end{cases} \quad (8)$$

The SBD is then computed by transforming the maximum value CC_w to a normalized dissimilarity:

$$SBD(x, y) = 1 - \max_w \left(\frac{CC_w(x, y)}{\sqrt{R_0(x, x)R_0(y, y)}} \right) \quad (9)$$

In the case where lock-step measures are preferable, the second approach can be employed. It uses Uniform Scaling, which is an interpolation approach, in order to scale the variable length subsequences into a fixed length. To scale a time series x of length m to produce a new time series x' of length n , the Uniform Scaling is defined by the following formula:

$$x'_j = x_{\lceil j * m/n \rceil}, 1 \leq j \leq n \quad (10)$$

We consider here scaling the subsequence to the length 300. We investigated both approaches by training from 50 normal voltage signals from the circular welding segmented using the change point method. We tested on a test signal containing an abnormal subsequence. The results are shown in Fig.17. There are 3 subsequences in the test signal, and 3 anomaly scores are then produced by each approach. From Fig.17 we can notice that both approaches have the same ranking of the subsequence in terms of abnormality.

These results encourage further investigation in this research direction for welding defect detection. We considered here mean change detection for segmenting the time series. In future works, other change detection should be considered, as segmentation is important in these approaches.

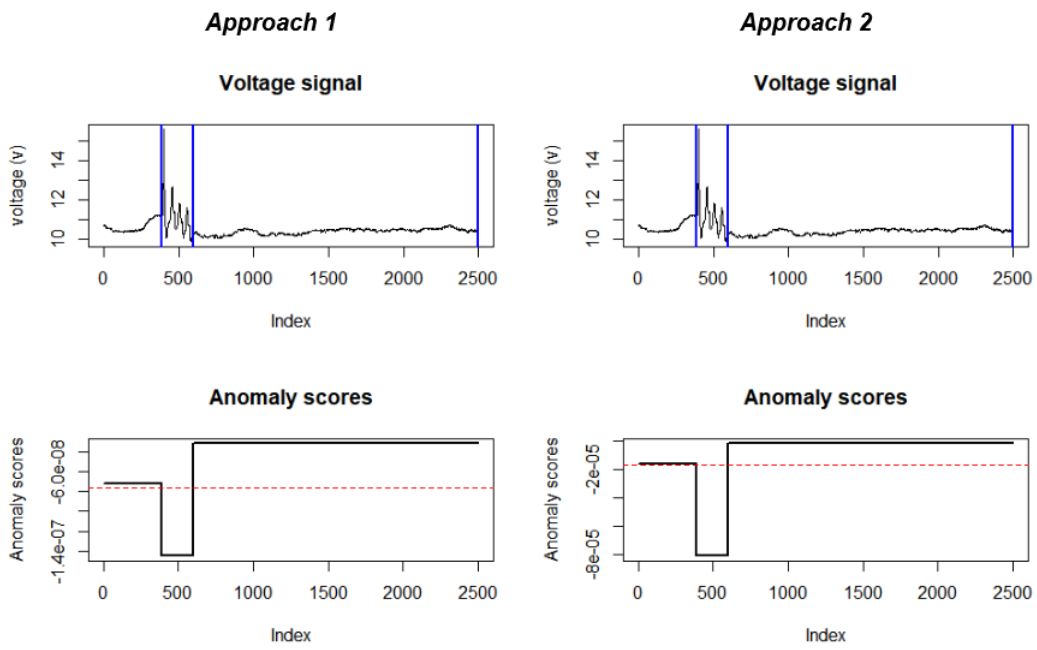


Figure 17: Anomaly scores produced by each approach for the test signal.

E Pseudocode of ROCKET for explainable abnormal subsequence detection

The pseudocode highlighting the important steps for training an OC-SVM model using the transform obtained by ROCKET is given in Algorithm 3, while the testing phase is given by Algorithm 4. Finally, the pseudocode for explaining the abnormal patterns is given in Algorithm 5.

Algorithm 3 Train OC-SVM with ROCKET

```

1:  $\hat{S}$  ▷ Subsequences of some normal time series
2:  $w, d = \text{generate\_kernels}(k)$  ▷ Generate  $k$  kernel weights  $w$  and their dilations  $d$ .
3:
4: for (i =1 to  $|\hat{S}|$ ) do
5:   for (j =1 to  $k$ ) do
6:      $\text{conv\_output} \leftarrow \text{apply\_kernel}(\hat{S}^i, w[j], d[j])$ 
7:      $\text{transform\_train}[i, j] \leftarrow \max(\text{conv\_output})$ 
8:   end for
9: end for
10:  $\text{model} \leftarrow \text{train\_ocsvm}(\text{transform\_train}, \nu, \gamma)$  ▷ Fit the OC-SVM model with the parameters  $\nu, \gamma$ .

```

Algorithm 4 Predictions with OC-SVM and ROCKET

```

1:  $x_t$  ▷ The test time series
2:  $\tau$  ▷ Threshold of the anomaly scores
3:  $S \leftarrow \text{get\_subsequences}(x_t, w)$  ▷ Subsequences of the test time series
4: for (i =1 to  $|S|$ ) do
5:   for (j =1 to  $k$ ) do
6:      $\text{conv\_output} \leftarrow \text{apply\_kernel}(S^i, w[j], d[j])$ 
7:      $\text{transform\_test}[i, j] \leftarrow \max(\text{conv\_output})$ 
8:   end for
9: end for
10:  $\text{Anomaly\_scores} \leftarrow \text{model.predict}(\text{transform\_test})$ 
11:  $\text{Final\_predictions} \leftarrow \text{convert\_to\_binary}(\text{Anomaly\_scores}, \tau)$  ▷ 0 if  $\text{Anomaly\_scores}[i] > \tau$ , 1 otherwise

```

Algorithm 5 Explainability

```
1:  $S$                                 ▷ An abnormal subsequence.
2:  $x'$                                 ▷ The transform of the abnormal subsequence  $S$ .
3:  $N\_imp\_kernels$                     ▷ The number of important kernels to return.
4:  $FI \leftarrow x' - NN(transform\_train)$     ▷ The features importance defined as the
   difference between the transform of the abnormal subsequence and its nearest neighbor in the
   training data.
5: for (i = 1 to  $k$ ) do
6:   if  $FI[i] \leq 0$  then
7:      $FI[i] \leftarrow 0$ 
8:   end if
9: end for
10:  $Imp\_order \leftarrow order(FI)[1 : N\_imp\_kernels]$     ▷ The indexes of the most important kernels
   that explain the abnormal subsequence.
11: for (i = 1 to  $N\_imp\_kernels$ ) do
12:    $conv\_output \leftarrow apply\_kernel(S, w[Imp\_order[i]], d[Imp\_order[i]])$ 
13:    $L[i] \leftarrow argmax(conv\_output)$     ▷ the location of the maximum value of the convolution.
14: end for
15:  $Explaination \leftarrow [FI, L]$ 
```

F Testing ROCKET and OC-SVM on time series from different domains

We are interested here in investigating the use of the ROCKET with OC-SVM for anomaly detection in other types of signals in order to further study its ability to work with different types of signals. For this, we consider an electrocardiogram (ECG). Fig. 18 shows an ECG signal with multiple abnormal subsequences. For training, we use the first 1000 points to extract training subsequences. The length of the subsequence is set to the length of one period of the signal. We use here the original features extracted from the convolutions with 500 kernels without dimensionality reduction, and

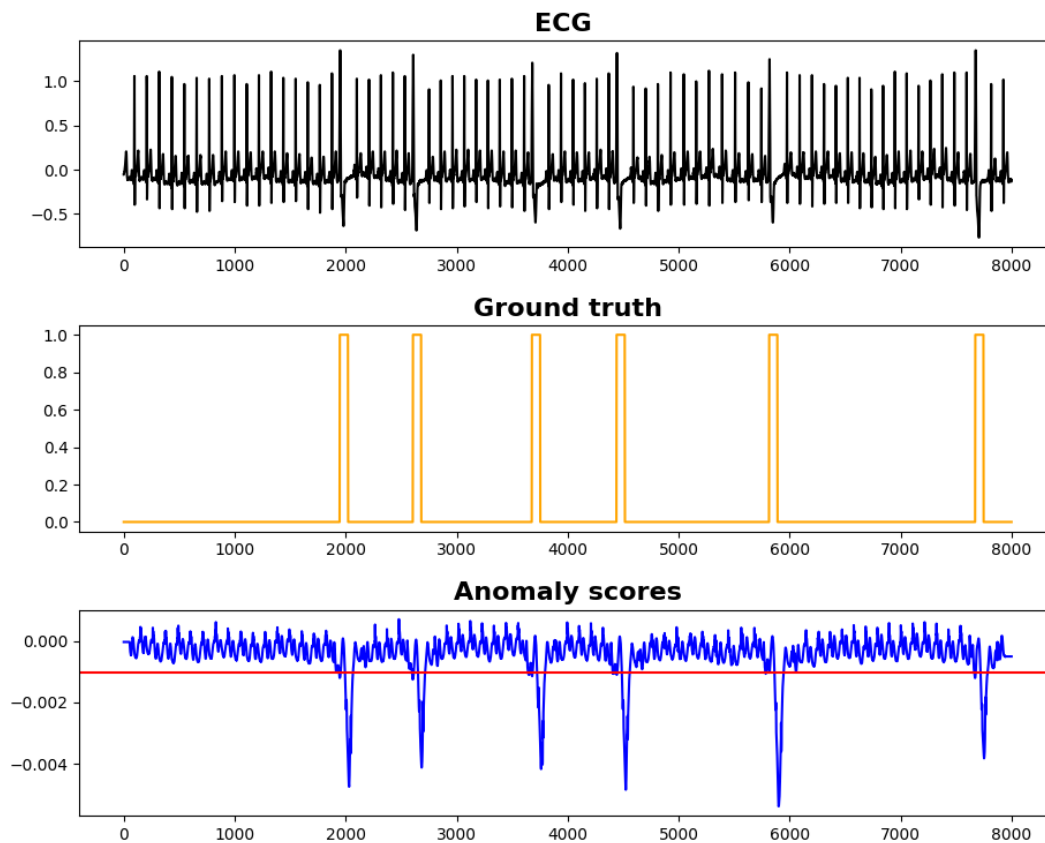


Figure 18: ECG signal along with the ground truth labels and anomaly scores.

we set the parameter γ of the RBF kernel to 10^{-4} . Fig. 18 gives the anomaly scores generated with OC-SVM along with the ground truth labels for each subsequence. We notice from the anomaly scores that the abnormal subsequences are perfectly detected. This shows again that the approach is promising as a generic method for abnormal subsequence detection.

We also tested the approach on a signal from the Mars Curiosity Rover shown in Fig. 19 that has a subtle anomaly annotated by the experts. Employing the approach with the same parameters set earlier gives the anomaly scores given in Fig. 19. We notice that despite the complexity of this anomaly, the approach perfectly detects it. Fig. 20 shows a zoom on the abnormal subsequence. We can notice that the only difference from a normal subsequence is that the abnormal subsequence

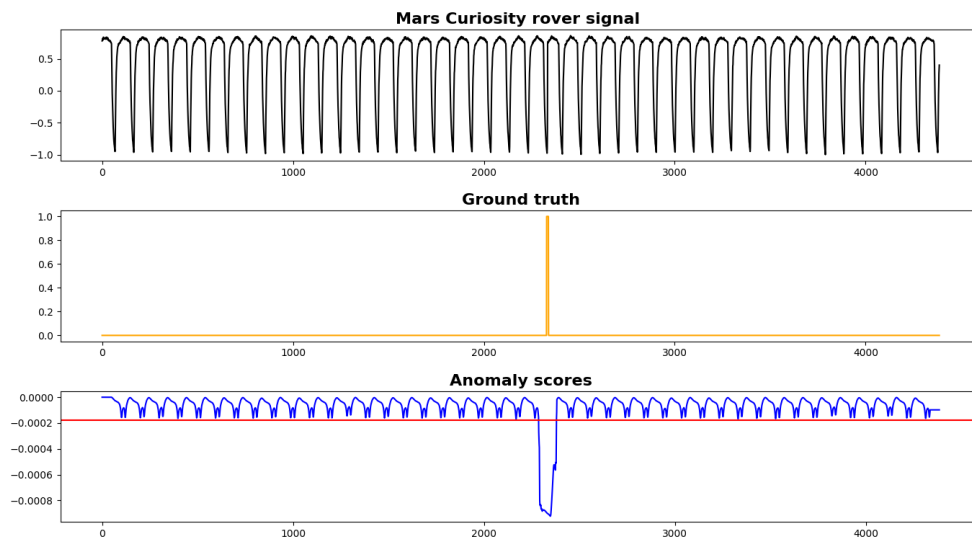


Figure 19: Mars Curiosity rover signal along with the ground truth labels and anomaly scores.

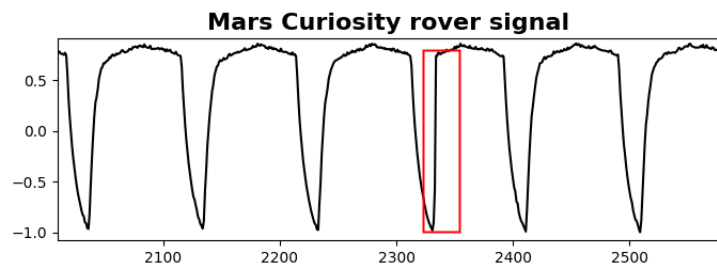


Figure 20: A zoom on the abnormal subsequence.

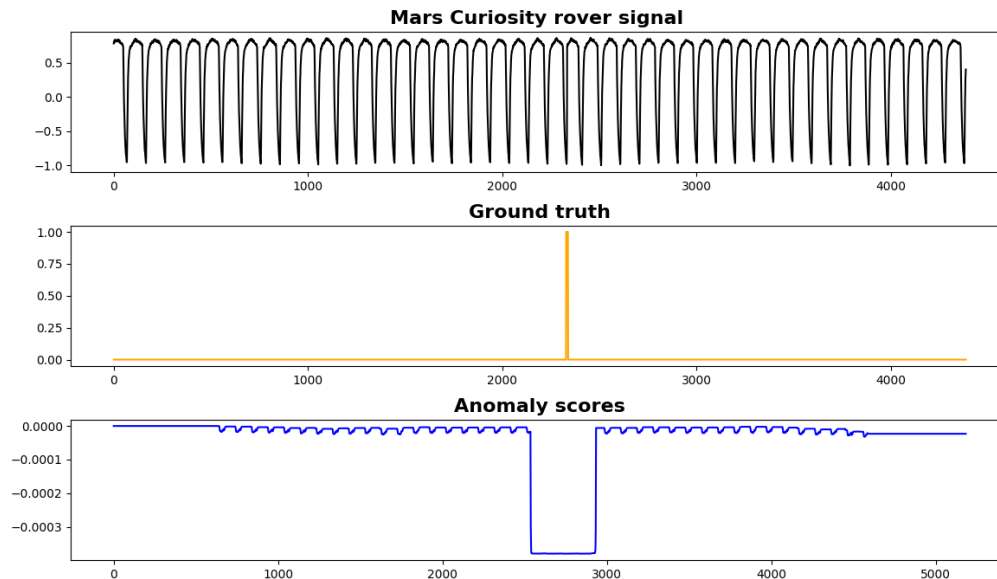


Figure 21: Anomaly score obtained with the larger moving window.

has a steeper rate of increase, which can be difficult to detect for other methods. We noted In 3 that ROCKET allows detecting variable length anomalies in a subsequence. We are interested here in verifying this for this signal. For this, we extracted subsequences using a moving window whose size is equal to 4 times the length of one period of the signal. Fig. 21 shows the signal with the produced anomaly scores for each of the subsequences. We notice that despite the difference between the length of the anomaly and the length of the moving window, the method perfectly detects the anomaly. Other approaches that we tested were not able to detect the anomaly. This verifies that ROCKET allows the detection of even small anomalies in a relatively long subsequence.

A problem that can arise when detecting a small anomaly in a subsequence is to localize the anomaly found. The first approach proposed that deals with explainability is well-suited for this task. Fig. 22 shows the subsequence where an anomaly is detected along with the three most important kernels. We can notice that they perfectly point to the abnormal rate of increase. These good results encourage further investigations into the ability of the approaches to detect and explain abnormal subsequences in time series from different domains.

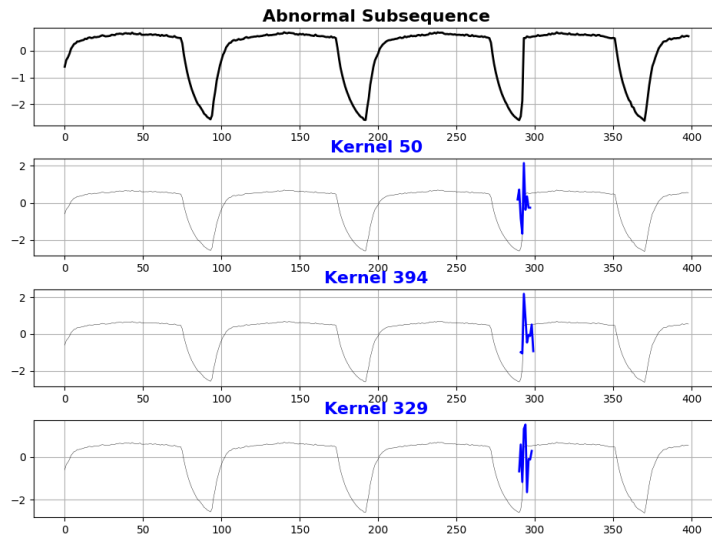


Figure 22: The most important kernels obtained using the proposed explainability approach.

G Welding defect diagnosis using ROCKET and K-means

We are interested here in investigating the use of the representation of the subsequences obtained by the random convolutional kernel transform in order to cluster the abnormal subsequences for the goal of automatic welding defect diagnosis. ROCKET can be interesting for this particular task because it does not require the abnormal subsequences to be aligned. Thus, we expect that ROCKET would give better clustering results than distance-based methods where alignment is required.

We suppose here that abnormal subsequences are detected using the second approach in Chapter 3 that combines ROCKET and PCA. We consider here the abnormal subsequences of the orbital 1 and CMT connection welding (the same that were used in Chapter 2 and Chapter 3) and the use of the K-means algorithm to cluster the abnormal subsequences from the output of the PCA. In K-means, we need to specify the number of clusters k . to estimate k , we compute the silhouette score of the clustering obtained from varying the value of k from 2 to 14, and we choose the k that results in the maximum silhouette score. Fig 23 (a) shows the silhouette scores for the orbital welding subsequences and Fig 23 (b) the ones for the CMT welding. From the figure, we can conclude that the optimal value of k is 5 and 4 for the orbital and the CMT welding signals, respectively. Fig. 24 shows the 5 abnormal subsequences of the orbital signals that are the most representative of the 5 centroids. In the first cluster, we find subsequences with an abnormal upward trend, while the fifth

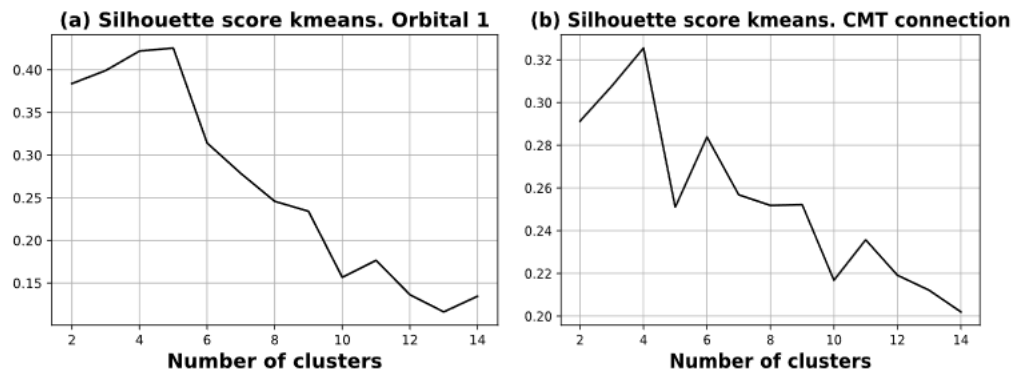


Figure 23: Silhouette scores for different numbers of clusters for (a) orbital signals' subsequences and for those of the CMT signals (b).

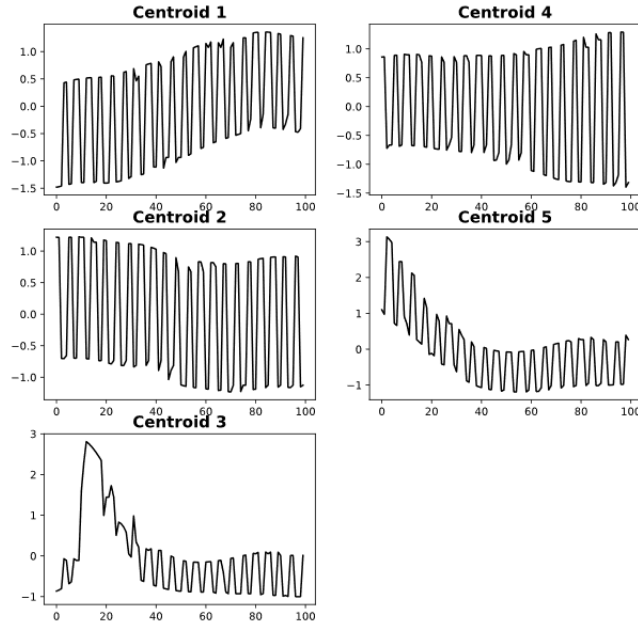


Figure 24: The centroids of the abnormal subsequences of the "orbital 1" signals.

cluster groups subsequences with an abnormal downward trend. Cluster 2 consists of subsequences with a level shift, and Cluster 4 groups subsequences where there is an abnormal change in the amplitude of the oscillations. Cluster 3 had only one subsequence that has a peak with amplitude. The centroids of the abnormal subsequences of the CMT signals are depicted in Fig. 25. Cluster 1 consists of subsequences where there are flat regions indicating the stopping of the movements of the electrode, which indicates the occurrence of a burn-through. Cluster 3 contains subsequences having irregular waveforms indicating abnormal movement of the electrode. Cluster 2 groups subsequences where we see a part having an abnormal amplitude of the oscillations, possibly indicating that the electrode is retrieved before the occurrence of the short circuit. Cluster 4 is similar to Cluster 3 but has more regions where the short circuit does not occur.

The results obtained from the clustering of the abnormal subsequences suggest that ROCKET is a suitable feature extractor that can be used to cluster abnormal subsequences from different signals, allowing us in our case study to perform an unsupervised diagnosis of welding defect and to have a complete framework for the detection and the diagnosis of welding defects based on ROCKET.

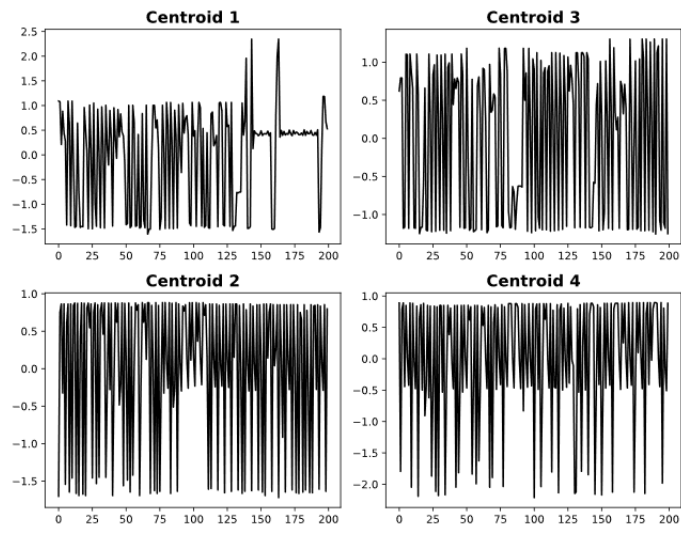


Figure 25: The centroids of the abnormal subsequences of the CMT connection welding signals.

H Unsupervised welding defect detection from weld images

We are interested here in studying the feasibility of unsupervised anomaly detection from weld images by employing an autoencoder that is trained to reconstruct defect-free weld images.

The acquired images by the image acquisition system developed exhibit a significant amount of background. The first task that needs to be accomplished for anomaly detection to work well is to only extract the weld from the whole image. For that, we used U-net, which is an autoencoder designed for image segmentation. We trained the model using 700 weld images and by using image augmentation. The model showed high accuracy in segmenting weld images. An example of the segmentation is shown in Fig. 26.

Once the images are segmented. We trained an autoencoder for anomaly detection (27) where the encoder consists of 3 layers of 32, 64 and 128 kernels respectively, and the latent space of length 200. We tried both the L^2 and the Structural similarity measure (SSIM) losses. We found that the

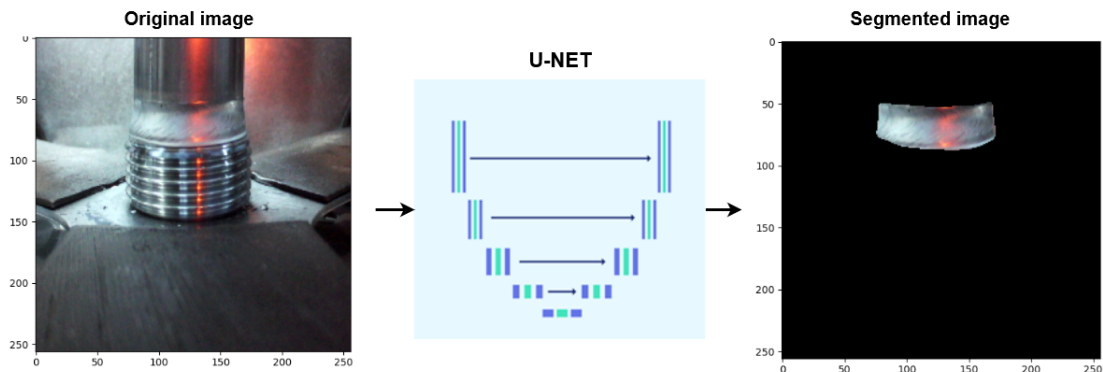


Figure 26: The segmentation of the welded tube image.

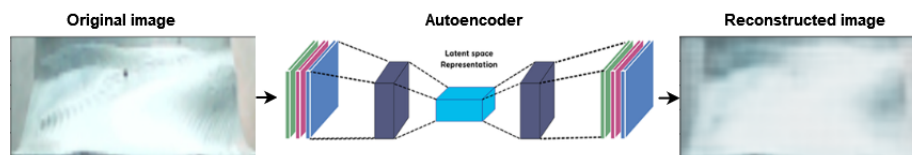


Figure 27: An illustration of the autoencoder for image reconstruction.

latter is more suitable for weld images, as it reconstructs better the texture of the weld. As seen in 4, this type of anomaly detection method uses the difference between the reconstructed image and the original image to produce an anomaly map, where high values would indicate anomalies. We tested the autoencoder on some of the normal and abnormal segmented weld images. Fig. 28 shows three examples. The top image shows a normal weld. We notice that the autoencoder reconstructs this image with low errors, as can be seen from the anomaly map in the third column. For the second and the third image that show welds with burn-through, the autoencoder fails at reconstructing the defect, which allows their detection from the anomaly map shown in the third column where we see high error values at the location of the burn-through. This shows that this unsupervised approach can be used to detect welding defects from images. There are some remarks that can be made from this first study that would help in future works in this direction. First, we notice from Fig. 28 that the autoencoder cannot reconstruct the sharp edges of the tube with

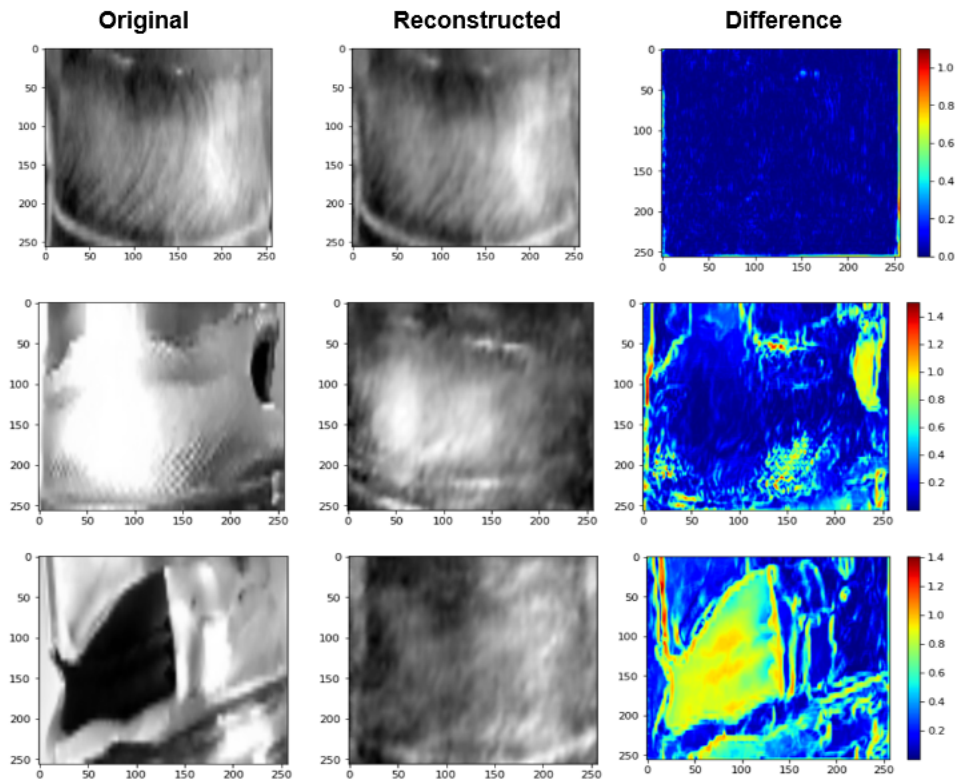


Figure 28: Some results of anomaly detection from the anomaly map.

high accuracy. This introduced high reconstruction errors in the anomaly map that can cause a high false positive rate. Moreover, we notice that even with the use of SSIM loss, the model does not reconstruct the texture of the weld for some images. This can be seen in the second image at the region around the coordinates (150,200). This means that the autoencoder might need a high number of normal training images in order to be able to reconstruct the complex texture of the weld in any image.

Liste de publications

Revues:

1. Melakhsou, Abdallah Amine, and Mireille Batton-Hubert. "Welding monitoring and defect detection using probability density distribution and functional nonparametric kernel classifier." *Journal of Intelligent Manufacturing* 34.3 (2021): 1469-1481.
2. Melakhsou, Abdallah Amine, and Mireille Batton-Hubert. "Welding fault detection and diagnosis using One-Class SVM with distance substitution kernels and random convolutional kernel transform". *The International Journal of Advanced Manufacturing Technology*.

Conférences :

1. Melakhsou, Abdallah Amine, and Mireille Batton-Hubert. "On welding defect detection and causalities between welding signals." *2021 IEEE 17th International Conference on Automation Science and Engineering (CASE)*. IEEE, 2021.
2. Melakhsou, Abdallah Amine, Mireille Batton-Hubert, and Nicolas Casoetto. "Computer Vision based welding defect detection using YOLOv3." *2022 IEEE 27th International Conference on Emerging Technologies and Factory Automation (ETFA)*. IEEE, 2022.
3. Explainable Abnormal Time Series Subsequence Detection Using Random Convolutional Kernels. *4th international conference on deep learning theory and applications*.

Posters:

1. Melakhsou, Abdallah Amine, and Mireille Batton-Hubert. "Study on welding signal in the manufacturing of hot water tanks." *ENBIS 2021 Spring Meeting*. 2021.

Résumé

La fabrication de ballons d'eau chaude nécessite de multiples processus de soudage. La qualité des soudures est cruciale pour la durabilité du produit. Elle est souvent évaluée par inspection visuelle, chronophage et sujette à l'erreur. Une solution à ce problème est l'utilisation de l'apprentissage automatique qui est une technologie se développant de plus en plus dans l'industrie manufacturière. L'objectif de cette recherche est le développement de systèmes de détection et de diagnostic des défauts de soudage par apprentissage en exploitant les signaux capturés lors du soudage automatique et des images de la soudure. La détection des défauts est difficile dans le contexte des ballons d'eau chaude pour de nombreuses raisons: la complexité de la dynamique du soudage, la variété des procédés de soudage et le large éventail de défauts. Les approches proposées ici répondent à ces défis, afin de développer des systèmes utilisables en temps réel. Après avoir étudié la faisabilité de la détection, nous proposons une approche basée sur le One-Class SVM et les noyaux de substitution de la distance. Cette approche ne nécessite que des données brutes de soudures normales et détecte les anomalies en fonction de leur distance à la normalité, ce qui facilite la généralisation. De plus, nous avons proposé une approche de diagnostic basée sur la classification. Une autre contribution est proposée qui étend la transformée de noyaux aléatoires au problème de détection d'anomalies et l'explicabilité. De plus, nous proposons un système détectant les défauts à partir d'images de soudure composé d'un système d'acquisition et d'un réseau neuronal capable de localiser et de classer les défauts.

Mots clés: Détection et diagnostic des défauts; Soudage à l'arc; Détection d'anomalie; Séries temporelles; Dissimilarité; Détection d'objet.

Abstract

The manufacturing of hot water tanks requires multiple welding processes. The quality of the welds is crucial for the durability of the product. It is often assessed by visual inspection, which is time-consuming and prone to error. One solution to this problem is the use of machine learning, which is a growing technology in the manufacturing industry. This research aims to develop systems for detecting and diagnosing welding faults using machine learning by exploiting the signals captured during automatic welding and images of the weld. Fault detection is difficult in the context of hot water storage tanks for many reasons: the complexity of welding dynamics, the variety of welding processes, and the wide range of faults. The approaches proposed here treat these challenges with the aim of developing systems that can be used in real-time. After studying the feasibility of detection, we propose an approach based on One-Class SVM and distance substitution kernels. This approach only requires raw data of conforming welds and detects anomalies based on their distance from normality, which facilitates the generalization. Moreover, we propose a diagnostic approach based on classification. Another contribution is proposed, which extends the random kernel transform to the problem of anomaly detection and explainability. In addition, we propose a system detecting defects from welding images composed of an acquisition system and a neural network capable of locating and classifying defects.

Keywords: Defect detection and diagnosis; Arc welding; Anomaly detection; Time series; Dissimilarity; Object detection.